Title

Engineered Bio-inspired Geometrically Complex Water-repellent Surfaces and Their Applications

Author

Chung, Soochan

Publication Date

2019

Peer reviewed|Thesis/dissertation

Engineered Bio-inspired Geometrically Complex Water-repellent Surfaces and Their Applications

by

Soochan Chung

A dissertation submitted in partial satisfaction of the

requirements for the degree of

Doctor of Philosophy

in

Engineering – Mechanical Engineering

in the

Graduate Division

of the

University of California, Berkeley

Committee in charge:

Professor Hayden K. Taylor

Professor Liwei Lin

Professor Ana Arias

Fall 2019

Engineered Bio-inspired Geometrically Complex
Water-repellent Surfaces and Their Applications

by

Soochan Chung

ABSTRACT

Engineered Bio-inspired Geometrically Complex

Water-repellent Surfaces and Their Applications

by

Soochan Chung

Doctor of Philosophy in Engineering – Mechanical Engineering

University of California, Berkeley

Professor Hayden Taylor, Chair

In nature, various plants and animals exhibit promising structurally-defined functionalities. Many discoveries of efficient water-repellent surfaces in nature have promoted research into engineering bio-inspired artificial structures with superhydrophobicity, due to their huge potential impacts on various applications, such as water-repellency, self-cleaning, condensation acceleration, and drag reduction. In particular, *Nelumbo nucifera* (lotus leaf), has been extensively studied in an effort to replicate its excellent superhydrophobic and low water adhesive characteristics.

According to the inspiration driven from the lotus leaf, the stable combination of chemical modification (e.g. hydrophobic fluoro-silane treatment) and increased surface roughness (e.g. increasing levels of structural hierarchy) is the most important factor to obtain efficient water-repellency. However, most existing manufacturing techniques using a lithographic or molding approach have typically involved only one, or occasionally two, length-scales of roughness, and have not been successful enough to mimic the complex geometries of a biological epidermis, such as the lotus leaf or taro leaf.

In this research, in order to achieve a closer resemblance to the *Nelumbo nucifera* and to obtain even better water-repellent performance, we will introduce various manufacturing breakthroughs and in-depth investigations into novel micro- and nano-manufacturing processes for bio-inspired geometrically complex structures. This research on efficient water-repellency makes extensive contributions in the field of wettability, e.g. microfabrication research, biomimetics, and related fundamental wettability theories.

TABLE OF CONTENTS

ACKNOWLEDGEMENTS

First, I should express my sincere thankfulness to my advisor, Professor Hayden Taylor, for his unending thoughtful comments, his devotion to good guidance and encouragement, and endless support. Professor Hayden Taylor has helped me to grow critical thinking and creative ideas. I cordially am grateful to him for his guidance and all the research support for my Ph.D. program in UC Berkeley.

Also, I thank my dissertation committee professors, Professor Liwei Lin and Professor Ana Arias. Professor Liwei Lin every semester advised me with all the course works as a major field advisor. He also asked me important and difficult engineering questions during my qual exam, which inspired and encouraged me a lot. Professor Ana Arias also encouraged me with a lot of important and critical engineering questions as one of my qualification exam committee members.

I additionally thank the staff of the U.C. Berkeley Biomolecular Nanotechnology Center (BNC) and Jacobs Hall for all the research assistances. Especially, Paul Lum has provided unlimited research support and advices which hugely helped finishing all my projects successfully. I also acknowledge Naima Azgui first teaching me how to use scanning electron microscope, which provided a huge portion of my important results regarding all the micro- and nano- manufactured structures.

I am so much grateful to all my research collaborators, especially Cameron Riley, Kristyn Kadala, Brooks Barrett for their thoughtful comments, critical ideas and feedback, and all the support. And, I would like to especially acknowledge one of my lab-mates, Hossein Heidari, for helping me with unlimited comments, ordering lab supplies, and his devotion to maintaining our lab tidy.

Special thanks to Samsung Scholarship Foundation for funding full five years of my Ph.D program and inviting and hosting a number of important conferences and good social events annually, which helped me to make a lot of good and talented scholars from all over the world. Also, I acknowledge a big research support by the Singapore–Berkeley Building Efficiency and Sustainability in the Tropics (SinBerBEST) program, funded by the National Research Foundation, Prime Minister's Office, Singapore.

Finally, but not least, I would like to thank my parents, my younger brother, and Dr. Inhwa Lee for all their support and encouragements. They made me into who I currently am with their patience, support and love.

LIST OF FIGURES

LIST OF TABLES

Chapter 1. Introduction

In nature, there are various plants and animals that exhibit promising structurally-defined functionalities. Many discoveries of efficient water-repellent examples in nature have intensively promoted the research with bio-inspired structures with superhydrophobicity in past decades. Water repellent surface technology has been attracting a huge attention because of its many potential applications in, e.g., self-cleaning, condensation acceleration, anti-corrosion, anti-biofouling, anti-ice, oil/water separation, anti-fogging, and drag reduction.

In particular, engineering bio-inspired surfaces, such as *Nelumbo nucifera* (lotus leaf), and *Colocasia esculenta* (taro leaf), has been extensively studied to achieve its excellent superhydrophobic and low water adhesive characteristics. *Nelumbo nucifera* (lotus leaf) is a semi-aquatic plant and has wide leaves up to 30 cm in diameter with remarkable superhydrophobicity[2]. In order to adapt to the aquatic environment, the upper epidermis features a distinctive hierarchical structure consisting of papillae with a dense coating of agglomerated wax tubules and periodic undulated boundaries between epidermal cells, which acts as the basis for the well-known water resistance characteristic called the 'lotus effect'.

According to the inspiration driven from natural examples, there are two main factors to prepare efficient water-repellent surfaces: one is to roughen the surface geometries (or increasing the surface roughness), and the other is to modify the surface low-surface-energy materials (hydrophobic chemical termination)[1]. However, the maximum water sessile contact angle achieved only by the low-surface-energy material modification is reported to be 118° (e.g. hydrophobic fluoro-silane treatment).[1] Thus, the stable combination of chemical modification and the increased surface roughness is the most important factor to obtain the efficient water-repellency in this research.

Currently, many methods have been widely studied to obtain efficient superhydrophobic surfaces. In general, based on the widely known Cassie–Baxter relation of the reduced solid-liquid contact interface[3], previous studies have attempted to achieve hierarchical surface with micro- or nano-texturing to reduce the contact area fraction and improving the robustness of the superhydrophobicity[4–10], and thus lower the force is needed to shed water droplets from the surface by, e.g., gravity or air flow.

However, most existing manufacturing techniques with lithographic or molding approach, which typically combined only one, or occasionally two, length-scales of roughness, have not been successful enough to mimic the complex geometries of biological epidermis, such as lotus leaf and taro leaf.

In this research, various manufacturing breakthroughs and in-depth investigations on the novel micro- and nano- manufacturing processes for bio-inspired geometrically complex structures were studied in this research. This study on the efficient water-repellency will make extensive contributions in the field of wettability, e.g. photolithographic research, biomimetic field, and related fundamental wettability theories.

Chapter 2. Motivation and Background

2.1 Outstanding properties of *Nelumbo nucifera* (Lotus leaf)

Nelumbo nucifera (Lotus leaf) is the most representative superhydrophobic example from nature. Although there are many other natural surfaces that achieve high contact angles, the *Nelumbo nucifera* stands unchallenged in the field of stable and perfect water repellency.

The structural configuration of the lotus leaf includes an array of micro-papillae with small tip radii (from 20 to 60 μm in diameter) with a dense coating of agglomerated nano-sized wax crystals (nonacosane diols), and periodic micro-grooves between epidermal cells. By having this unique multi-level hierarchical geometrical roughness of micro- and nano-scales and chemical coating of epicuticular wax, the lotus leaf achieves an extremely low surface–water contact fraction, which leads to the well-known concept of the 'Lotus effect'.

A possible reason for these distinctive evolutionary lotus leaf structures can be deduced from the fact that the stomata of the leaf are located in the upper epidermis.[2] In order to avoid leaf decomposition by heavy rain, contamination, and pathogens especially on the upper epidermis, the lotus leaf has successfully evolved to have a remarkable method of protection, called self-cleaning. And it has been widely studied and illustrated that the superhydrophobicity and self-cleaning property of the lotus leaf can be achieved by the combined effect of optimized surface topographies and unique chemical composition.

2.2 Static contact angle and the two modes of wetting

To better understand the superhydrophobicity obtained through a bio-inspired geometrically complex surface, a popular and standard index for wettability determination needs to be studied. When there is contact between solid and liquid, an ideally isotropic and smooth solid surface achieves equilibrium by surface chemistry and forms a certain contact angle (θ) governed by traditional theory of surface wettability, Young's equation[11,12] as below (Figure 2.1):

$$\gamma^{sv} = \gamma^{sl} + \gamma^{lv} cos\theta \tag{2.1}$$

where, θ is the water sessile contact angle, γ^{sv} is the interfacial tension between solid and vapor, γ^{sl} is the interfacial tension between solid and liquid, γ^{lv} is the interfacial tension between liquid and vapor. As the equation indicates, changes in surface chemistry, such as fluorosilane treatment on the solid surface *etc*., can alter the interfacial tensions related and thereby changing the contact angle (θ) of the equilibrium.

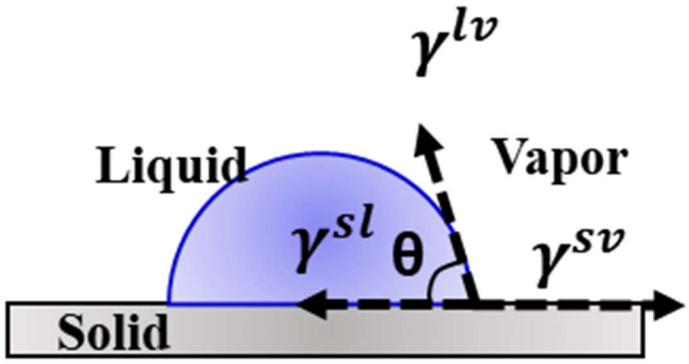

Figure 2.1. A schematic of Young's equation.

In general, a solid surface which has a contact angle smaller than 90° is considered to be hydrophilic, and a surface which has a contact angle greater than 90° is called hydrophobic. Especially, when the contact angle is greater than 150°, such surface is called a superhydrophobic surface (Figure 2.2).

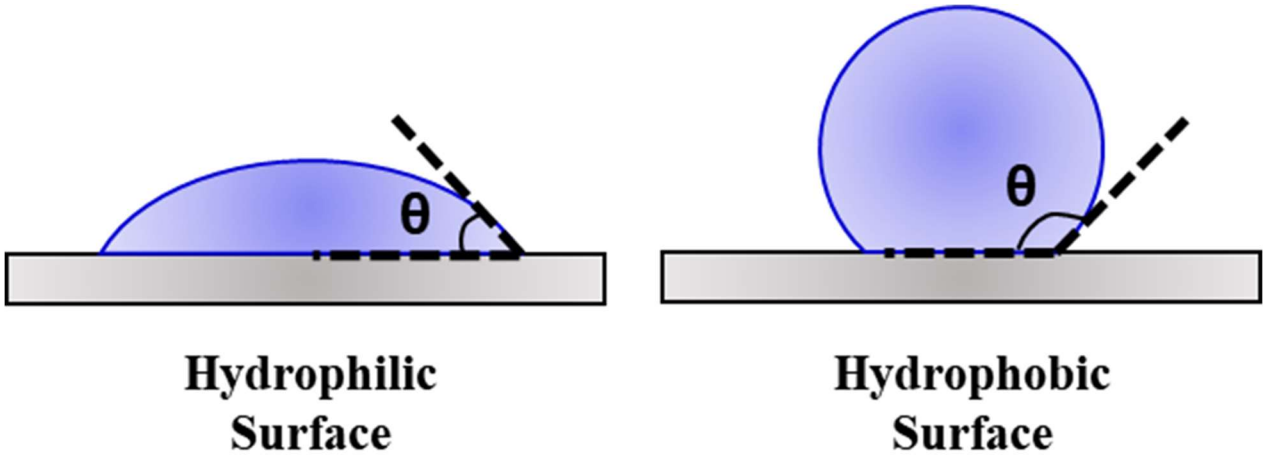

Figure 2.2. Schematics of hydrophilic and hydrophobic surfaces.

Generally, surface chemistry and surface roughness are the two most important factors to achieve the surperhydrophobicity. However, the maximum contact angle obtained only by surface chemistry modification is reported to be 118° (e.g. hydrophobic fluoro-silane treatment).[1] Thus, the effect of surface roughness to obtain the high contact angle has been widely studied.

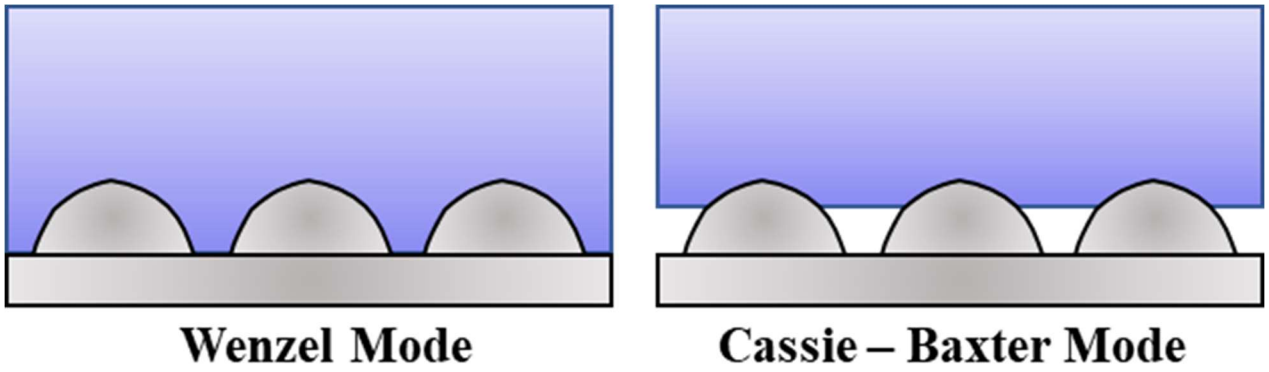

Figure 2.3. Schematics of showing two modes of wetting on rough surface.

As shown in Figure 2.3, the wettability mode on rough surface can be divided into two. The first mode is the Wenzel mode[13], which is a homogeneous mode with only two-phases: solid and water. The Wenzel equation is defined as below,

$$cos\theta^* = r\, cos\theta_O$$

where θ^* is the apparent contact angle, r is the surface roughness, defined as the ratio of the actual area of a rough surface to the geometric projected area, and θ_O is the original contact angle that is predicted by Young's equation.

Since the surface roughness is always greater than or equal to 1, when the θ_O is smaller than 90° (hydrophilic), the apparent contact angle of θ^* decreases with the increase of surface roughness of r, making the rough surface more hydrophilic. And when θ_O is greater than 90 ° (hydrophobic), the apparent contact angle θ^* increases with the increase of surface roughness r, and the surface becomes more hydrophobic.

The other mode is called the Cassie–Baxter mode[3], which is defined as a composite mode with three phases: solid, water, and air. In this mode, a number of air pockets are trapped between the solid structure and contacting liquid. The Cassie–Baxter equation is defined as below,

$$\cos\theta^* = \sum f_i r_i \cos\ \theta_i = (The\ solid\ part) + (The\ air\ part) \tag{2.2}$$

$$= f\left[r_f \cos\theta_o\right] + (1-f)[r_{air}\cos\theta_{air}] \tag{2.3}$$

$$= f \cdot\ r_f \cos\theta_0 +\ f - 1 \tag{2.4}$$

$$(\because r_{air} = 1, \text{and}\ \cos\theta_{air} = \cos 180^\circ\ = -1\ ) \tag{2.5}$$

where *f* is the fraction of liquid–air interface occupied by the solid, and r_f is the roughness ratio of the wetted portion of surface (or the actual solid–liquid interfacial area divided by the projected area).

The Cassie–Baxter equation describes the apparent contact angle based on the summation of solid surface in contact with multiple substances (e.g. liquid and air in Figure 2.3). Thus, the equation starts with the summation of the solid part and the air part of the liquid–air interface. Then the equation is simplified into the final form since the contact angle of the air (θ_{air}) is defined as 180°. If there is no air trapped in between the solid structures (*f* = 1), the Cassie–Baxter equation reduces back to the Wenzel equation. This equation gives us a good insight of how we should design the hydrophobic surface in order to achieve the higher contact angle: for the hydrophobic surface (θ_O is greater than 90°), when the fraction of solid–liquid contact area (*f*) is reduced, the apparent contact angle on the rough surface (θ^*) increases (if $f\ \rightarrow 0\ , \theta^* \rightarrow 180\ °$).

2.3 Contact angle hysteresis (Dynamic contact angle)

Contact angle hysteresis, defined as the difference between advancing (θ_{adv}) and receding (θ_{rec}) contact angles, can be used as another standard to show different superhydrophobic characteristics. There are number of methods to measure advancing and receding angles. One well-known method is the volume-changing method (Figure 2.4). In the volume-changing method, water is slowly pumped out from a needle to the surface. The advancing angle (θ_{adv}) is measured while the volume of droplet is increasing. Then liquid is sucked back in (to the needle. The receding angle (θ_{rec}) is measured while the volume of the droplet is reducing. However, this method can make it difficult to measure

the receding angle precisely because the needle affects the geometry of the droplet contours while the volume is being reduced.[14]

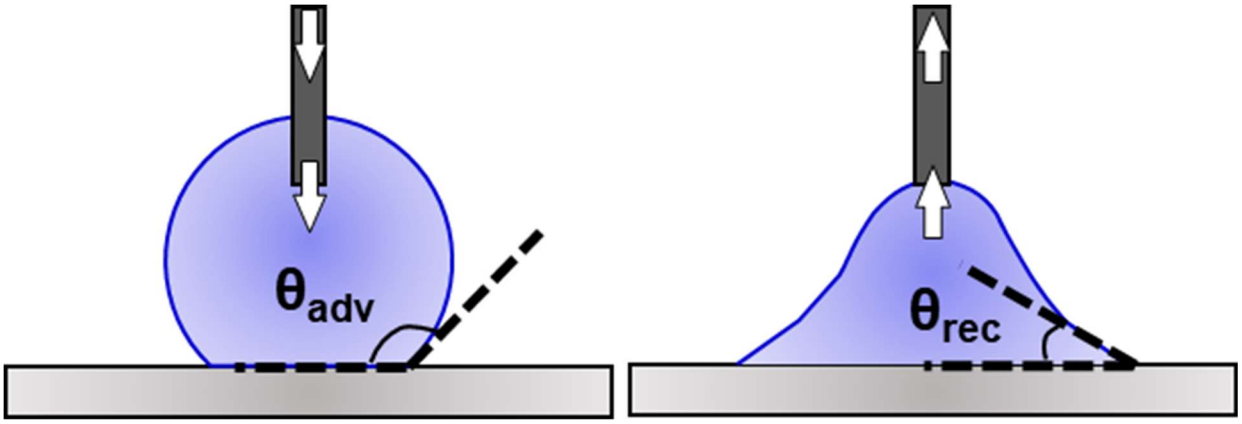

Figure 2.4. Dynamic contact angle measurement by the volume changing method.

Another method of capturing contact angle hysteresis is the tilting plane method (Figure 2.5). This method measures the advancing and receding angles simultaneously while the solid surface is being gradually tilted from horizontal to vertical.[15] As the surface is tilted, the gravity eventually causes the droplet to roll down. Here, the advancing angle is measured at the front of the droplet just before the droplet starts to move and the receding contact angle is measured at the back of the droplet.

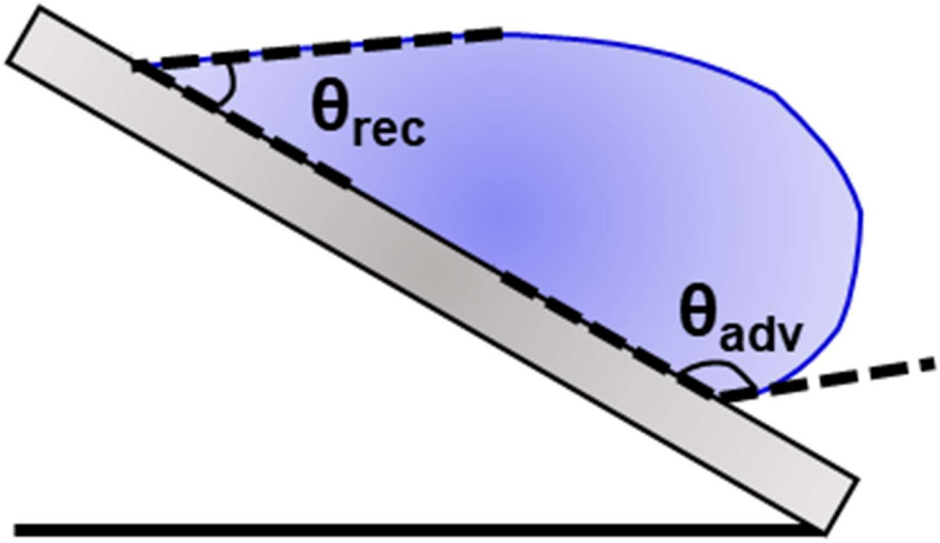

Figure 2.5. Dynamic contact angle measurement by the tilting plane method.

A stable water-repellent surface, which has many important advantageous characteristics such as self-cleaning and anti-biofouling behavior, not only has a high apparent contact angle but also has a low contact angle hysteresis. An effective water-repellent surface exhibits low contact angle hysteresis, which means a small difference between advancing (θ_{adv}) and receding angle (θ_{rec}), low adhesion between liquid and solid, and hence, an ability to shed water easily from the surface. An essential prerequisite for a water-repellent surface with high water sessile contact angle (larger than 170°) and low contact angle hysteresis (lower than 10°) appears to be to minimize the solid–liquid contact fraction, through precise design of geometrically complex structures.

2.4 Main aims of the research

Throughout the dissertation, a number of bio-inspired geometrically complex structures will be introduced in order to achieve progressively closer resemblance to the *Nelumbo nucifera* (lotus leaf) and to obtain superior water-repellency. Our investigations of novel potential micro- and nano- manufacturing processes provided us with various interesting superhydrophobic performances: higher water sessile contact angle, lower water contact angle hysteresis, effective dropwise condensation, and robust water impregnation resistance in an adverse environment (e.g. high-pressure underwater conditions).

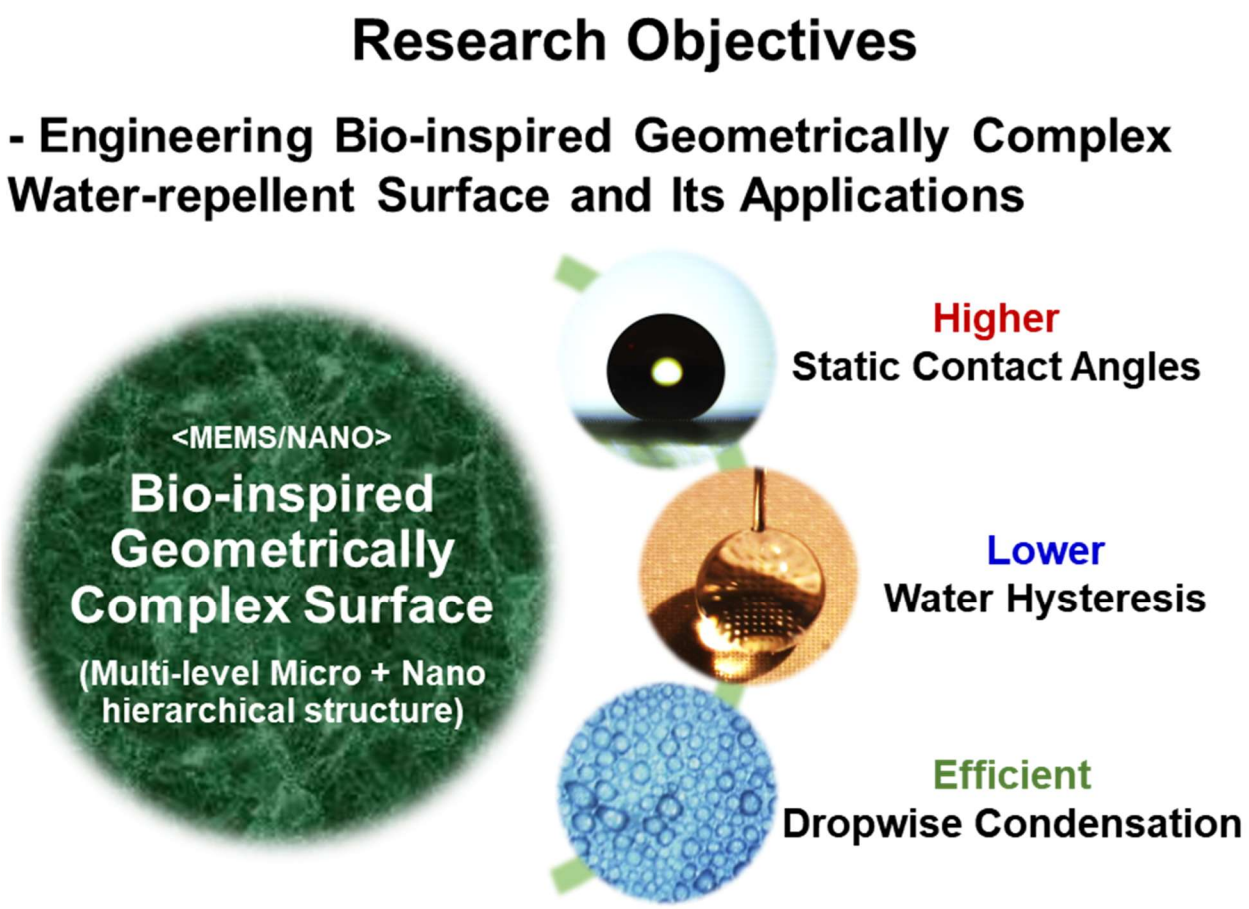

Figure 2.6. Schematics of the research objectives.

As the main aims of this research, a number of important questions will be addressed:

- How can we artificially make arrays of micro-protrusions with curved walls (or micro-papillae) which are coated with conformal nanosized hairy wax crystals, as observed on *Nelumbo nucifera* leaves?
- Which shapes (e.g. square-tipped micro-pillars or micro-domes) will be better for effective water-repellency?
- Does the conventional Cassie–Baxter relation accurately predict the hydrophobic behavior of our surfaces?
- What is the optimal shape and design of surface structures for condensation heat transfer? Can we simulate condensation performance of various patterns in an environment similar to that of tropical regions?

- Can we scale-up synthesis of our nanoporous coating to a full-scale cooling coil and develop an optimal fluorosilane process to minimize chemical usage while maintaining good surface coverage?

- How do droplets condense and merge on the cold surface of a micro-pillar or micro-dome array coated with nanoporous structures?

- Can we manufacture arrays of micro-domes with varying heights via a standard single layer photolithography process?

- What can be the advantage of having varying feature heights compared to conventional photolithographically produced structures with a uniform height?

- How can we generate the periodic undulations between the micro-patterns on the surface?

- Is there a simple method to maximize the effect of periodic micro-grooves?

- Does an additional layer of structural hierarchy provide more robust water-repellency? How can any differences in robustness be quantified?

Chapter 3. Engineering Optimal Shape and Design for Superhydrophobicity

3.1 Introduction and motivation

As the use of air conditioning rises globally, technologies are desired to make cooling and dehumidification more energy-efficient.[16] One particular challenge is the accumulation of condensed atmospheric water on heat exchanger surfaces, which can impede heat transfer and permit biological contamination.[17] Scalable, robust technologies are desired to enhance condensate shedding and keep cooling coil surfaces as dry as possible. One promising route is to render surfaces superhydrophobic to promote dropwise condensation and shedding, and to this end many chemical and morphological modifications have been investigated.[18–20] Inspiration has been sought from nature,[21] in which the multi-scale surface topographies of certain leaves, such as that of the lotus, have been shown to be promote droplet coalescence and shedding by greatly reducing liquid–solid contact and minimizing droplet pinning.[7,22,23] Synthetic repellent surfaces generally involve sharp-edged micro- and nano-structures,[24] which can be simple to manufacture but do not deliver the same droplet-shedding performance as the smoother, dome-shaped microstructures found in nature.[25–27] Engineered dome- or dimple-shaped[28,29] and hierarchical, multi-scale[30] structures are therefore of increasing interest.

Here, we show how dome-shaped microstructures can be simply fabricated and then coated with a nanoporous, fluorosilane-terminated zinc oxide film whose ultrahydrophobic properties on a flat surface were reported previously,[31] to generate a surface with lotus leaf-like performance. The addition of a micro-dome array substantially improved hydrophobicity, as seen through increased static water contact angle and reduced contact angle hysteresis relative to both a flat surface coated with the nanoporous film and an array of sharp-edged micropillars also coated with the film. A scale dependence was also seen, with the highest performance from the smallest features in the 20–50 μm range studied.

Sometimes underlying the design of hierarchical surfaces has been the widely known Cassie–Baxter relation,[3] which models how the apparent static contact angle, θ^*, of a droplet suspended on the protrusions of a rough surface increases as the fraction, ϕ, of the projected surface area in solid–liquid contact reduces:

$$\cos\theta^* = \phi\cos\theta_0 - 1 + \phi \qquad (3.1)$$

where θ_0 is the contact angle on a smooth surface of the same material. This model has, however, been extensively challenged since shortly after its introduction, on the basis that the characteristics of the liquid–solid contact *line* — and not the contact *area* — are of central importance in determining static, advancing and receding contact angles and hence droplet-shedding effectiveness.[27,32,33] The particular geometric design[34] of surface features has been shown to influence static contact angle, sliding angle, and contact angle hysteresis (the difference between advancing and receding angles). Such dependences are seen even at a fixed contact area fraction, indicating the importance of the shape and length of the contact line.

A related concern is droplet pinning, which tends to occur at feature corners and disrupts droplet shedding even if the static contact angle is high.[27,35] Also relevant are the robustness of the droplet's state to external mechanical energy inputs (e.g. droplet impact[36] or hydrostatic pressure[37]), and the fact that condensing droplets may nucleate at any location on the surface and not necessarily on the tips of surface protrusions.[38–40] A comprehensive and robust predictive model for contact angles, droplet shedding, and robustness therefore remains elusive, and especially so for surfaces with curved topographies.

Superhydrophobic surfaces with multi-scale topographies can offer exceptionally high apparent water contact angles and low contact angle hysteresis by virtue of the small liquid–solid contact fractions they enable. Naturally occurring water-repellent surfaces such as lotus leaves often feature dome-shaped micro-scale protrusions, whose lack of sharp edges also facilitates smooth droplet shedding without pinning. Engineered hydrophobic surfaces, however, have not yet fully exploited the merits of protrusions with a controlled curvature. In this work, thermal re-flow of photoresist patterns followed by elastomeric casting was used to fabricate arrays of micro-domes in the size range 20–50 μm. These microstructures were coated with a nanoporous zinc oxide film and fluorosilanized to produce hierarchical surface topographies that would achieve outstanding superhydrophobicity.[41]

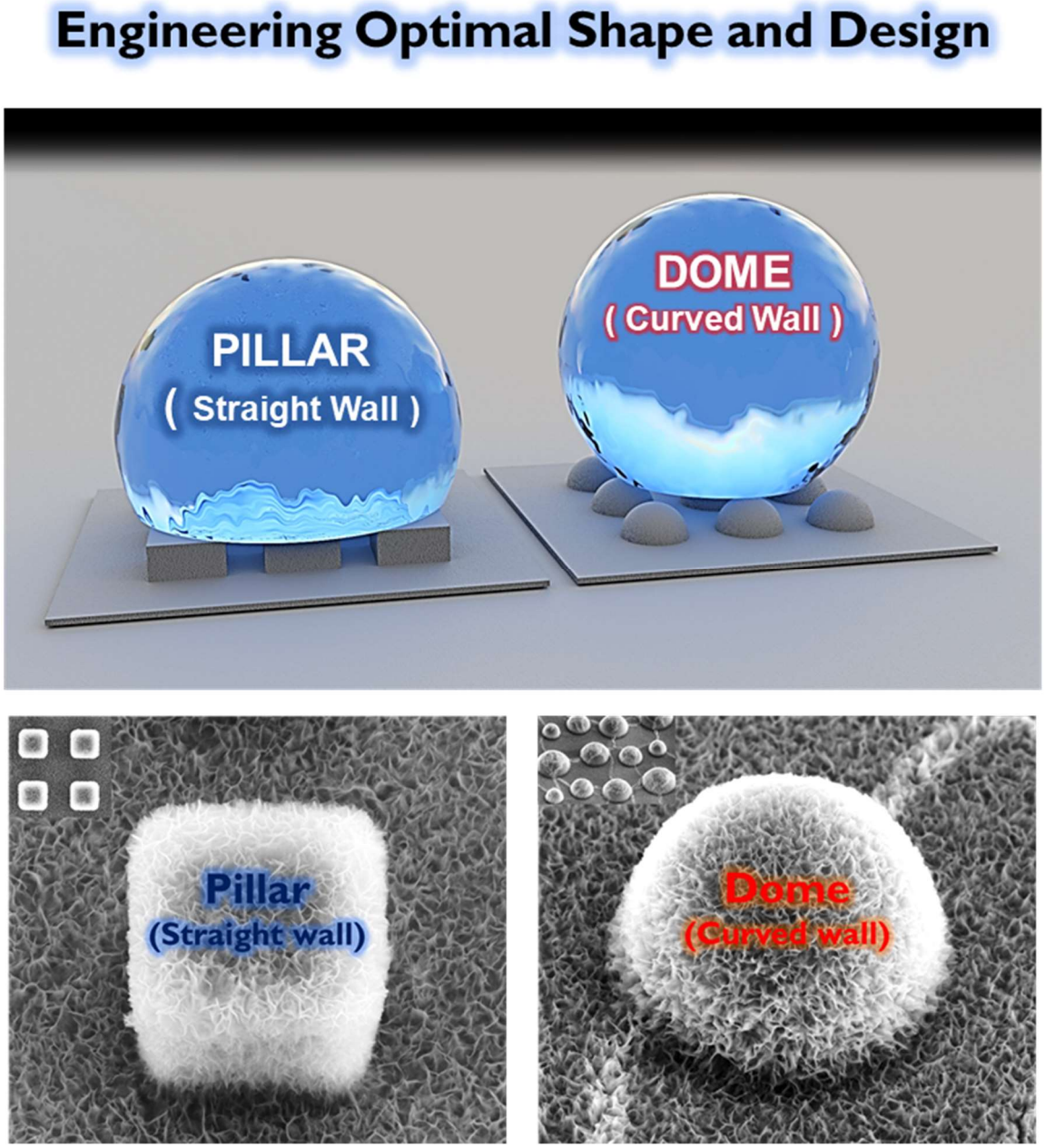

Figure 3.1. An overview of our results. Inspired by the lotus leaf which has an array of micro-sized domes with nano-sized hairy structures, we engineered the water repellent surface with micro and nano hierarchical structures using a standard single-layer photolithography and a simple hydrothermal bottom-up synthesis. Based on our investigations, the micro-domes with zinc oxide nanoporous structure exhibited much higher superhydrophobicity and much easier water removal when compared to the micropillars with the zinc oxide nanoporous structure

3.2 Photolithography mask design, and PDMS double casting method

Table 3-1 shows the scale by scale comparison between *Nelumbo nucifera* surface and our double hierarchical micro-dome surface. *Nelumbo nucifera* has the distinguishing hierarchical structure of micro-papillae with dense coating of nanosized hairy structure made up of epicuticular wax (*Nonacosanediols*). In this study, we precisely designed the two different classes of hierarchical surface (sharp-tipped vertical walled pillars and curved micro-bumps): array of micro-pillar and micro-dome via a standard single layer photolithography followed by reflow (for dome structure only), conformal growth of zinc oxide nanostructure, and the surface hydrophobic termination of fluorosilane treatment.

Basic Design Rule - Comparison

	Lotus Leaf (*Nelumbo nucifera*)	**Our Hierarchical Surface (This project)**
Micro-Structure	Micropapillae (with Various Tip Radii)	Micro-Pillar / Micro-Dome (Various Aspect Ratio)
Nano-Structure	Nanosize Wax Crystal	ZnO Nanostructure
Chemical Coating	Epicuticular Wax (Nonacosanediols)	Fluoro-Silane (1H,1H,2H,2H-Perfluorooctyltrichlorosilane)

Table 3.1. Scale- by scale comparison between *Nelumbo nucifera* surface and our hierarchical surface.

For the detailed methods, two Mylar transparency masks were prepared: one with square arrays of square features, to produce the sharp-tipped pillars, and the other with square arrays of circular features, to produce the micro-dome arrays. Each mask contained 16 different pattern arrays sized 15 mm × 15 mm, covering every combination of the

feature side-length or diameter set {20, 30, 40, 50} μm with inter-feature spacings of 0.5, 1.0, 1.5 and 2.0 times the feature size (Figure 3.2 and Table 3.2).

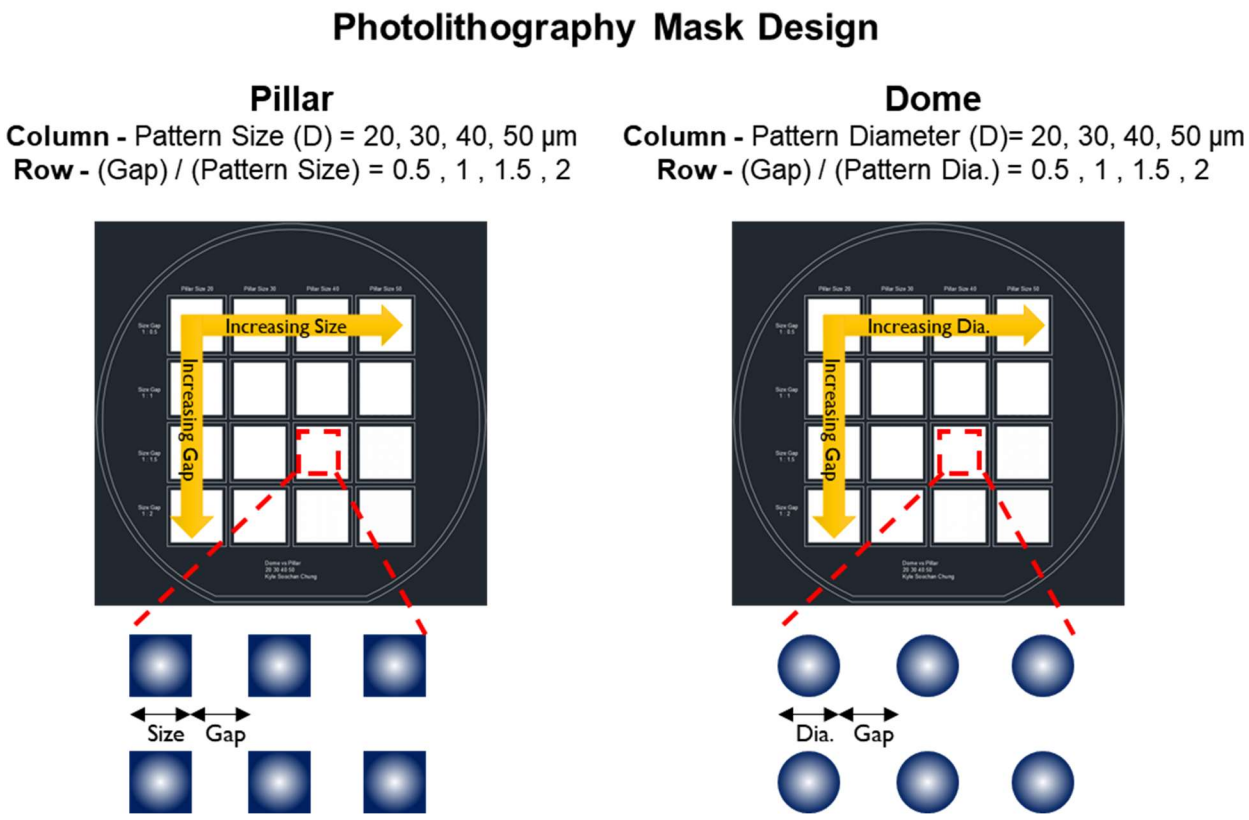

Figure 3.2. Two different photolithography mask designs (Mylar transparency masks) of micro-pillars and micro-domes with various sizes and spacings

Two 100 mm-diameter silicon wafers were cleaned by sonication in acetone and isopropanol, rinsed with deionized (DI) water, and dehydrated at 150 °C on a hotplate for 15 min. Then, the wafers were oxygen plasma-treated at 70 W, 200 mTorr for 5 min (O2 plasma system, Plasma Equipment Technical Services (PETS) Inc.). An adhesion promoter, hexamethyldisilazane (HMDS, Sigma-Aldrich), was vapor-phase coated onto the silicon wafers for 5 min.

AZ P4620 photoresist (PR) was spin-coated onto one of the wafers at 300 rpm for 19 sec, attained at a ramp rate of 50 rpm/s, followed by 850 rpm for 39 sec, attained at 100 rpm/s, with a target thickness of 20 μm. The coated wafer was soft-baked at 90 °C for 30 min. To prevent cracking of the PR, the wafer was placed in a dark room for 10 min at 30–

50% relative humidity to rehydrate. This wafer was then exposed, using the square-pillar mask design, to 500 mJ/cm2 i-line (365 nm) UV in a contact mask aligner (Model 200, OAI) and developed for 5 min with AZ 1400K diluted 1:3 by volume in DI water. The developed wafer was rinsed with DI water and treated with O2 plasma at 60 W, 200 mTorr for 10 min (O2 plasma system, Plasma Equipment Technical Services (PETS) Inc.) to descum it.

Unit [μm]	Pattern 20 μm	Pattern 30 μm	Pattern 40 μm	Pattern 50 μm
Pattern : Gap 1 : 0.5	P : 20 G : 10	P : 30 G : 15	P : 40 G : 20	P : 50 G : 25
Pattern : Gap 1 : 1	P : 20 G : 20	P : 30 G : 30	P : 40 G : 40	P : 50 G : 50
Pattern : Gap 1 : 1.5	P : 20 G : 30	P : 30 G : 45	P : 40 G : 60	P : 50 G : 75
Pattern : Gap 1 : 2	P : 20 G : 40	P : 30 G : 60	P : 40 G : 80	P : 50 G : 100

Table 3.2. Table of various pattern sizes (for micro-pillar) or diameters (for micro-dome) and spacings in our photolithography masks.

This wafer was then baked at 135 °C for 1 hour, triggering a thermal reflow driven by the PR's surface tension to obtain curved micro-dome features. The heights of the reflowed geometries ranged between 16.5 and 25.0 μm as determined by electron microscopy and stylus profilometer (Dektak 3030). To match the heights of the micro-pillar structures to those of the reflowed domes, a different spin coating speed was used: 1000 rpm instead of 850 rpm, based on the resist manufacturer's spin curve. The other

lithographic process steps were as above, but without thermal reflow step. Vertical-walled PR features resulted, and the resist height was confirmed to be 16.75 ± 0.20 µm with a surface profilometer (Dektak 3030).

In order to achieve the same structure from the result of our photolithography process, replicas of the micro-pillar and micro-dome structures were created in polydimethylsiloxane (PDMS, Sylgard 184, Dow Corning) via two-stage casting.[42]

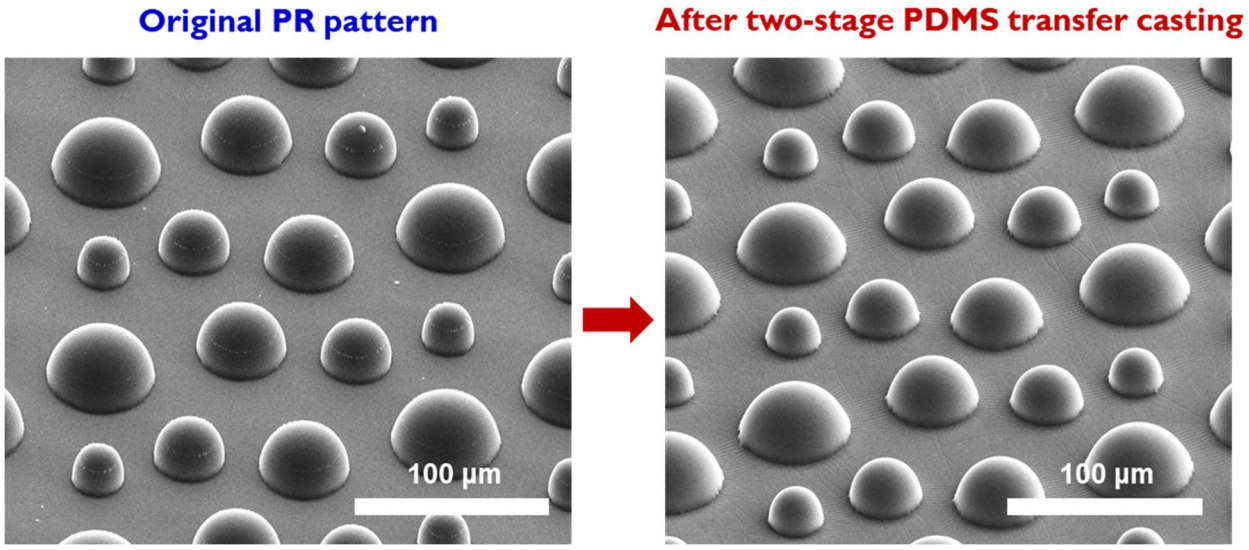

Figure 3.3. The scanning electron microscope (SEM) image of our two-stage PDMS casting result

In the first casting step, the PDMS pre-polymer and crosslinker were mixed in the ratio 5:1 and poured onto the wafer. After curing at 70 °C for 2 hours, this casting was oxygen plasma-treated (60 W, 200 mTorr, 2 min) and silanized with 1H,1H,2H,2H-perfluorooctyltrichlorosilane (Sigma-Aldrich). This casting served as the mold for a second casting step using a less rigid mixture of PDMS (pre-polymer:crosslinker :: 10:1).

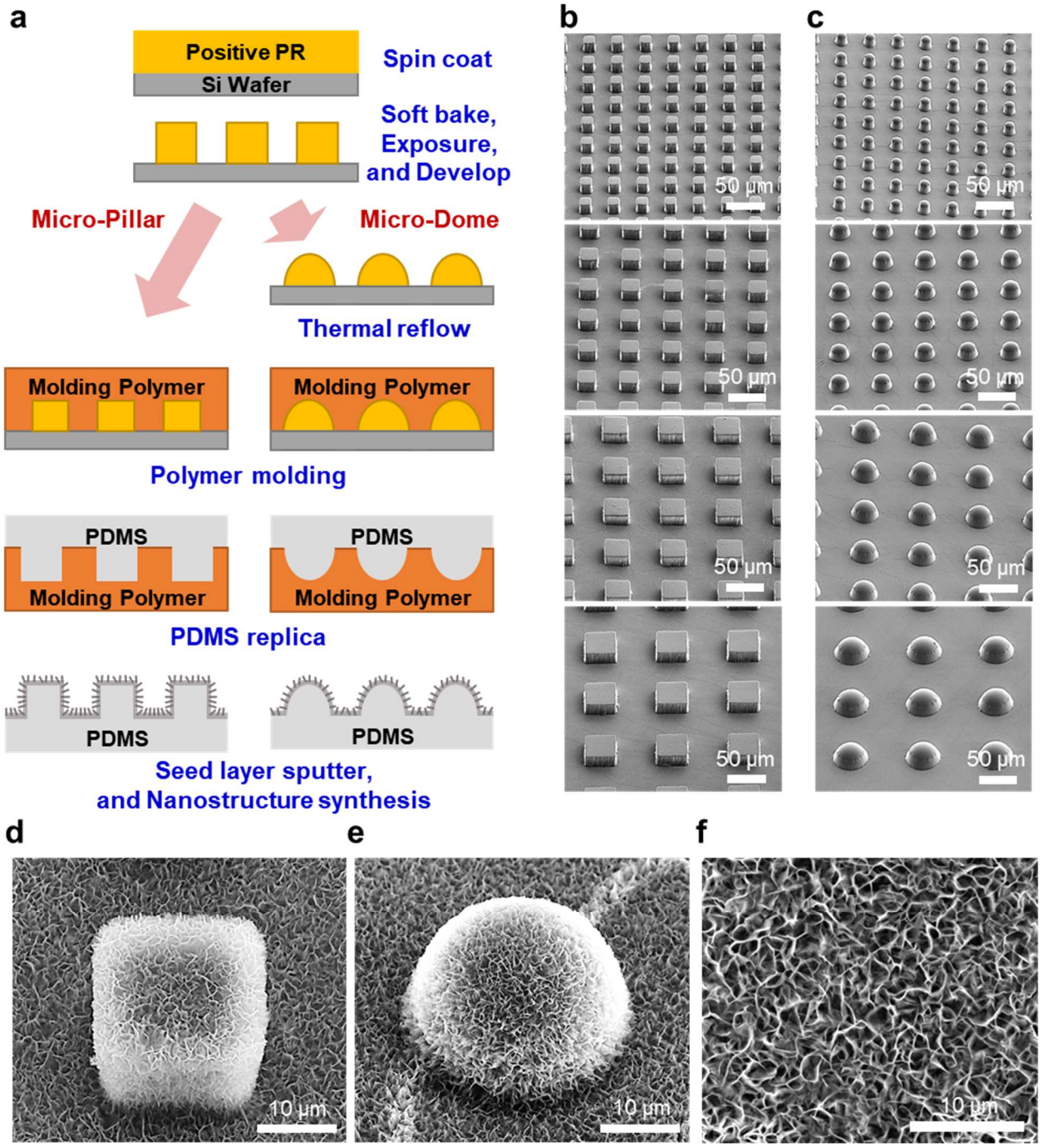

Figure 3.4. Fabrication and characterization of hierarchical structures. (a) Process flow for both dome and square pillar arrays; (b) Scanning electron microscope (SEM) images showing micro-pillar arrays with pattern sizes of (from top to bottom) 20 μm, 30 μm, 40 μm, 50 μm. Gap-to-pattern size ratio was 1 in all cases. Scale bar: 50 μm; (c) SEM images showing micro-dome arrays with the same set of pattern and gap sizes as (b); (d, e) SEM images of a representative square pillar (d) and dome (e), showing the nanoscale porosity of the deposited ZnO film. Scale bar: 10 μm; (f) Enlarged view of nanoporous ZnO coating. Scale bar: 10 μm.

Next, the microstructured PDMS substrates were sputtered with 10 nm Cr followed by 150 nm 99.999%-pure aluminum to support the hydrothermal synthesis of porous ZnO. The growth of ZnO followed our previously reported process[31], in which the aluminum-coated PDMS was immersed in a 25 mM equimolar aqueous solution of zinc nitrate ($Zn(NO_3)_2$ ▪ 6 H_2O, Sigma-Aldrich) and hexamine (hexamethylenetetramine, Sigma-Aldrich) at 70 °C for 90 minutes in an oven. Following this bath synthesis, samples were rinsed in DI water, dried in a jet of N_2, and stored at room temperature. Electron micrographs of the resulting nanostructures are shown in Figure 3.4d, 4e, and 4f.

As the final step, we applied fluoro-ilane treatment to our hierarchical surface. Sample surfaces were cleaned with oxygen plasma (60 W, 200 mTorr, 2 min). To achieve surface superhydrophobicity, samples were then immediately placed in a vacuum desiccator with 100 μL of 1H,1H,2H,2H-perfluorooctyltrichlorosilane (Sigma-Aldrich), pumped down for 20 minutes and left to rest for 40 minutes. Samples were rinsed with DI water and allowed to 'cure' at room temperature in a fumehood for 24 hours.[41]

3.3 Overview of our structures, fabrication process, and surface morphology characterization

In this study, we empirically investigated the relationship between surface microstructure geometry and water droplet behavior for surfaces covered with domes and square pillars. The fabrication process for domes (Figure 3.4a) relies on the thermal re-flow of a single, patterned photoresist layer in which the surface tension of heated photoresist drives an energy minimization to create features with curved surfaces. A two-stage elastomeric casting process creates replicas of these microstructures, which are then sputtered with an aluminum seed layer and coated with a nanoporous ZnO film via immersion in a heated equimolar aqueous zinc nitrate/hexamine solution. This process flow allowed structures with a range of micro- and nano-scale features to be prototyped rapidly. A total of 16 micro-dome patterns were tested (e.g. Figure 3.4c), covering each possible combination of the pre-reflow feature diameters of {20, 30, 40, 50} μm with gap-to-diameter ratios of {0.5, 1.0, 1.5, 2.0}. A set of patterns was also fabricated without the thermal re-flow step, to provide square pillars with sharper corners for comparison (Figure 3.4b).[41]

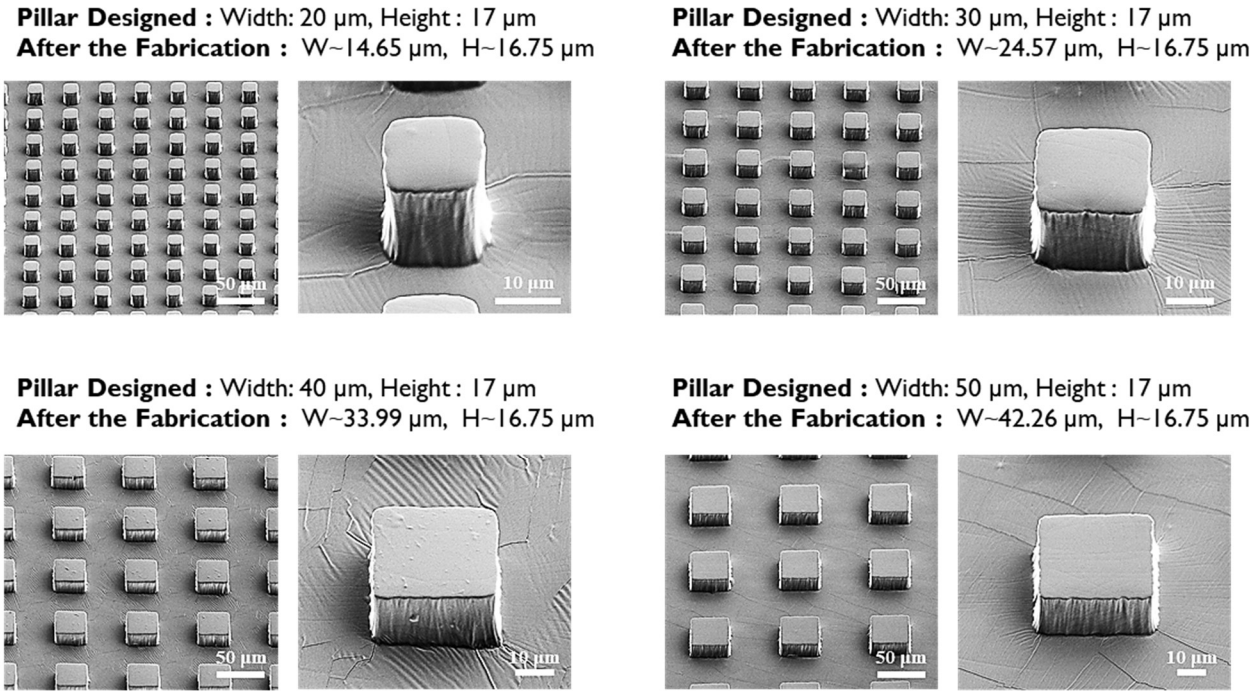

Figure 3.5. Scanning electron microscope images of the of micro-pillar with various sizes. The pattern sizes (i.e. square width of the top surface) were 20, 30, 40, 50 µm, with the uniform average height of 16.75 µm.

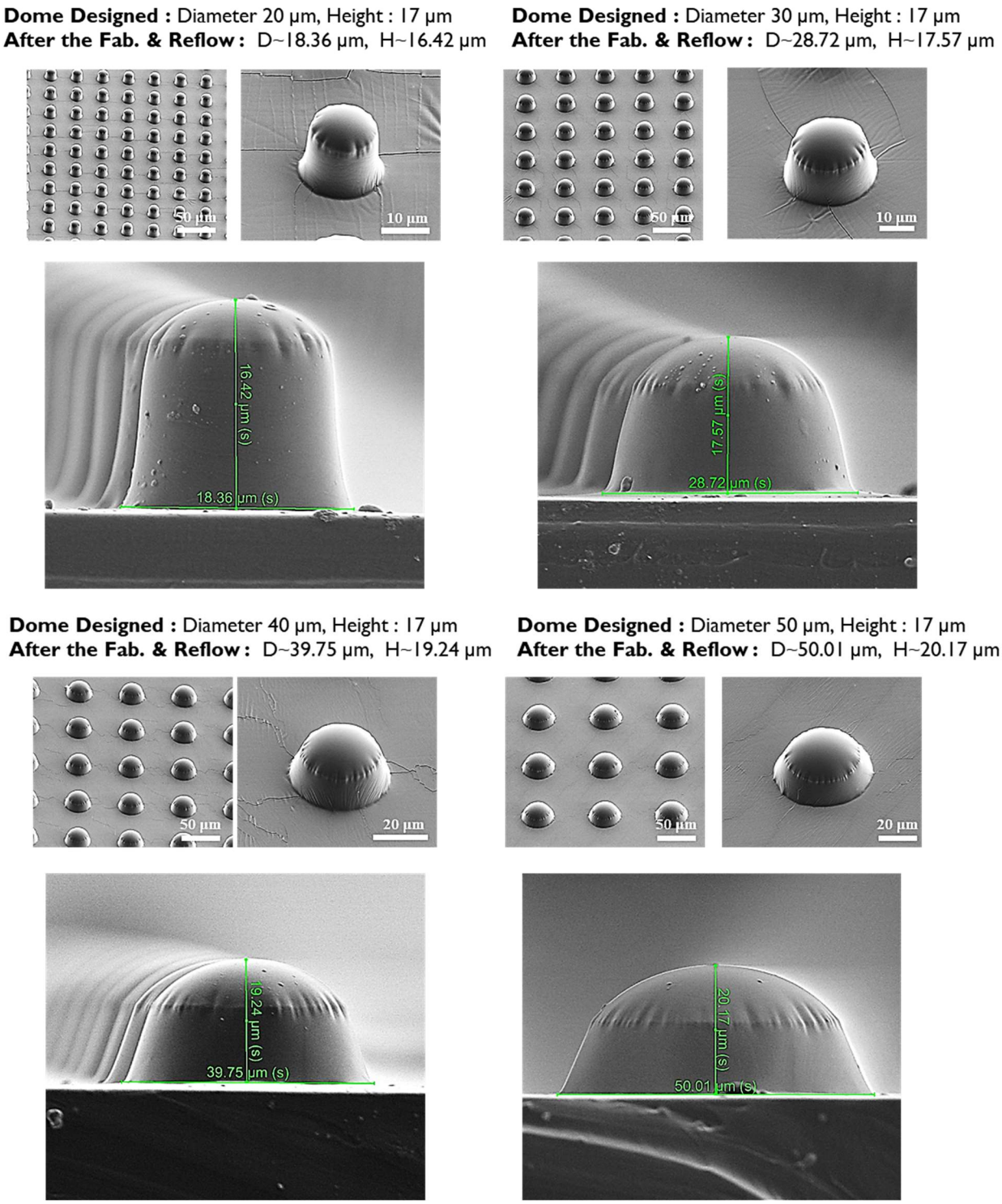

Figure 3.6. Scanning electron microscope images of the of micro-dome with various sizes. The pattern diameters (i.e. circular diameter of the bottom surface) were 20, 30, 40, 50 µm, with the average center heights of 16.52, 17.57, 19.88, 25.01 µm, and the radii of curvature of the apex were 9.02, 12.52, 18.16, 25.39 µm.

3.4 Water sessile contact angles on arrays of square-tipped pillars and micro-domes

Static, advancing, and receding water contact angles were measured using a custom-built goniometer. Five droplets (7.5 µL) were sequentially deposited onto different parts of each sample surface and measured. Video images were captured of each droplet, viewed from the edge of the substrate using a Thorlabs DCC1645C camera with a 25 mm focal-length plano-convex lens. Images were analyzed in ImageJ[43]. Static contact angles were extracted using the Low-Bond Axisymmetric Drop Shape Analysis (LB-ADSA) ImageJ plug-in,[44] which fits the Young–Laplace equation to image data. The sample stage was then tilted until the droplet rolled off, and the Dropsnake ImageJ plugin[45] was used to extract advancing and receding contact angles from the video frame captured immediately prior to roll-off. Hysteresis is defined as the difference between advancing and receding angles.

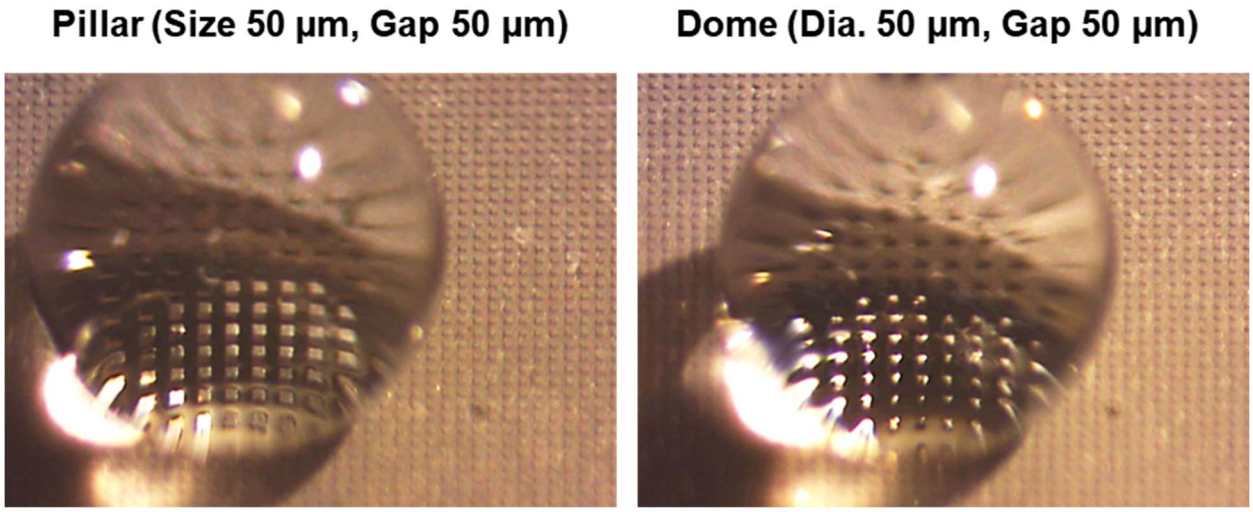

Figure 3.7. Tilted view of optical microscope image during our static contact angle measurements: micro-pillar (left), and micro-dome (right).

Optical microscopy of water droplets resting on the micropatterned surfaces indicated that they remained suspended on the tips of the structures and did not infiltrate the gaps between microfeatures (Figure 3.7). All of the microstructured surfaces tested — including pillar and dome arrays — showed higher average static water contact angles (Figure 3.8) than a microscopically flat surface processed in the same batch of samples and bearing only the nanoporous ZnO film. The micro-dome arrays, however, performed significantly better than the square pillars for any given nominal feature size and spacing.

These general differences are compatible with existing conceptions of the role of partial liquid–solid contact.[3,27] Adding any sort of microstructure is expected to reduce both linear and areal liquid–solid contact fractions, provided that the droplet is suspended on the tips of the microstructure.

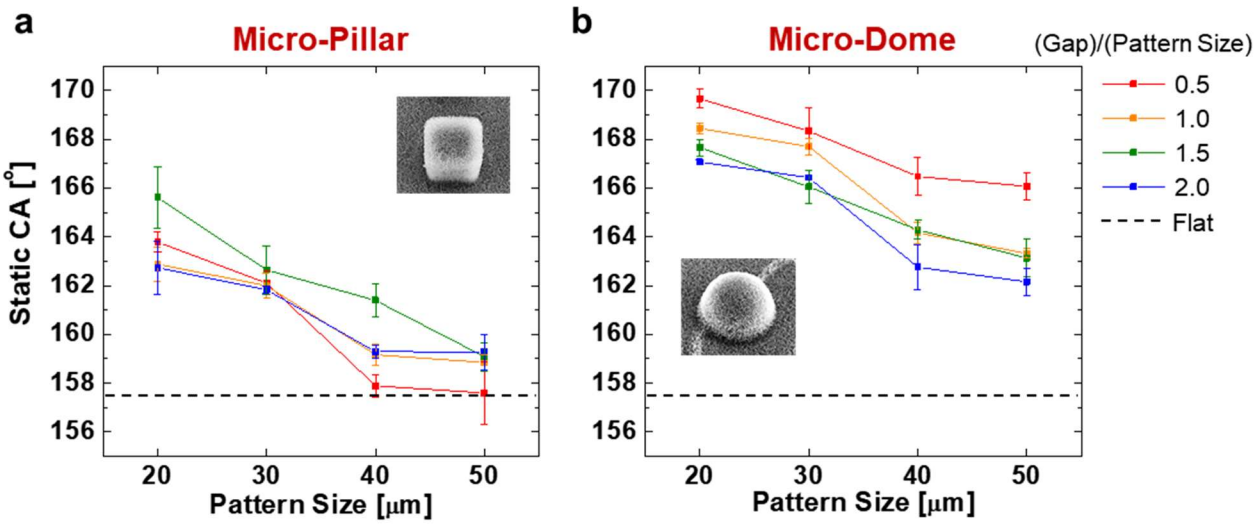

Figure 3.8. Water sessile contact angles on arrays of (a) square-tipped pillars and (b) micro-domes, both covered with a fluorosilanized ZnO nanoporous coating. Contact angles are plotted against feature diameter ('pattern size') for varying gap-to-pattern-size ratio. Error bars represent ±1 standard error of the mean; five droplets per specimen. 'Flat' denotes the contact angle on a surface with the fluorosilanized ZnO coating but no microfeatures. Contact angle of the flat surface was measured to be approximately 157°

Pillar	**Experimental Contact Angles (Average)**			
Gap/Pattern size	**Pattern size 20**	**Pattern size 30**	**Pattern size 40**	**Pattern size 50**
0.5	163.7802	162.104	157.8964	157.5932
1	162.8778	161.9942	159.169	158.8464
1.5	165.608	162.6402	161.3994	159.0768
2	162.734	161.8244	159.2912	159.2784

Table 3.3. Result of water sessile contact angle measurement on the micro-pillar pattern

Dome	Experimental Contact Angles (Average)			
Gap/Pattern size	Pattern size 20	Pattern size 30	Pattern size 40	Pattern size 50
0.5	169.6648	168.3318	166.4708	166.0682
1	168.4452	167.6994	164.1576	163.3156
1.5	167.6628	166.0472	164.293	163.1308
2	167.0668	166.4322	162.751	162.157

Table 3.4. Result of water sessile contact angle measurement on the micro-dome pattern

Furthermore, the curvature of the domed features makes it possible for only a small region at the tip of each dome to be in contact with the liquid, whereas the entire upper surface of a flat-tipped square pillar beneath a droplet is expected to be in contact with the liquid.

There are two trends, however, that cannot be simply explained by either the contact area fraction-based Cassie–Baxter model[3] or by a model based on a linear contact fraction.[27] The first trend is a scale dependence: average contact angle reduced by about 4–5° as the nominal feature size grew from 20 to 50 μm, for a fixed gap-to-size ratio. This trend is unexpected, since no model that considers only a solid–liquid contact fraction can explain this dependence, and indeed previous experimental results from Hisler *et al.*[40] showed no such scale dependence for flat-topped pillars with widths of 4–128 μm.

A second unexpected trend is seen in the micro-domed samples: in general, as the gap-to-size ratio increased from 0.5 to 2, the average contact angle decreased by about 3–4° for a given pattern size. This trend is the opposite of what might be anticipated from existing models and prior experiments with square pillar arrays,[46] since spacing features of a particular size further apart would usually reduce both the linear and areal contact fractions and hence be expected to raise the apparent contact angle. A possible explanation is that the contact area within each individual dome increased as the domes were spaced further apart, since a greater fraction of the droplet's weight would have needed to be carried by each feature. The highest static contact angle obtained in this work, 169.7±0.4° (mean ± standard error of the mean, N = 5), occurred when the domes had the smallest diameter (20 μm) and gap (10 μm), and is slightly superior to the 164° measured from

natural lotus leaves.[26] This optimal result was more than 10° higher than obtained with the 'flat' (nanostructure-only) surface.[41]

3.5 Analytical modeling and theoretical calculation of apparent contact angle based on the Cassie–Baxter model

For comparison with the results of our experiments, we performed a theoretical calculation of apparent contact angle based on the conventional Cassie–Baxter model. Similar to previous work, and supported by existing models and prior experiments with square pillar arrays, we assumed the local contact angle at the solid–water touching region to be the contact angle of water on a flat surface (no microstructure) with a ZnO nanoporous structure synthesized on it, which was measured to be approximately 157°. The liquid–air interface between the solid–liquid touching regions is assumed to be parallel to the ground while the local contact angle at the contact region remains the same. Based on these assumptions and side-view scanning electron microscope (SEM) images of our micro-dome structures, the solid–liquid touching area was calculated first.

From the previous study on the statistical analytical model of the ZnO nanoporous structure was reported from our lab[47],

$$\cos\theta^*_{nanopore} = \phi_f r_n \cos\theta_0 - (1 - \phi_f) \tag{3.2}$$

$$\cos\theta^*_{nano} = \phi_{tn} \cos\theta_0 + (1 - \phi_{tn})(\cos\theta^*_{nanopore}) \tag{3.3}$$

$$\cos\theta^*_{nano} = \phi_{tn} \cos\theta_0 + (1 - \phi_{tn})[\phi_f r_n \cos\theta_0 - (1 - \phi_f)] \tag{3.4}$$

where:

$\theta_0 = 105^o$ (contact angle on flat surface of same chemistry of zinc oxide);

$\phi_f = 0.018606$ (fraction of nanopores filled with water);

$\phi_{tn} = 0.0051$ (area fraction of ZnO nanoporous strucuture's tips);

$r_n = 3.5$ (surface roughness of ZnO nanoporous structure excluding the tip area).

Similarly, we modified the hybrid equation above to our microstructure cases, but the basis contact angle of our equation was now θ^*_{nano}, rather than θ_0 used in the above study, since the local contact surface of our structure was the ZnO nanoporous structure.

$$\cos\theta^*_{micro} = \sum \phi_i r_i \cos\theta_i \tag{3.5}$$

$$= \phi_m r_{mt} \cos\theta^*_{nano} + (1 - \phi_m)[\phi_{fm} r_{mp} \cos\theta^*_{nano} - (1 - \phi_{fm})] \tag{3.6}$$

$$= \phi_m r_{mt} \cos\theta^*_{nano} + (1 - \phi_m)\,, \tag{3.7}$$

($\because \phi_{fm} = 0$, since water did not infiltrate the graps between micro-features.)

where:

r_{mt} is surface roughness of the micro-structure' tip area (or, ratio of "actual" wetted touching area to projected wetted touching area; thus, the $r_{mt} = 1$ for micro-pillar, $r_{mt} > 1$ for micro- dome);

r_{mp} is surface roughness of microstructure excluding the wetted tip area;

ϕ_m is the ratio of the wetted tip area to the actual area of the unit cell;

ϕ_{fm} is a fraction of micropores filled with water, which in our case '0' (no pore wetted);

Based on the equations above, we calculated the theoretical contact angles for all of our 16 different micro-pillars and 16 different micro-domes.

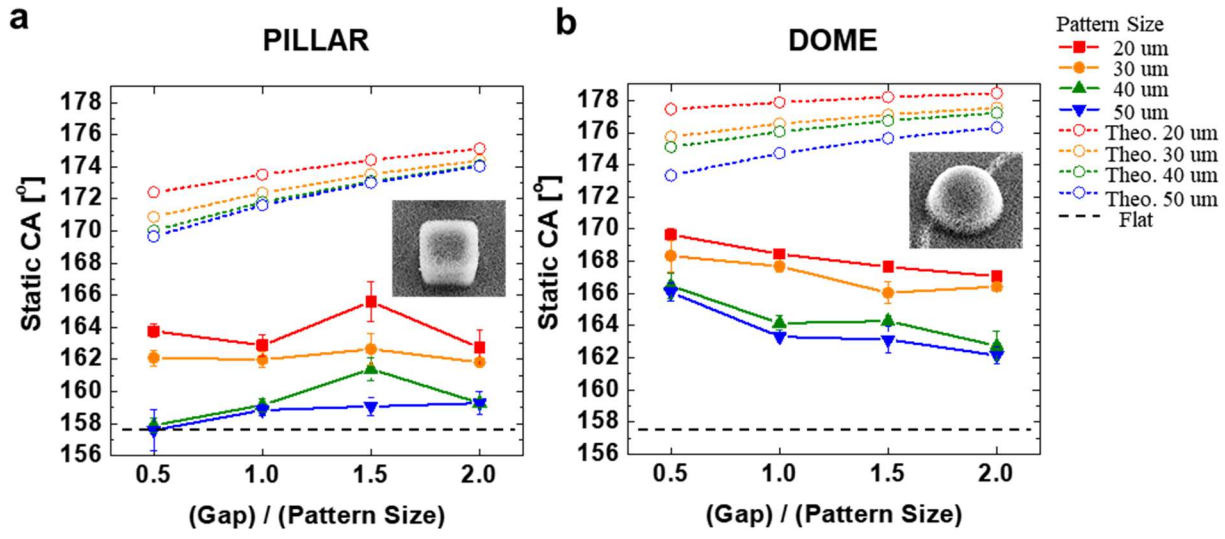

Figure 3.9. Theoretical and experimental water sessile contact angle distribution of various pattern sizes and spacings, and comparison between micro-pillar and micro-dome. (a) Plot of water contact angle (CA) versus the ratio of the gap to micro-pillar pattern size. (i.e. square width of the top

surface). (b) Plot of water CA versus the ratio of the gap to micro-dome pattern size. Solid lines are experimental measurements and dotted lines are theoretical calculation using the Cassie–Baxter model. (All the samples are the hierarchical surfaces with micro and nano structures, while the "Flat" means the sample with the ZnO nanoporous structure on flat surface with no microstructures.)

Pillar	**Theoretical Contact Angle Values**			
Gap/Pattern size	**Pattern size 20**	**Pattern size 30**	**Pattern size 40**	**Pattern size 50**
0.5	172.4143	170.8891	170.0366	169.6718
1	173.5252	172.3809	171.8035	171.6193
1.5	174.4253	173.5296	173.1109	173.0141
2	175.1408	174.412	174.0901	174.038

Table 3.5. Theoretical calculation of contact angle based on Cassie-Baxter model for micro-pillar case

Dome	**Theoretical Contact Angle Values**			
Gap/Pattern size	**Pattern size 20**	**Pattern size 30**	**Pattern size 40**	**Pattern size 50**
0.5	177.4588	175.7519	175.1093	173.341
1	177.8825	176.545	176.0668	174.7116
1.5	178.2059	177.1161	176.7383	175.6453
2	178.4529	177.5367	177.2252	176.311

Table 3.6. Theoretical calculation of contact angle based on Cassie-Baxter model for micro-dome case

The plot above shows that different trends in theoretical values were observed compared to our experimental data. The theoretical values not only had higher contact angles than any results from our experiments but also the dotted line shows an increasing trend with increasing gap-to-pattern size ratio. We believe the conventional Cassie–Baxter equation[3] cannot be applied since it does not include gravity (i.e. the water droplet's weight), which can sag the droplet closer to the ground and increase solid–liquid contact area. From the beginning, the liquid–air interface between the solid–liquid touching regions is assumed to be parallel to the ground while the local contact angle at the contact region remains the same (approximately 157°). As a result, the patterns with the larger spacing are regarded as having less solid–liquid touching area; this would give us a higher apparent contact angle based on the conventional Cassie–Baxter model.

However, in our experiment, the local region of solid–liquid contact on the micro-dome surface was not parallel to the ground due to the weight of the droplet and the dome's curved contour, where the normal force to the droplet's weight is exerted. Thus, unlike in all the lithographically defined vertical-side-wall cases, the equilibrium of the water droplet on the micro-dome can be similar to the droplet advancing down on the tilted surface. As a result of our experiment, the micro-domes with the larger spacing, in fact, had the larger solid–liquid contact area, and thus yielded the lower apparent contact angle. We believe this physical understanding can be the reason why the trends from our experiments were divergent from the conventional analytical model.

3.6 Dynamic contact angle measurement of various pattern sizes and spacings, and comparison between micro-pillar and micro-dome

Contact angle hysteresis was lower for both domed and pillared surfaces than for a flat surface (Figure 3.10). Lower hysteresis is associated with greater ease of droplet shedding[27,33], suggesting that these microstructures may be attractive for enhancing condensate removal from a surface. The micro-domed surfaces showed consistently lower hysteresis values than square-pillared surfaces with equivalent diameters and spacings. As with the static contact angle results, smaller features and smaller gaps yielded more desirable performance in the micro-domed surfaces: the lowest hysteresis obtained was 14.7±1.3° for 20 μm-diameter domes spaced by 10 μm, whereas the hysteresis on a flat surface was far higher, at 39.0±0.4°.[41] (For comparison, the hysteresis of the lotus leaf has been reported to be 3°.[26]) A scale-dependence was evident in the square-pillar arrays as well, with smaller pillars almost always offering lower hysteresis at any given gap-to-size ratio. Such a scale dependence was not seen, in contrast, in the experiments of Yeh[48] in

which square-tipped silanized silicon pillars ranging from 3 – 9 μm in size were tested. The improvements in hysteresis achieved by patterning the surfaces are attributable to increased receding contact angles (Figure 3.10b, and 10d); the advancing angles remained very close to that of a flat surface. The dominant role of the receding angle is consistent with, e.g., Dorrer's and Rühe's experimental results for square pillars[49].

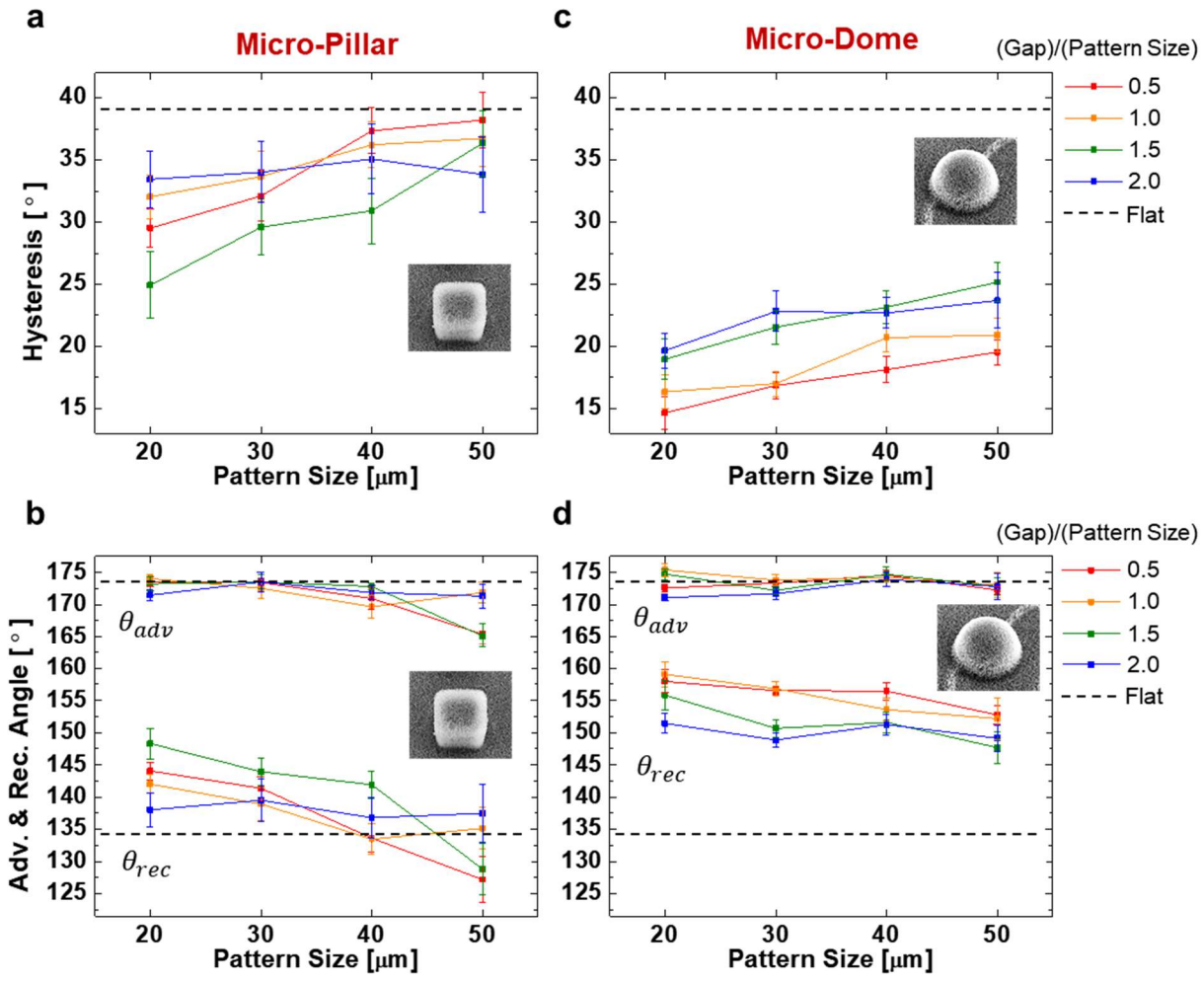

Figure 3.10. Contact angle hysteresis and advancing and receding contact angles for arrays of (a, b) square pillars and (c, d) domes, all covered with a fluorosilanized ZnO nanoporous coating. Results are plotted against pattern size for a range of gap-to-pattern-size ratios. Error bars represent ±1 standard error of the mean; sample size is five separate droplet sheddings per specimen. 'Flat' denotes the corresponding results on a surface with the fluorosilanized ZnO coating but no microfeatures. The hysteresis on a flat surface was measured at 39.0°.

Pillar	Experimental Contact Angle Hysteresis (Average)			
Gap/Pattern size	Pattern size 20	Pattern size 30	Pattern size 40	Pattern size 50
0.5	29.5212	32.1040	37.3460	38.2136
1	32.0322	33.6656	36.2164	36.7472
1.5	24.9244	29.5944	30.9148	36.3386
2	33.4512	34.0144	35.0738	33.8354

Table 3.7. Result of contact angle hysteresis on the micro-pillar pattern

Dome	Experimental Contact Angle Hysteresis (Average)			
Gap/Pattern size	Pattern size 20	Pattern size 30	Pattern size 40	Pattern size 50
0.5	14.6506	16.8458	18.1310	19.5420
1	16.3476	16.9992	20.6908	20.9114
1.5	18.9634	21.5480	23.1572	25.1670
2	19.6652	22.8240	22.7000	23.6980

Table 3.8. Result of contact angle hysteresis on the micro-dome pattern

3.7 Conclusion

This study suggests that micro-scale domes can usefully be added to a surface to increase static water contact angle by at least 12° and reduce contact angle hysteresis by at

least 24° relative to a flat surface with a comparable nano-scale surface structure and chemistry. Best performance was obtained with the smallest (20 μm) and most closely spaced (10 μm) domes tested, suggesting that it would be useful to investigate whether further reducing dome size or spacing could increase the performance even more. The strong feature-size dependences that we have observed of both static contact angle and hysteresis are absent in much previous work, such as Hisler's[40], Yeh's[48] and Lv's[49]. That previous work was conducted on microscale pillar arrays without a secondary nanostructure, and it is possible that addition of the nanostructured film to our surfaces may, by roughening the edges of the micro-scale pillars, render the pillars' sizes more critical to the overall surface performance.

High static contact angles and low hysteresis and are widely associated with dropwise condensation and more effective droplet shedding respectively, suggesting that it may be possible to apply these geometries to enhance condensate shedding from evaporator coil surfaces during the cooling of moist air. The structures tested here involved depositing a thin aluminum layer onto an elastomeric substrate, but for heat transfer applications similar structures might be fabricated at scale in bulk aluminum alloy by, e.g., coining or knurling. The demonstrated process therefore represents a step towards scalable manufacturing of practicable, water-repelling materials.[41]

Chapter 4. Condensation Performance with Optimal Shape and Design

4.1 Introduction and motivation

Heating, ventilating, and air-conditioning systems account for 10−20% of the total energy consumption of many developed countries, and air conditioning in particular is driving rapidly increasing electricity consumption in emerging economies.[16,50] Condensation phase change is a critical phenomenon to understand and control in air conditioning because atmospheric water may condense onto cooling surfaces, and the latent heat of vaporization of water is large enough to constitute a substantial fraction of the cooling load of a system. Controlling condensation is also important in desalination, atmospheric water harvesting, and refrigeration, among other applications.[39,51–53]

Water that condenses on a cooled surface may do so in either a filmwise or a dropwise mode, depending on the chemical and morphological characteristics of the surface (Figure 4.1 and 4.2). It has been widely demonstrated that dropwise condensation offers up to 5–10 times better heat transfer performance than filmwise condensation, because dropwise water shedding continually clears regions of the surface and enables further droplet nucleation and growth to occur.[52]

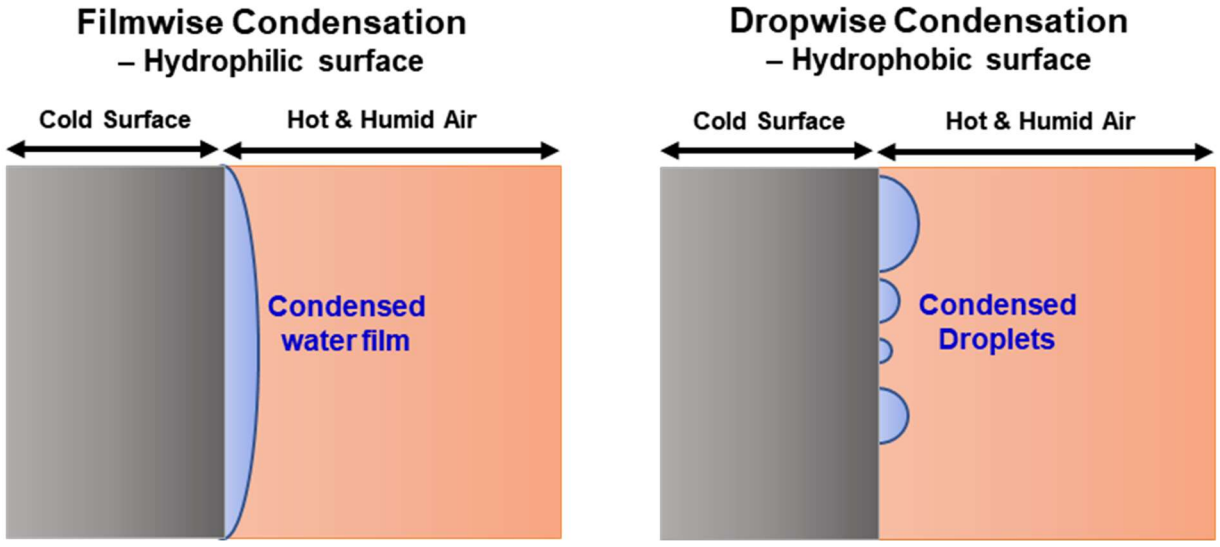

Figure 4.1. Schematic comparison of a filmwise and dropwise condensation modes

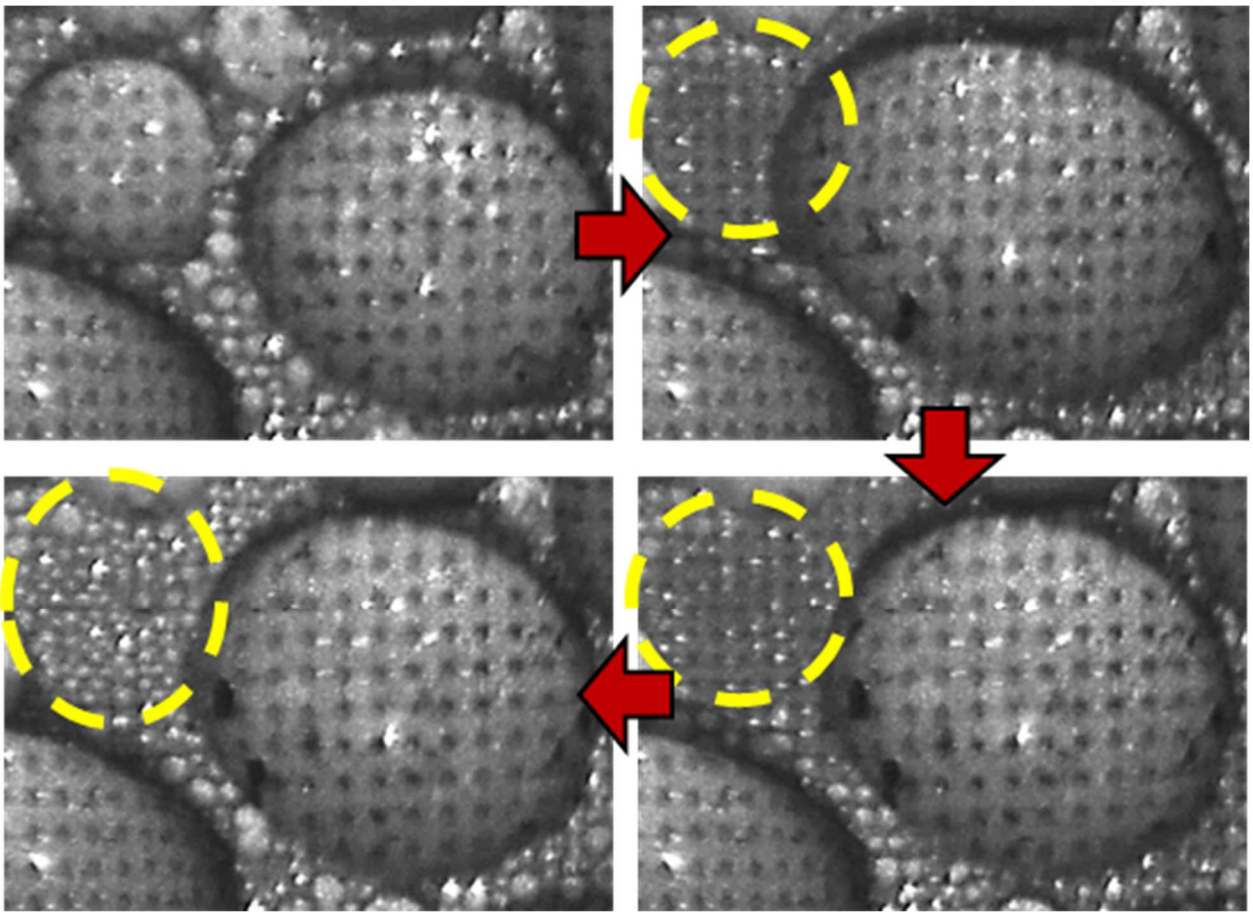

Figure 4.2. When the humid vapor hits the cold (surface temperature lower than the saturation temperature) surface, condensation occurs. When two adjacent droplets touch each other, droplet merging (or coalescence) happens and thereby creates fresh cold surface re-exposed to the humid air for further condensation and new droplets grow.

The role of chemical composition can be understood through surface energy. Higher-surface-energy materials will exhibit more hydrophilic behavior and tend to form water films with low contact angles. Lower-surface-energy materials—for example, highly fluorinated molecules—will exhibit more hydrophobic behavior and water will tend to support droplets with contact angles greater than 90°. The role of surface morphology, meanwhile, is more complex. Roughening an already hydrophobic surface can increase its apparent water contact angle when liquid fully penetrates the surface texture, as originally highlighted by Wenzel.[13] 'Composite' or suspended interfaces, meanwhile—in which the base of a droplet makes contact only with the protruding regions of a roughened surface, as originally described by Cassie and Baxter[3]—can offer even higher water contact angles and open up the superhydrophobic regime of surface performance (static contact angles > 150°). The suspended mode is encountered in many natural leaves, such as the lotus, and has often been associated with lower contact angle hysteresis than Wenzel wetting and

hence easier droplet shedding under gravity or in flowing air. With the addition of micro-, nano-, or multi-scale surface roughness, contact angles approaching 180° have been achieved.[25,54]

Considering such idealized equilibrium droplet contact modes does not, however, fully predict the complete condensing performance of a surface, because effective shedding of condensed droplets is required, and not simply high static contact angles. The specific shapes and length-scales of surface protrusions are crucially important, with sharp edges and corners tending to pin droplets in place on a surface and impede shedding. The dynamics of condensation itself also need to be understood: condensation may nucleate deep within the pores or recesses of a surface, so that a droplet might not ultimately attain a suspended, composite-contact mode even if that would, in principle, be its lowest-energy state.[55,56]

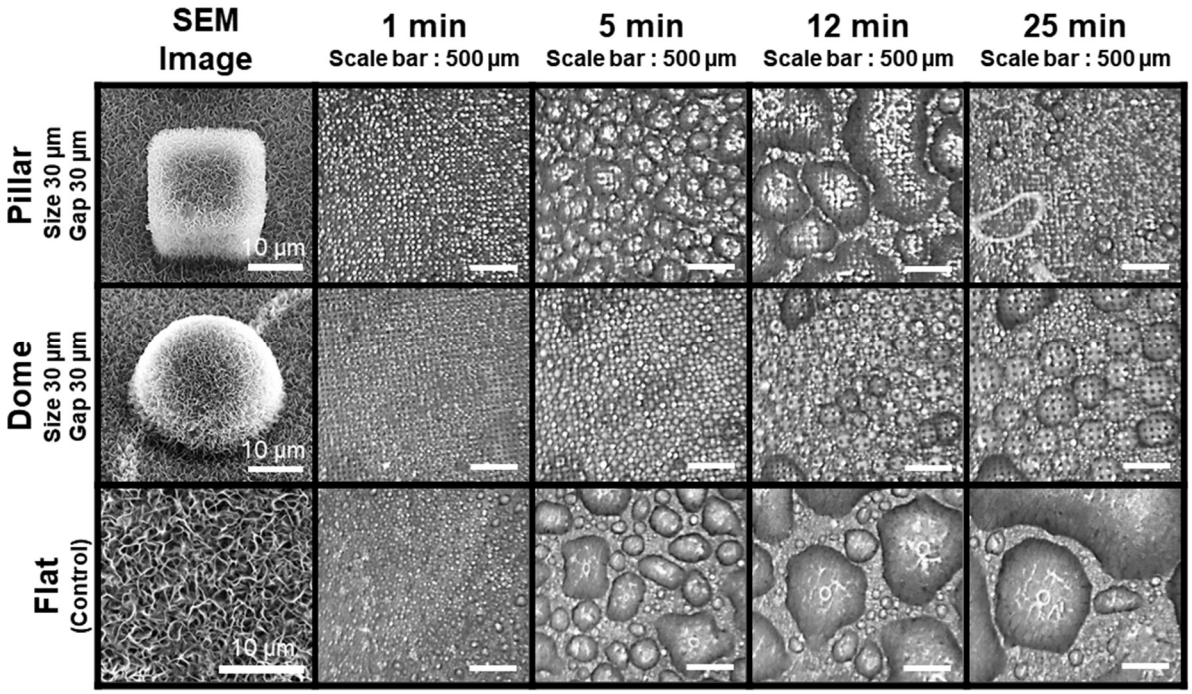

Figure 4.3. Graphical overview of chapter 4. In this chapter, we introduce condensation comparison tests of a bio-inspired surface in HVAC-simulated environment. Especially, unique bio-inspired, hierarchical, micro-dome featured surface exhibit superior dropwise condensation compared to the micro-pillars and the flat (control).

Previously, we demonstrated a nanoporous zinc oxide film that was hydrothermally grown onto aluminum surfaces and, after surface fluorosilanization, offered static contact angles up to 178°.[31] With dropwise condensation applications in mind, we demonstrated that the ability of these surfaces to support stable dropwise condensation in supersaturated damp air depended strongly on the specific growth parameters and hence the details of the surface morphology. We found that the surface with the best dropwise condensing performance was not the one with the highest static water contact angle, highlighting the importance of dedicated condensation studies.

In the previous chapter, we developed a manufacturing technique to produce hierarchical surfaces in which the zinc oxide nanostructure was grown onto arrays of square-tipped micro-pillars or micro-domes, approximating the topography of the lotus leaf.[41] Characterization of static and dynamic water contact angles showed that the addition of pillar and dome arrays both increased static contact angles and reduced contact angle hysteresis, with the smoother surfaces of the micro-domes offering the greater improvements on both fronts. While these improvements augured well for applications in droplet-shedding, condensation experiments are needed for a complete picture. In this chapter, therefore, we describe the water-condensing performance of micro-pillar and -dome arrays coated with a fluorosilanized nanoporous zinc oxide, and we identify optimal surface geometries for stable dropwise condensation. This study paves the way for the possible future application of such surfaces on air conditioning heat exchangers to promote dropwise condensation.[57]

4.2 Fabrication process, static and dynamic contact angles of the hierarchical structures

We fabricated hierarchical micro- and nano-scale surfaces using a method that we have previously developed.[41] The fabrication process flow is illustrated in Figure 4.4a. Briefly, we began by using photolithography to produce a square array of micro-scale features with a specific size and separation distance. When micro-domes were being targeted, the photoresist patterns were then heated to enable surface tension-induced reflow to take place, resulting in microstructures with curved surfaces. Two sequential elastomeric molding steps were then carried out, beginning with the photoresist-patterned wafer as a mold. The second casting step yielded a surface with the same polarity as the photoresist pattern. This cast elastomer was sputtered with an aluminum layer, onto which nanoporous zinc oxide was then grown following our previously reported procedure [31] (Figure 4.4c, 4.2d).

In this work, growth was carried out in an equimolar aqueous solution of 25 mM zinc nitrate and hexamine at 70 °C for 90 min. After rinsing in deionized water, the surfaces were then exposed to a vapor of 1H,1H,2H,2H-perfluorooctyltrichlorosilane in a vacuum bell-jar for 40 minutes to render them hydrophobic. The surfaces studied in this work all had a feature size (i.e. pillar width or dome diameter) of 30 μm, and different cases were explored with gap-to-feature-size ratios of 0.5, 1, 1.5, and 2 (Figure 4.4b). These geometries are reminiscent of many natural leaf surfaces, including that of the lotus. A 'flat' surface without microstructures but with the fluorosilanized zinc oxide film was also studied for reference.

The behavior of water droplets placed directly onto the surface of interest—rather than condensed from vapor onto the surface—provides a simple and convenient characterization method. We measured the static, advancing, and receding contact angles of 7.5 μL water droplets on all the surfaces studied, using a custom-built goniometer with a tilting stage and the method detailed in our previous work.[31] Briefly, side-views of the droplets resting on the surfaces were captured using a Thorlabs DCC1645C CMOS image sensor coupled to a 4× objective and a 30 mm focal-length achromatic doublet. Sessile (static) contact angles were extracted from images captured with the stage held horizontal, using ImageJ[58] and its low bond axisymmetric drop shape analysis plugin[44]. Advancing and receding angles were determined from the video frame that was captured immediately before the droplet began sliding in the advancing direction as the stage was gradually tilted. To extract these dynamic contact angles, the Dropsnake B-spline active contours plugin was used[45]. Contact angle hysteresis is defined as the difference between advancing and receding contact angles.

We have previously investigated the dependence of static and dynamic water contact angles on the feature size and size-to-gap ratios of dome and pillar arrays coated with the nanoporous ZnO film[41]. Here we recapitulate droplet behavior on arrays with feature sizes of 30 μm, to facilitate comparison with the new condensation results.

All these surfaces were found to be superhydrophobic (Figure 4.4e). The dome-shaped structures had higher average static contact angles than the rectangular pillars by approximately 6° for each size-to-gap ratio tested, and the dome arrays offered lower contact angle hysteresis than the corresponding pillar features (Figure 4.4f). Therefore, the smoother dome arrays were clearly superior to the sharp-edged square pillar arrays in terms of their ability to repel and shed externally introduced droplets. Nevertheless, both the dome and pillar arrays showed higher static contact angles and lower hysteresis than the 'flat' (nanostructure-only) reference case.

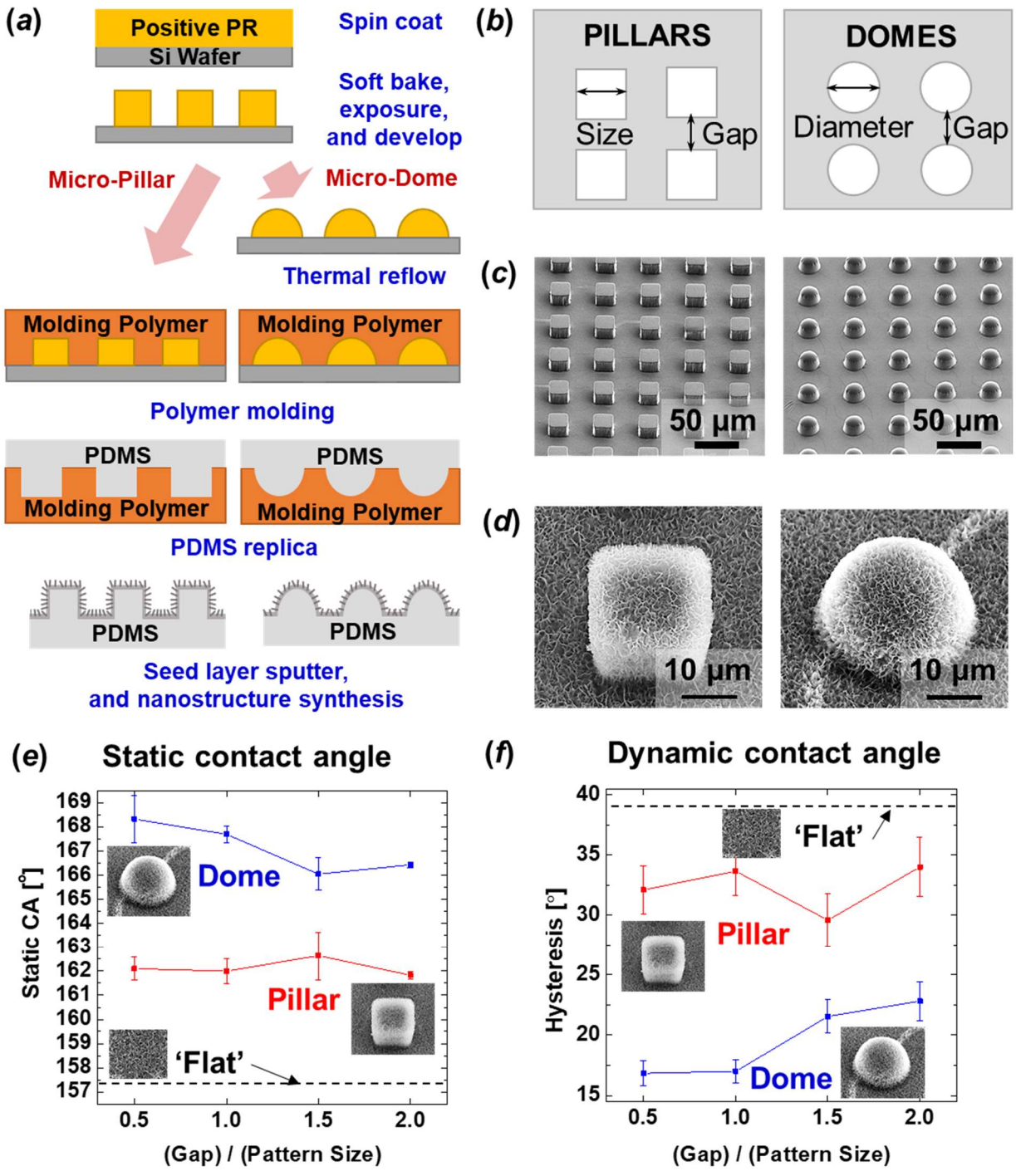

Figure 4.4. Fabrication process of the hierarchical structures and summary of characterization of the surfaces' response to externally introduced water droplets. Adapted from the previous chapter.[41] (a) Schematic of fabrication process for arrays of domes and square pillars. (b) Definition of feature size/diameter and gap. (c) Scanning electron microscope (SEM) images

showing a micro-pillar array with pattern sizes and gap both equal to 30 μm (left); a micro-dome array with the diameter and gap both of 30 μm (right). (d) SEM images of a representative square pillar (left) and dome (right), showing the nanoscale porosity of the synthesized ZnO film on the microstructures. (e) Water sessile contact angles on arrays of square pillars and micro-domes, both covered with a fluorosilanized ZnO nanoporous coating. Contact angles are plotted against varying gap-to-pattern-size ratios. Pattern size is a constant 30 μm. (f) Contact angle hysteresis plot for the same sets of square pillar and micro-dome arrays. In (e) and (f), 'Flat' denotes the contact angle or hysteresis respectively on a surface with the fluorosilanized ZnO coating but no microfeatures. Error bars represent ±1 standard error of the mean; five droplets per specimen.

	Experimental Water Sessile Contact Angle (Average)			
Pattern Type	**Gap/Pattern size 0.5**	**Gap/Pattern size 1.0**	**Gap/Pattern size 1.5**	**Gap/Pattern size 2.0**
Pillar	162.1040	161.9942	162.6402	161.8244
Dome	168.3318	167.6994	166.0472	166.4322

Table 4.1. Result comparison of water sessile contact angle on the micro-pillar, micro-dome, and the 'flat' surface.

	Experimental Contact Angle Hysteresis (Average)			
Pattern Type	**Gap/Pattern size 0.5**	**Gap/Pattern size 1.0**	**Gap/Pattern size 1.5**	**Gap/Pattern size 2.0**
Pillar	32.1040	33.6656	29.5944	34.0144
Dome	16.8458	16.9992	21.5480	22.8240

Table 4.2. Result comparison of contact angle hysteresis on the micro-pillar, micro-dome, and the 'flat' surface.

These observations may be explained by a Cassie–Baxter-like composite wetting mode in which the droplets make contact only with the tips of the microstructures and therefore have a lower liquid–solid contact area than the surface bearing only the ZnO film. We attributed the superior performance of the domes compared to the square pillars to the fact that it was possible for only a small region at the tips of the micro-domes to be in contact with water, resulting in extremely low contact area fractions. On the other hand, it can be expected that the entirety of the flat top surfaces of the square pillars would be in contact with any droplet resting above them. Moreover, the absence of sharp edges from the micro-dome arrays is expected to have reduced the likelihood of droplet pinning and can explain the lower contact angle hysteresis observed.

As the gap-to-size ratio of the dome patterns increased from 0.5 to 2.0, however, the hysteresis increased by about 5°, which we attribute to an increased likelihood of the droplet penetrating into the region between domes, leading to possible capillary bridge formation between the water and the flat portion of the structure, and hence higher liquid–solid adhesion. [57,59]

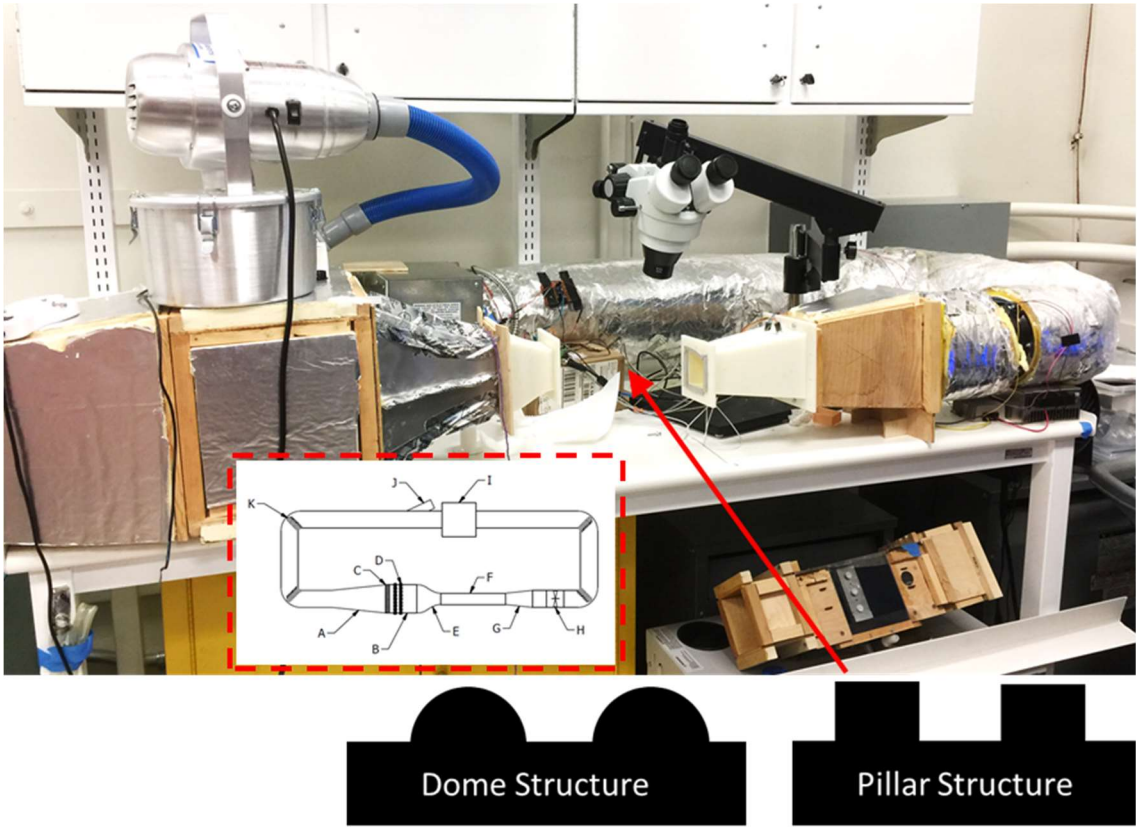

Figure 4.5. Our condensation experiment setup – "Wind Tunnel". The condition of testing used were 60–80% relative humidity, generated by an upstream water nebulizer, dry bulb temperature

of 26–30 °C achieved with a duct heater, and air flow of 2–3 m/s. Samples were placed on an aluminum holder that was back-cooled with 4 °C chilled water, and the sample surfaces were oriented vertically, such that air flowed horizontally across the sample surface while gravity tended to pull condensed droplets down across the sample surface.

4.3 Condensation performance results of square pillar and micro-dome with various pattern-gap ratios

Experiments were also performed to observe the performance of the surfaces under condensing conditions, by simulating exposure to incoming humid air. As shown in Figure 4.5, a custom-designed and -built, closed-loop wind tunnel was used, as described in previous work[31]. The testing conditions used were 60–80% relative humidity, generated by an upstream water nebulizer, dry bulb temperature of 26–30 °C achieved with a duct heater, and air flow of 2–3 m/s.

Samples were placed on an aluminum holder that was back-cooled with 4 °C chilled water, and the sample surfaces were oriented vertically, such that air flowed horizontally across the sample surface while gravity tended to pull condensed droplets down across the sample surface. For each sample tested, the setup was allowed to stabilize in static air at room conditions (approximately 20 °C and 40 % RH) before air speed and the elevated temperature and humidity were introduced. A video was captured for approximately 30 minutes, directly facing a portion of the surface so that droplet growth, coalescence, and any surface flooding could be observed. The same DCC1645C image sensor was used as for the contact angle measurements, but in this case was connected to an Amscope SM zoom trinocular stereomicroscope with a 4.5× objective and an LED ring light mounted around the objective.

Figure 4.6 (Microscopic view with scale bars of 500 μm) and Figure 4.8 (Macroscopic view with scale bars of 2 mm) shows that while all the tested surfaces enabled dropwise condensation during the first few minutes of operation, after 25 minutes only the 30 μm micro-domes spaced by 30 μm (the “30:30” surface) still showed clearly defined, spherical cap-like droplets. Condensed water on all the other surfaces—including the ‘flat’, nanostructure-only surface—had formed irregular pools of water that were up to several mm in diameter and had effectively flooded the surfaces. The unique performance of the 30:30 micro-dome surface was found to be repeatable in an independent condensation experiment (Figure 4.7).

(*a*) Square pillars with varying pattern size-to-gap ratio (unit: μm)

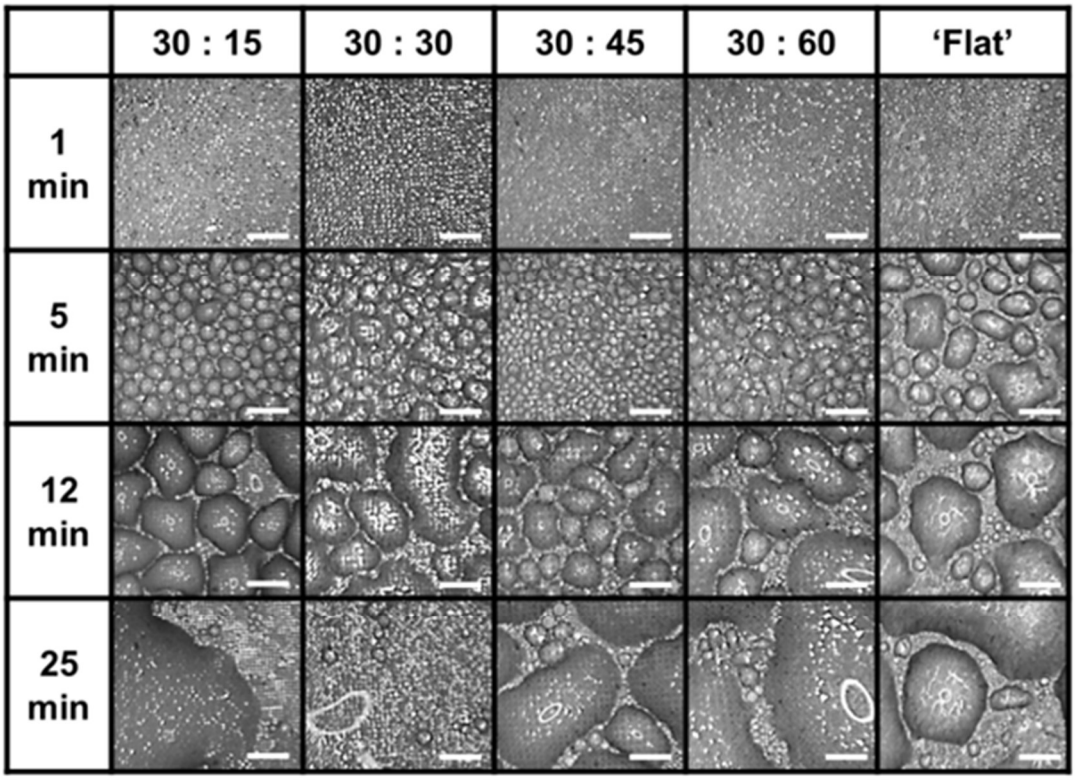

(*b*) Micro-domes with varying diameter-to-gap ratio (unit: μm)

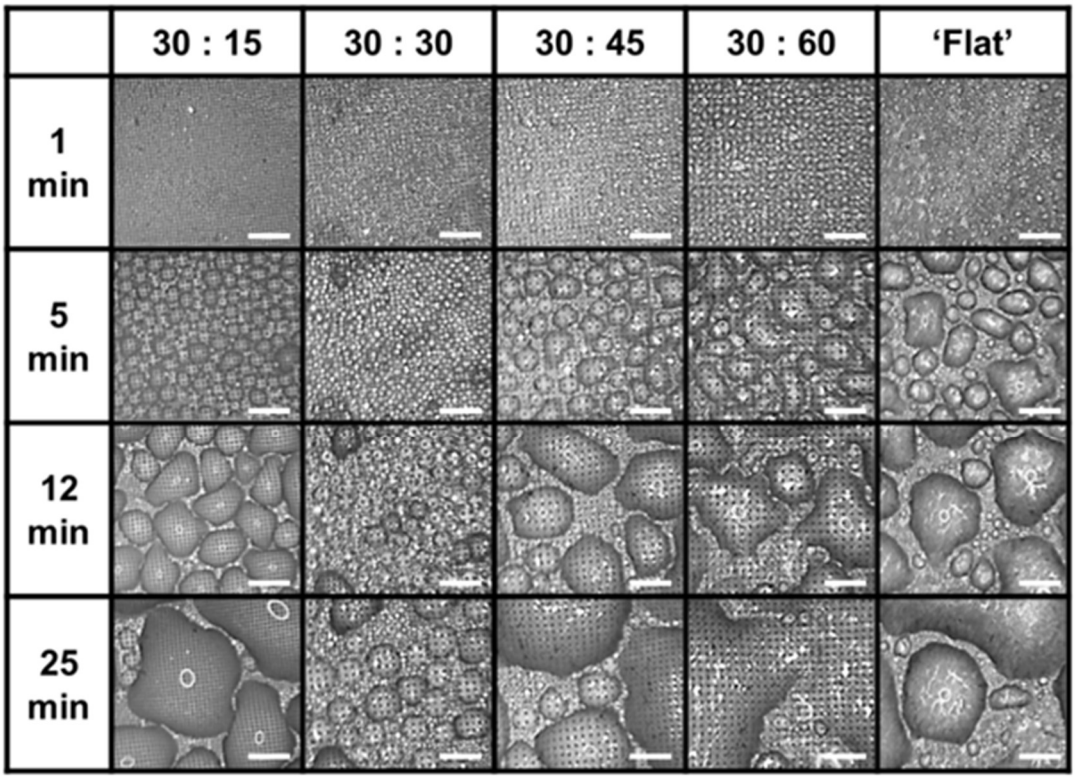

Figure 4.6. Condensation performance results of square pillar and micro-dome with various pattern-gap ratios. Recorded video length was 30 min. 'Flat' denotes a surface with the fluorosilanized nanostructured film only, and no microstructures. Scale bars: 500 μm.

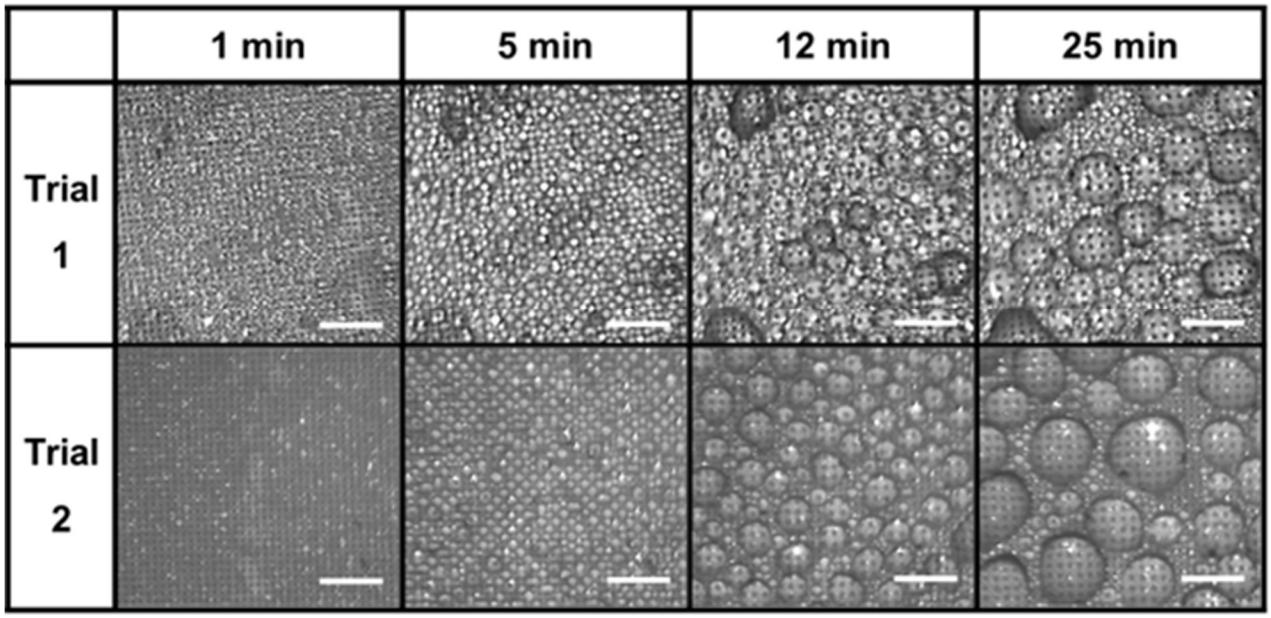

Figure 4.7. Repeated condensation performance on micro-dome arrays with 30:30 diameter–gap ratio. Scale bars: 500 μm.

It is perhaps surprising that the 30:30 domes would behave in this way while the more tightly-packed 30:15 domes showed just as much flooding as the even sparser 30:45 or 30:60 patterns. Our analysis of the static contact angle and hysteresis results in Chapter 4-2 suggested the 30:15 and 30:30 dome arrays yielded comparable hysteresis and static contact angles, so this aspect of condensing performance is not well predicted by static droplet behavior. A possible insight comes from closer inspection of the condensation images after 1 minute (Figure 4.6 and Figure 4.9): the incipient droplets appear to have formed between domes, rather than on top of them. This effect is particularly clear in the 1-minute image of the 30:45 micro-domes.

It is not yet clear why droplets would preferentially nucleate between domes. Since the surfaces were vertically oriented, gravity would not have been consistently directing droplets into the interstices between domes. It is possible that the topography of the surface shielded the interstices from the flow of hot, humid air and allowed the temperature of the air between the domes to fall to a lower value than that at the tips, promoting earlier condensation between domes.

It is also plausible that coalescence events between droplets in the interstices can take place more easily when the gaps between the micro-domes exceed some minimal value, and that droplets can then more easily escape the interstices to sit on the tips of the domes and later be shed.[57]

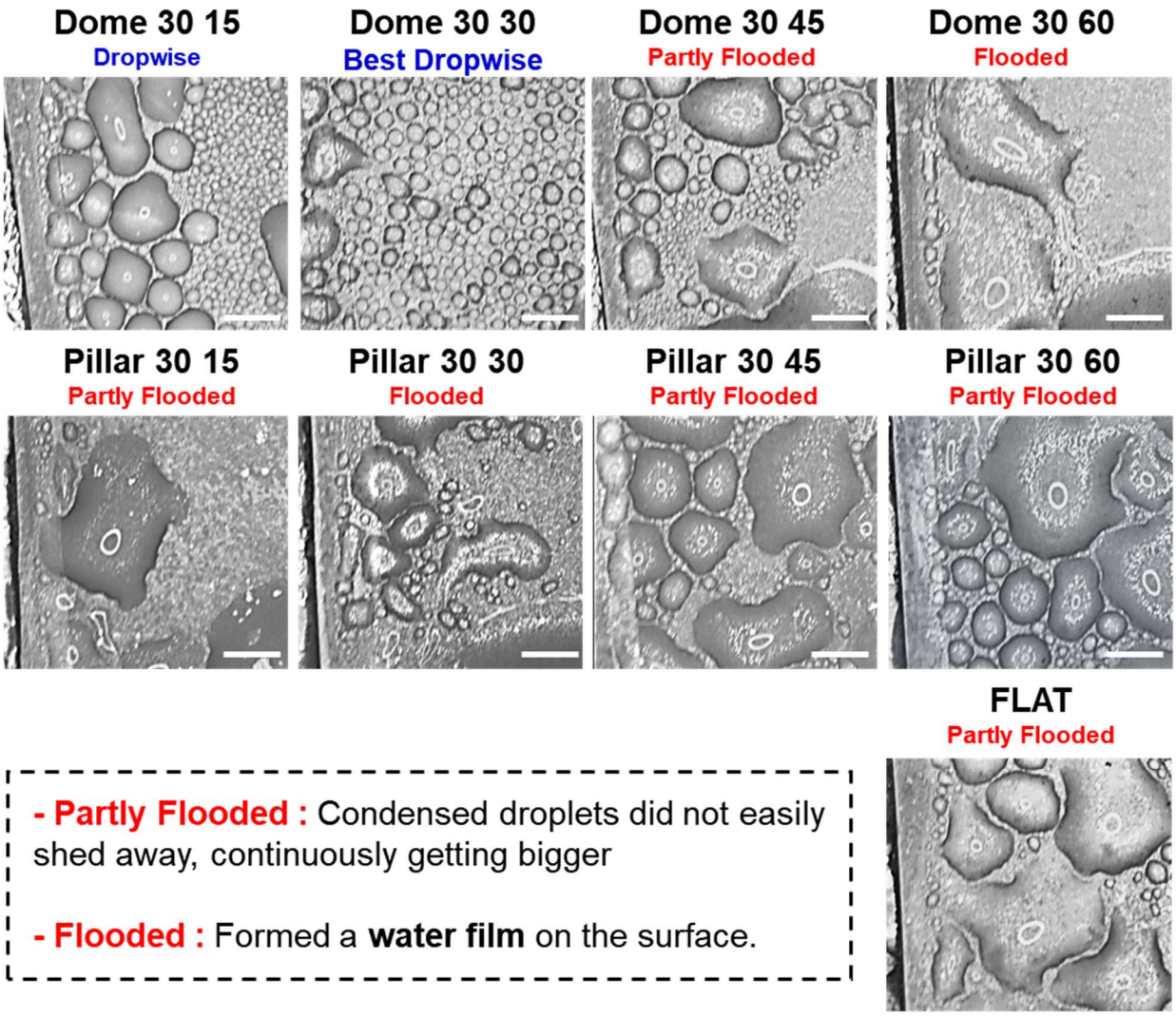

Figure 4.8. Macroscopic view comparison of condensation performance (after 30-minute) of square pillar and micro-dome with various pattern-gap ratios. 'Flat' denotes a surface with the fluorosilanized nanostructured film only, and no microstructures. Scale bars: 2 mm.

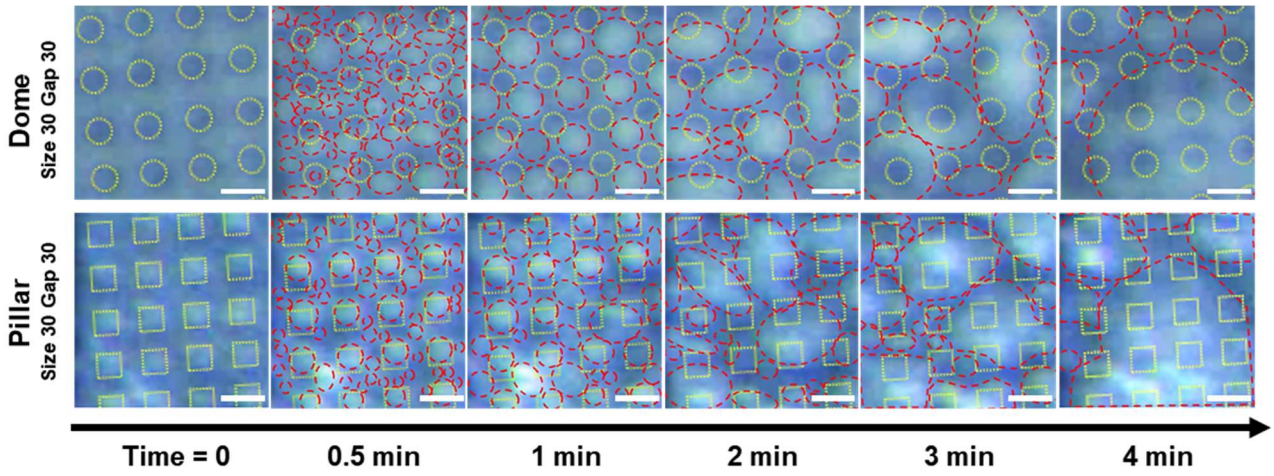

Figure 4.9. Early phase condensed droplets merging events (time ≤ 5 min) of square pillar array and micro-dome array. Both patterns have equal size and spacing of 30 µm. At early phase, the result showed differences between water droplet nucleation and merging. Yellow lines are surface patterns while red lines are condensed droplets. Scale bars: 50 µm

4.4 Image analysis – Quantification of condensate area fraction

In order to evaluate further the dropwise condensation behavior of the 30:30 dome array compared to the pillar equivalent and a purely nanostructured surface, the video recordings of condensation were analyzed to extract water droplet size distributions on the surfaces, as well as the evolution of condensate area fraction (CAF) over time. CAF is defined as the fraction of the projected area of the sample surface that is covered by detectable water droplets. For each time-point analyzed, the corresponding frame from the video was first converted into grayscale form by adding together the values of the three color channels for each pixel. The individual droplets were then detected, by making use of the fact that light reflection from the droplets resulted in a bright zone within each droplet and a darker shadow region all around the droplet.

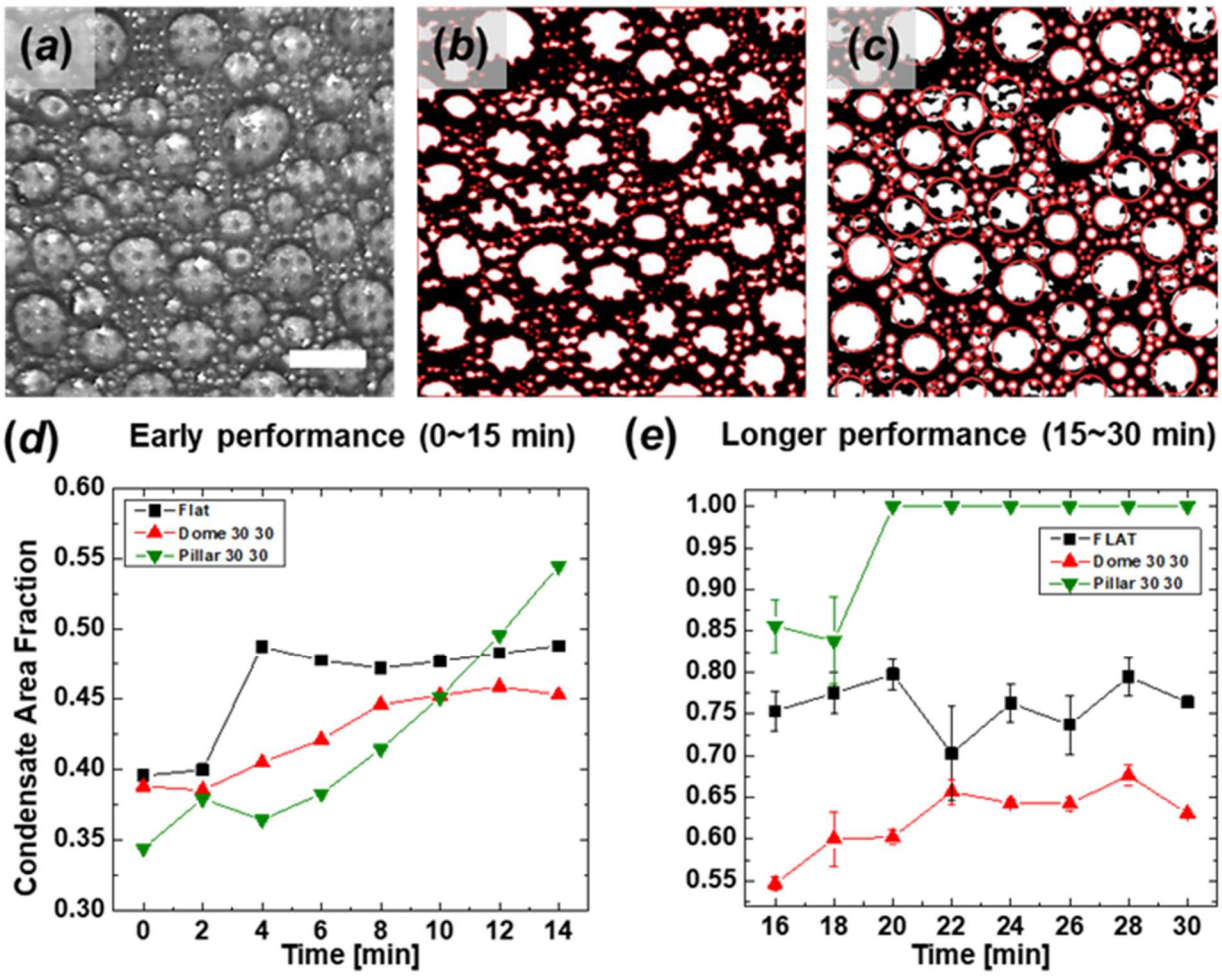

Figure 4.10. (a) Condensation performance of a 30:30 diameter-to-gap ratio micro-dome array: image was captured after eight minutes of testing. (Scale bar 500 µm; sample thickness ≈ 1.8 mm; saturation values (S) = 1.2–1.3; air temperature ≈ 35 °C; surface temperature ≈ 16.5 °C; RH ≈ 40.6 %; air velocity ≈ 3 m/s.) (b) Droplet boundary detection of the processed droplet image to indicate separation of droplet occurrences from the image background. (c) The previous image overlayed with circles from a region-detection routine that extracted the approximate radius and projected area of each detected droplet in an image. (d) Condensate area fraction (CAF) extracted by the software routine, for 0–14 min from the beginning of condensation testing. Results are shown for 30:30 micro-dome and micro-pillar arrays, and the 'flat' surface with the nanoporous film only. CAF=1 means the surface is totally covered by water. (e) CAF estimated by human analysis of captured images for 16–30 min after the beginning of condensation testing.

The detection algorithm used Matlab's built-in command, graythresh, applying Otsu's method to determine a threshold intensity value that 'minimizes the intraclass variance of the thresholded black and white pixels'.[60] This threshold value was then used to convert the image to binary form, with the white pixels notionally corresponding to

droplet regions. In some larger droplets, microfeatures beneath the droplet manifested themselves as dark spots, and a 'hole fill-in' command was used to subsume these spots into the droplet area (Figure 4.10b). This image was fed into a watershed segmentation algorithm that explicitly distinguished between droplet and non-droplet regions.[61] The centroid position of each 'droplet' region was then calculated, and the radius of a circle with an area equal to that of the droplet region was calculated. These circles were then superimposed on the image to provide a visual check of the algorithm's operation (Figure 4.10c).

The CAF was computed as the sum of the areas of these circles divided by the total area of the imaged region. It should be emphasized that because the contact angle between the condensed water and the surface cannot be directly observed from these aerial images, the fitted circles approximate the projected area of the droplets on the surface. They may therefore not exactly represent the contact area fraction, but nevertheless provide a useful metric for comparing the performance of different surfaces.

In cases where droplets became particularly large and irregular in shape, they could not adequately be approximated by circular regions via the above algorithm. In these cases, a manual technique was used to gauge CAF. The perimeters of the wetted regions were traced out in a Matlab figure, and the enclosed areas were computed. CAF was then estimated as the ratio of the sum of enclosed areas to the total imaged area. This analysis was performed three times for each image, to quantify any variability introduced by human visual judgement.

The CAF plot in Figure 4.10d showed that during approximately the first ten minutes of condensation, the 30:30 domes, 30:30 pillars, and purely nanostructured samples all had similar CAF values, within about 0.1 of each other. This observation is supported by images in Figure 4.6. After about 10 minutes, however, the CAF of the square-pillared surface grew rapidly and approached a flooded state. From 16 minutes onwards, the manual CAF determination method was used because of the irregular shapes of many of the droplets (Figure 4.10e); the comparison continues to show the micro-dome array yielding consistently lower CAF values than either the micro-pillar array or the nanostructure-only surface. The CAF of the domed surface remained stable, at around 0.65, up to the end of the condensation experiment at 30 minutes, while the pillared surface had completely flooded.

Although the CAF values recorded on the nanostructure-only surface were around 0.75 by the end of the 30-minute period—just 0.1 higher than those of the micro-domed

surface—the morphology of the condensed water was profoundly different. On the nanostructure-only surface, the droplets were large and irregular in shape, whereas on the micro-dome array, they retained the shapes of spherical caps. Interpretation of condensing performance therefore needs to take account not only of CAF but also of the appearance of the images themselves. The temporal fluctuations of CAF of both the micro-dome arrays and the nanostructure-only surfaces are attributable to the motion of droplets out of the camera's field of view, and their subsequent replacement by new condensate.[57]

4.5 Additional testing for optimization – Additional testing for surface optimization – Condensation performance testing of ZnO nanoporous structure with various synthesis parameters, and fluorosilane treatment by spray method

The final challenge addressed in this chapter is to investigate the possibility of scaling up the ZnO synthesis process to enable performance testing of the material on an industrial-sized cooling coil (Figure 4.11). Our team's first goal was to study the influence of ZnO nanoporous structure synthesis parameters to achieve the best possible condensation performance.

The important growth parameters for our ZnO nanoporous structure are synthesis temperature, solution molar concentration, and synthesis time. The ZnO nanoporous structures grown with various parameters looked surprisingly different. Especially, as the synthesis time increases and the bath temperature increases, the ZnO nanostructures became more dense resulting in a smaller pore sizes (Figure 4.12). There was a clear trend observed in the case of 50 °C and 60 °C that the larger porous structures were grown with the longer synthesis time and the smaller solution concentration. However, the synthesis temperature of 70 °C showed more dense structures for all the other experimental parameters (times and concentrations). We believe this result can be attributed to the solution having a faster reaction (or synthesis) rate at higher temperatures, thus, generating a thicker and denser layer of nanostructures.

We then used the wind tunnel described above to test the condensing performance of all the structures grown. Testing conditions were 60–80% relative humidity, dry bulb temperature of 26–30 °C, and air flow of 2–3 m/s. The nanostructure with synthesis parameters of 70 °C, 25 mM and 4.5 hours was the only one that showed stable dropwise condensation performance, in which droplets were continuously shed out, and thus, fresh cold surface was continuously made. Most of the other samples were fully flooded after considerably shorter testing periods.

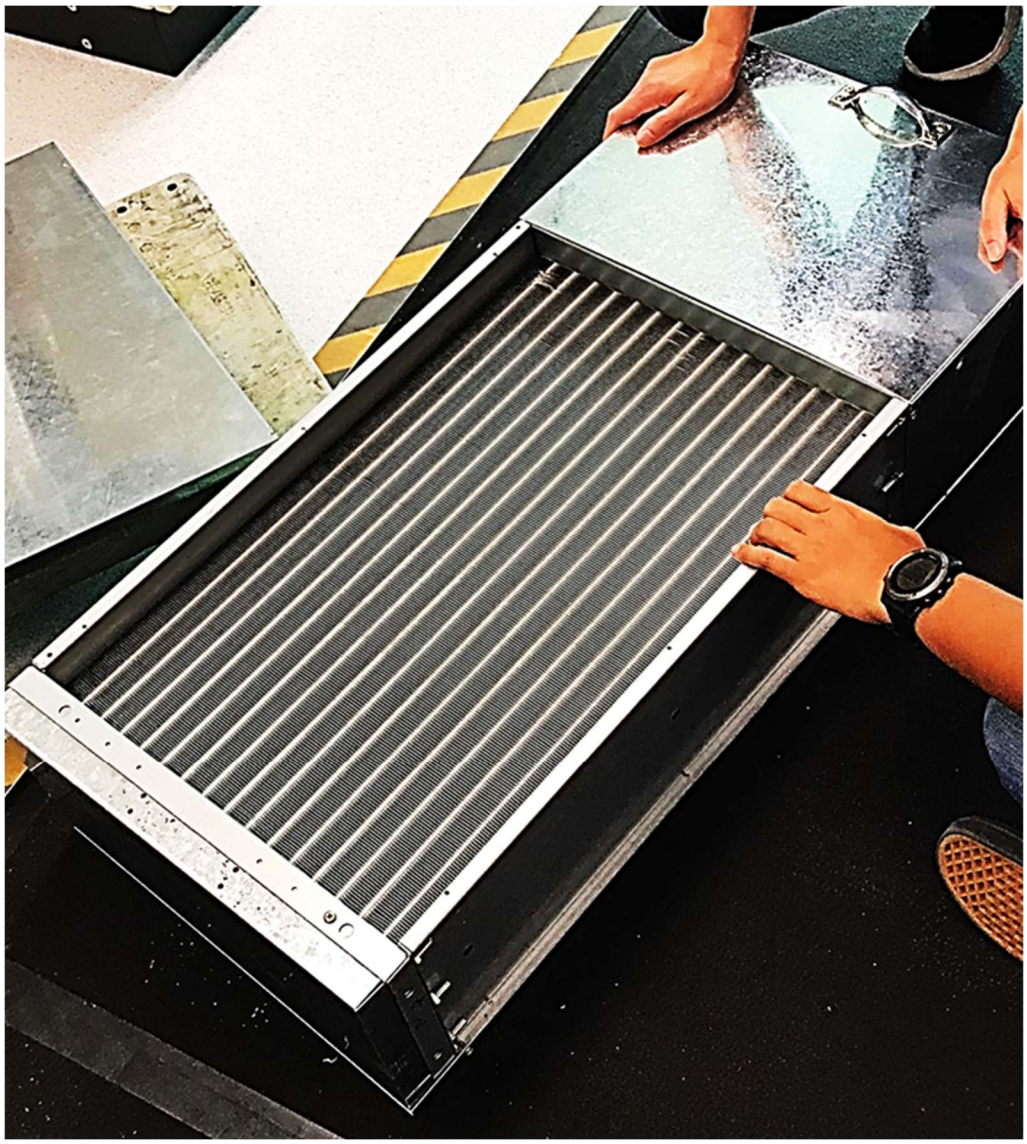

Figure 4.11. A photo of actual air conditioner evaporator coil object, which consists of hundreds of thin aluminum fins. (Photo courtesy: Kristyn Kadala)

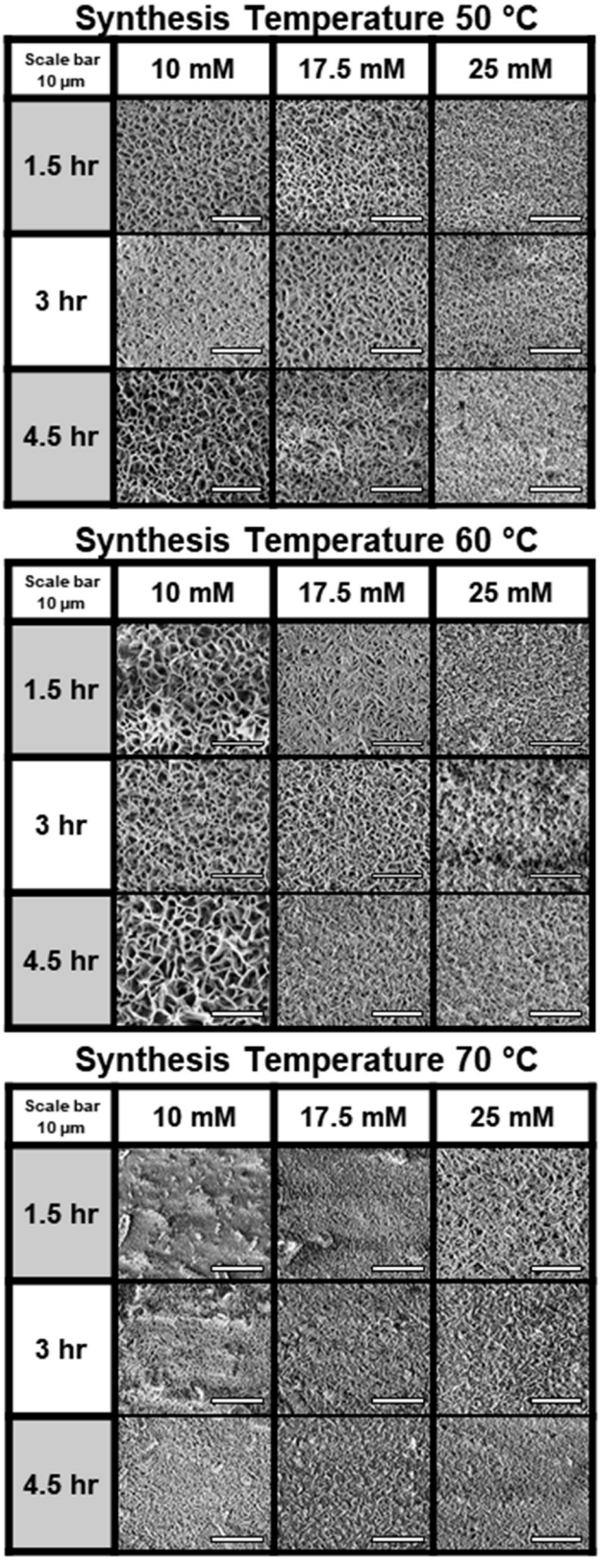
Synthesis Temperature 50 °C
Scale bar 10 µm
10 mM
17.5 mM
25 mM
1.5 hr
3 hr
4.5 hr
Synthesis Temperature 60 °C
Scale bar 10 µm
10 mM
17.5 mM
25 mM
1.5 hr
3 hr
4.5 hr
Synthesis Temperature 70 °C
Scale bar 10 µm
10 mM
17.5 mM
25 mM
1.5 hr
3 hr
4.5 hr

Figure 4.12. Scanning electron microscope images of our ZnO nanoporous structures with various growth parameters: synthesis temperatures (50, 60, 70 °C), solution molar concentrations (10, 17.5, 25 mM), and synthesis times (1.5, 3, 4.5 hours).

In addition to the growth parameter studies, we developed and optimized a stable spray-based fluorosilanization process. For the solution to be sprayed, 1g of 1H,1H,2H,2H-Perfluorooctyl-triethoxysilane (POTS, Sigma Aldrich) was mixed into 49 g of pure ethanol (Decon Labs, Inc) and the solution was stirred thoroughly for 10 min.[62] The samples' surfaces were sprayed with the POTS solution from a water sprayer (Ace hardware) and were dried at room temperature for 30 min. These spraying and drying steps were repeated up to four times. Finally, the samples were rinsed with pure ethanol and allowed to 'cure' at room temperature in a fumehood for 24 hours.

Static contact angles were measured on ZnO nanoporous structures that had been synthesized on aluminum finstock and then treated with between zero and four spraying and drying cycles as described above (Figure 4.13). The surfaces treated with three and four spray cycles were observed to offer stable superhydrophobicity (with the contact angle of approximately ~155°). This spraying method of fluorosilanization enabled a minimal amount of chemical (e.g. POTS) to be used, compared to more conventional complete immersion in a bath of POTS solution. The ethanol solvent has low surface tension and thus spreads easily across the target surface when applied, with remarkable results. The method also enabled a large industrial cooling coil to be fluorosilanized, which would not have fit into any readily available vacuum chamber for vapor-phase silanization — another conventional coating method. We therefore believe that our optimized spray fluorosilanization method is a perfect candidate for the hydrophobic surface termination of tightly-packed aluminum fins and large cooling coils.

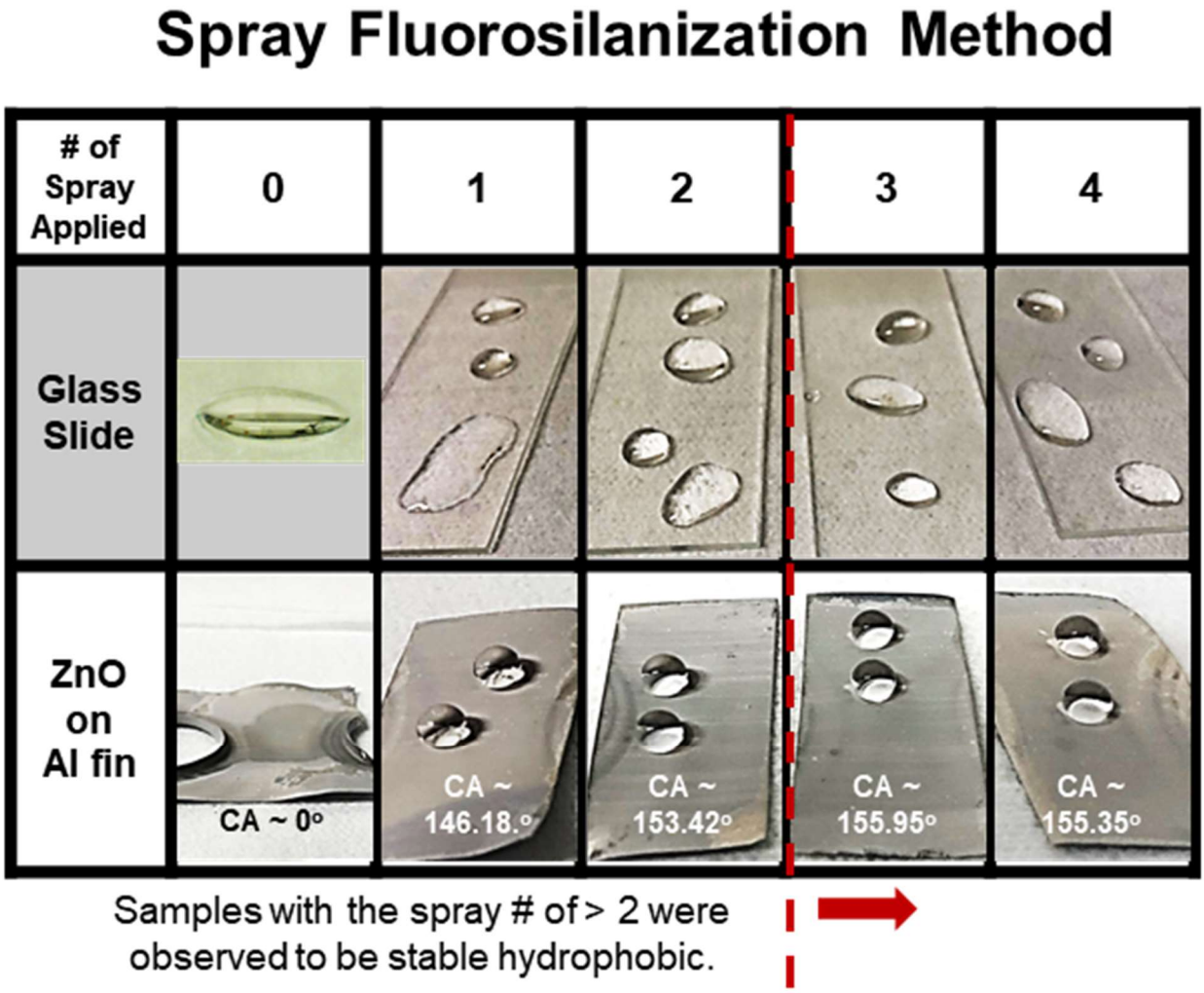

Figure 4.13. Spray fluorosilanization method. Glass substrate and ZnO nanoporous structure grown aluminum substrate were tested.

As the last goal of this project within our team, the ZnO growth parameters yielding the best condensation performance and the optimized spraying method of fluorosilane treatment, as described above, were applied to two full-scale cooling coils (Figure 4.14). As shown in Figure 4.14, the process appears to have been successful. The ZnO nanoporous structure synthesis on the tightly packed aluminum fins was apparently highly uniform and exhibited superhydrophobic behavior in response to a water spray after processing was complete. These coils have now (December 2019) been shipped to our collaborators at the Singapore–Berkeley Building Efficiency and Sustainability in the Tropics (SinBerBEST) center in Singapore, where their performance will be tested in an air-conditioning system, and compared with the performance of an uncoated coil with the same fin geometry.

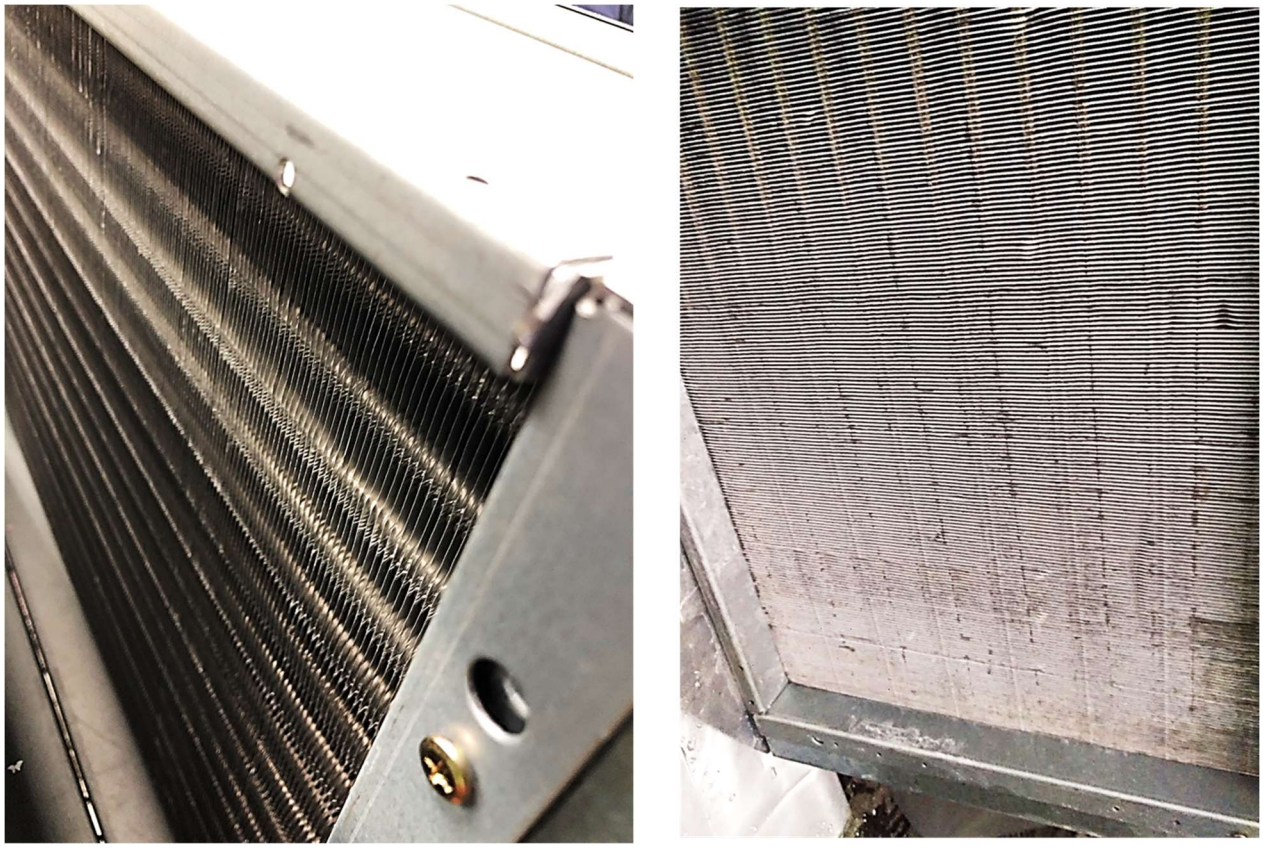

Figure 4.14. Photos of before (left) and after (right) our process on a full-scale cooling coil inside an air conditioner evaporator module. (Photo courtesy: Kristyn Kadala)

4.6 Conclusion

In this chapter, we have demonstrated an experimental framework for evaluating the dropwise condensation performance of hierarchically structured surfaces in highly supersaturated moist air, and have used it to establish the favorable performance of structures composed of micro-dome arrays coated with a nanoporous, fluorosilanized ZnO film. Our specific findings are:

- Of the surfaces tested, the most stable dropwise condensation was obtained on surfaces composed of an array of 30 μm-diameter domes separated by 30 μm, with the fluorosilanized ZnO film applied conformally.

- Surfaces with square-tipped pillars of comparable size and spacing performed much less favorably, and flooded within about 10 minutes of condensation testing.

- Surfaces that were coated only with a fluorosilanized ZnO coating (no microstructures) also exhibited flooding under comparable conditions.

- Micro-dome arrays with larger or smaller spacings than the optimal 30 μm did not exhibit as favorable condensing performance, suggesting that droplet growth and coalescence dynamics in the interstices between domes as well as on top of them are important in determining surface performance.

These findings can provide useful guidance in the development of manufacturable surfaces for condensation heat transfer, including in air conditioning systems. For the benefits of hierarchically structured surfaces to be realized at an industrial scale, however, methods need to be developed to impart the micro-domes at reasonable cost to heat exchanger materials such as aluminum alloy. Macroscopic industrial processes such as knurling, or coining could potentially be adapted for this purpose.

In addition, in Section 4.5, we established a set of ZnO growth conditions and a spray-based fluorosilanization process that could be readily scaled for application to commercial heat exchangers. The creation of large arrays of microstructures with controlled shape remains the next unmet challenge. Furthermore, it would be valuable to carry out further experimentation to quantify the condensation heat transfer coefficients of these surface designs and to correlate such measurements with the observed droplet growth and coalescence dynamics.[57]

Chapter 5. Adding Multiple Levels of Hierarchy for More Robust Water Repellency

5.1 Introduction and motivation

Superhydrophobic surface technology has attracted huge recent interest because of its many potential applications in, e.g., self-cleaning, condensation acceleration, anti-corrosion, anti-biofouling, and drag reduction. In particular, engineering bio-inspired surfaces, such as *Nelumbo nucifera* (lotus leaf), and *Colocasia esculenta* (taro leaf), has been extensively studied to achieve its excellent superhydrophobic and low water adhesive characteristics[62]. *Nelumbo nucifera* (lotus leaf) is a semi-aquatic plant and develops wide leaves up to 30 cm in diameter with exceptional water repellency[2]. In order to adapt to the aquatic environment, the upper epidermis features distinctive hierarchical structures consisting of papillae with a dense coating of agglomerated wax tubules and periodic undulating boundaries between epidermal cells, which acts as the basis for the well-known superhydrophobicity (or lotus effect).

In general, based on the widely known Cassie–Baxter relation describing the effect of a reduced solid–liquid contact interface[3], previous studies have attempted to achieve hierarchical surfaces with micro- or nano-texturing to reduce the contact area fraction, improve the robustness of the superhydrophobicity[4–10], and thus lower the force needed to shed water droplets from the surface by, e.g., gravity or air flow. However, because most existing technologies with lithographic or molding techniques typically combined one, or occasionally two, length-scales of roughness, they have not been successful enough to mimic the actual complex geometries of biological epidermis (e.g. lotus and taro leaf structures), which have periodic micro-grooves defined by boundaries between epidermal cells with contain papillae of varying height and nanosized short wax tubules[2].

Therefore, in this chapter, in order to see the effect of increasing levels of surface complexity, we introduce a novel triple hierarchical superhydrophobic surface (TriSS), inspired by water-repellent lotus leaf structures which consist of an array of various sized micro-protrusions with nano-scale hairy structures and grooves between the protrusions.

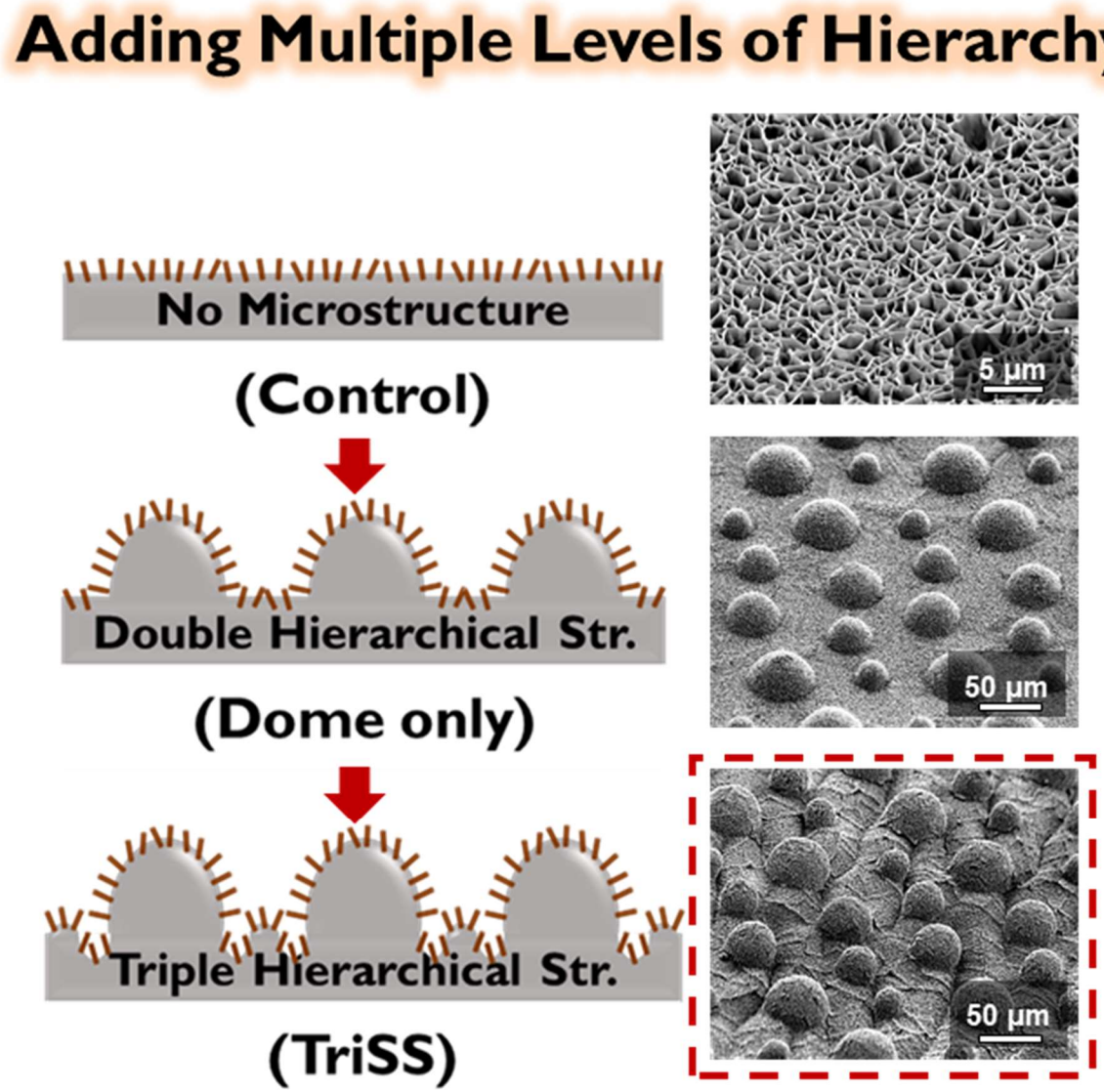

Figure 5.1. Overview Schematics of Chapter 5. This Chapter introduces a novel triple hierarchical superhydrophobic surface (TriSS), inspired by water-repellent lotus leaf structures which consist of an array of various sized micro-protrusions with nano-scale hairy structures and grooves between the protrusions. Our process allows the surface with the distinctive artificial three-tier hierarchical structures with its precisely tuned surface morphology with the highest resemblance to the actual lotus leaf: array of micro-dome various sizes and heights via a standard single layer photolithography followed by reflow, polymer bi-layer deformation maximized by presence of multiple sized surface microstructures, and conformal growth of zinc oxide nanostructure.

According to previous studies[63,64], when a surface has hierarchical structures that incorporate nanoscale features, the Laplace pressure offering resistance to water infiltration

is expected to increase while the liquid–solid contact area is reduced, relative to a surface with less complexity or fewer nanoscale features. Laplace pressure is defined as follows:

$$\Delta P_{Laplace} = P_{Liq} - P_{Air} = \frac{2\,\gamma\,cos\theta}{r}\text{[65]} \quad (5.1)$$

where ΔP is a difference between pressure of liquid, P_{Liq}, and pressure of air P_{Air}, γ is surface tension of the liquid, r is radius of capillary (corresponding to the relevant feature size on the surface), and θ is a contact angle of the liquid. Therefore, from the equation (5.1), when $\theta < 90°$ (surface is hydrophilic), P_{Liq} is larger so that the water is sucked in. On the other hand, when $\theta > 90°$ (surface is hydrophobic), P_{Air} is larger so that the water is pushed out. In the pursuit of superhydrophobic characteristics, the latter case of larger pressure from the air is desirable since the water needs to be repelled from the surface.

The force repelling water from the superhydrophobic surface can then be approximated as follows:

$$(Force\ of\ water\ resisting) = \left(-\Delta P_{Laplace}\right) \times (Liquid - Air\ Contact\ Area) \quad (5.2)$$

From equation (5.2), in order to repel water effectively, we can pursue two strategies. First, we can increase the first term on the right side, $\left(-\Delta P_{Laplace}\right)$, which can be achieved by reducing the radius of capillary (corresponding to surface roughness in hierarchical structures) and/or by increasing the contact angle. The second strategy is to increase the second term $(Liquid - Air\ Contact\ Area)$, in other words, to decrease the $(Liquid - Solid\ Contact\ Area)$, which can be achieved by higher surface roughness. Having additional levels of structural hierarchy can effectively satisfy both strategies at the same time, and thus, it becomes the most effective way of repelling water from the surface.

Table 5-1 shows a scale-by-scale comparison between the surface of *Nelumbo nucifera* and our triple hierarchical superhydrophobic surface (TriSS). *Nelumbo nucifera* has a remarkable hierarchical structural configuration consisting of micro-papillae with a dense coating of agglomerated nano-sized wax crystals and periodic micro-grooves between epidermal cells. In this study, we precisely engineered a surface with a distinctive artificial three-tier hierarchical structure whose precisely tuned surface morphology bears a close resemblance to the actual lotus leaf. The engineered surface consists of an array of micro-domes of various sizes and heights, produced by standard single-layer

photolithography followed by thermal reflow. These microstructures are transferred, by casting, to elastomeric target surfaces, which are then augmented with complex additional surface wrinkles by the relaxation of biaxial stress in an oxidized surface layer of the elastomer. The presence of a variety of sizes of surface microstructures directs the formation of the wrinkles. The process is completed with the conformal growth of a zinc oxide nanoporous film and fluorosilanization to add further surface complexity.

	Lotus Leaf (*Nelumbo nucifera*)	**TriSS**
Micro-Protrusion	Micropapillae (with Various Tip Radii)	Micro-Dome (Various sizes and heights)
Micro-Grooves	Boudaries between Epidermal Cells	Polymer Bi-layer Buckling
Nano-Structure	Nanosize Wax Crystal	ZnO Nanostructure
Chemical Coating	Epicuticular Wax (Nonacosanediols)	Fluoro-Silane (1H,1H,2H,2H-Perfluorooctyltriethoxysilane)

Table 5.1. Scale-by-scale comparison between *Nelumbo nucifera* surface and the triple hierarchical superhydrophobic surface.

5.2 Fabricating an array of micro-domes with various sizes and heights with standard single layer photolithography

In order to achieve a base surface containing various sizes and heights of curved micro-protrusions, as are observed in *Nelumbo nucifera*, a standard micro-fabrication method with an additional thermal reflow step was done with the mask design shown in Figure 5.2. According to a previously reported study[2], the varying heights of the curved structures would be expected to reduce the adhesion between water drops and the surface, relative to a surface with an equivalent areal density of microstructures with equal height. For water pressures below some critical value, the water drops touch only the apex regions

of the papillae. In higher-pressure cases, e.g. perhaps the impact of raindrops, the water can intrude more deeply between the papillae and form a direct interface with the superhydrophobic solid surfaces. When the water is being shed out, either at the receding side of a moving drop or if the drop is lifted off the surface, the contact area decreases and the papillae release their contact to the water one by one, so that only few of the papillae are simultaneously in the adhesive state. Finally, right before the drop loses contact with the surface, only a few of the papillae are still in contact and cause a small adhesive force[2].

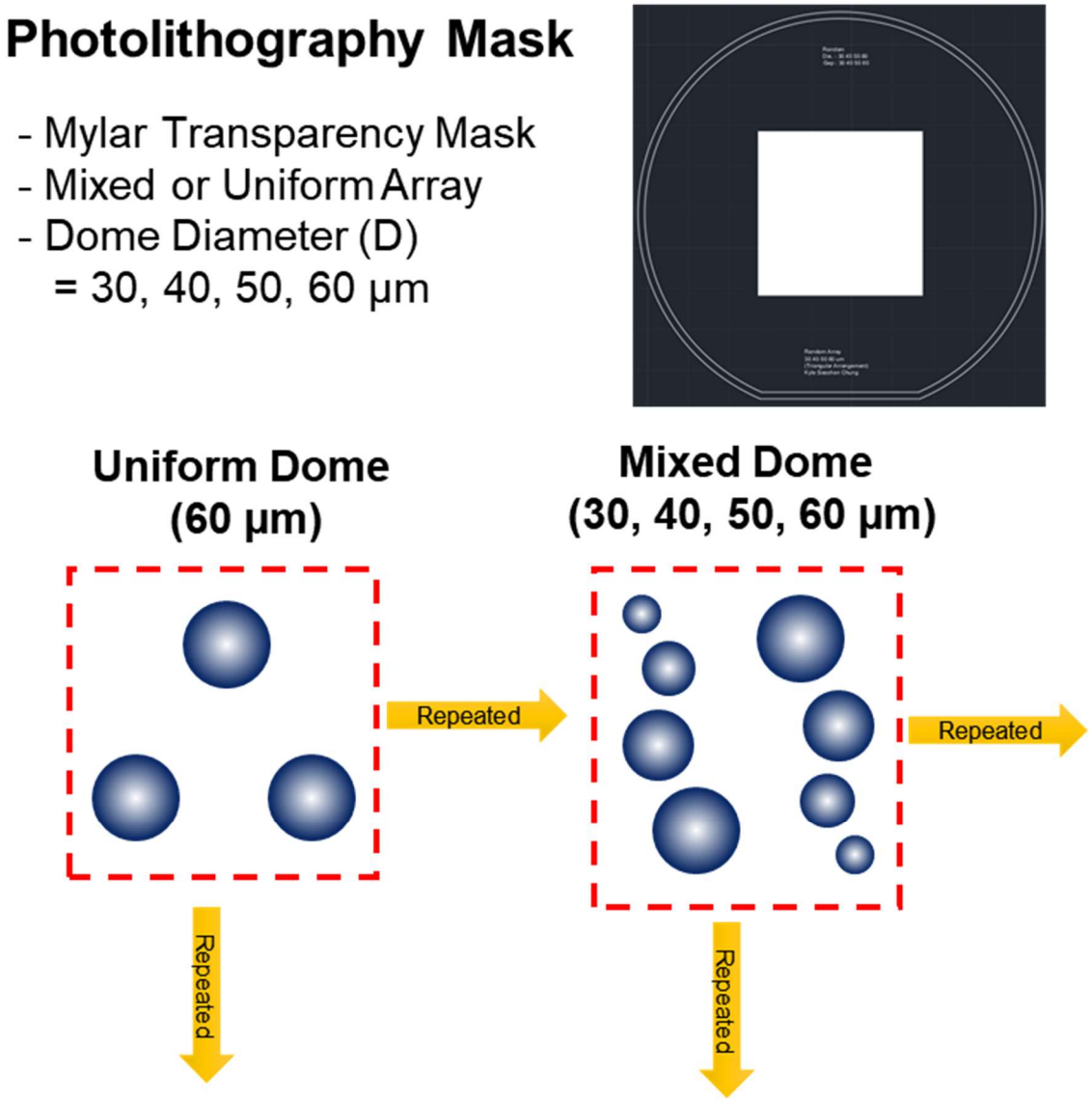

Figure 5.2. Photolithography mask design (Mylar transparency mask).

On the other hand, conventional photolithographically-made samples with pillars of equal height lead to much stronger adhesion during drop retraction when all the pillars are simultaneously in the adhesive state before contact breaks. Thus, the varying height feature is hypothesized to be highly desirable for efficient water-repellency.

In our process, two 100 mm-diameter Mylar transparency masks were designed: one with triangular arrays of circular features of the equal diameter and inter-feature spacings of 60 μm to produce the uniform dome array, and the other with square arrays of eight circular features array unit with the diameter set {1st column: 30, 40, 50, 60, and 2nd column: 60, 50, 40, 30} μm with inter-feature spacings of {1st column: 35, 45, 55, and 2nd column: 55, 45, 35} μm to produce the mixed dome array. Each mask contained the pattern arrays sized 40 mm × 40 mm and each of them was used on two different silicon wafers[62].

Two silicon wafers (100 mm-diameter) were cleaned by sequential sonication in acetone and isopropanol followed by rinsing with deionized water and dehydrated at 150 ℃ for 15 min. Then, the wafers were oxygen plasma-treated at 70 W, 200 mTorr for 5 min (O_2 plasma system, PETS Inc.). To improve the adhesion between photoresist and the wafer, an adhesion promoter, hexamethyldisilazane (HMDS, Sigma-Aldrich), was vapor-phase coated onto the wafers for 5 minutes.

AZ P4620 photoresist (PR) was spin-coated onto one of the wafers at 300 rpm for 19 sec, attained at a ramp rate of 50 rpm/s, followed by 1000 rpm for 39 sec, attained at 100 rpm/s, for a target thickness of 20 μm. The spin-coated wafer was soft-baked at 90 °C for 30 min. To prevent post-exposure cracking of the PR, the wafer was placed in a dark room for 10 min at 30–50% relative humidity to rehydrate. The wafer was then exposed to 500 mJ/cm^2 i-line (365 nm) UV in a mask aligner (Model 200, OAI) and developed for 10 min with AZ 400K. The developed wafer was rinsed with DI water, completely dried, and treated with O_2 plasma at 60 W, 200 mTorr for 10 min to descum it. This wafer was then baked at 135 °C for 1 hour to trigger a thermal reflow driven by the PR's surface tension to obtain curved micro-dome features.

As a result of the thermal reflow, the structures, which were originally circular pillar structures with various diameters after the photoresist development, now became the array of curved micro-domes with various sizes and heights. The nominal diameters of the domes were {30, 40, 50, 60} μm and the center heights after the reflow were {15.19, 19.62, 22.91, 25.09} μm, so that various heights of the micro-bumps were simply achieved by standard single-layer photolithography with reflow. These features were then transferred to polydimethylsiloxane (PDMS) elastomer via a two-stage casting process (Figure 5.3).

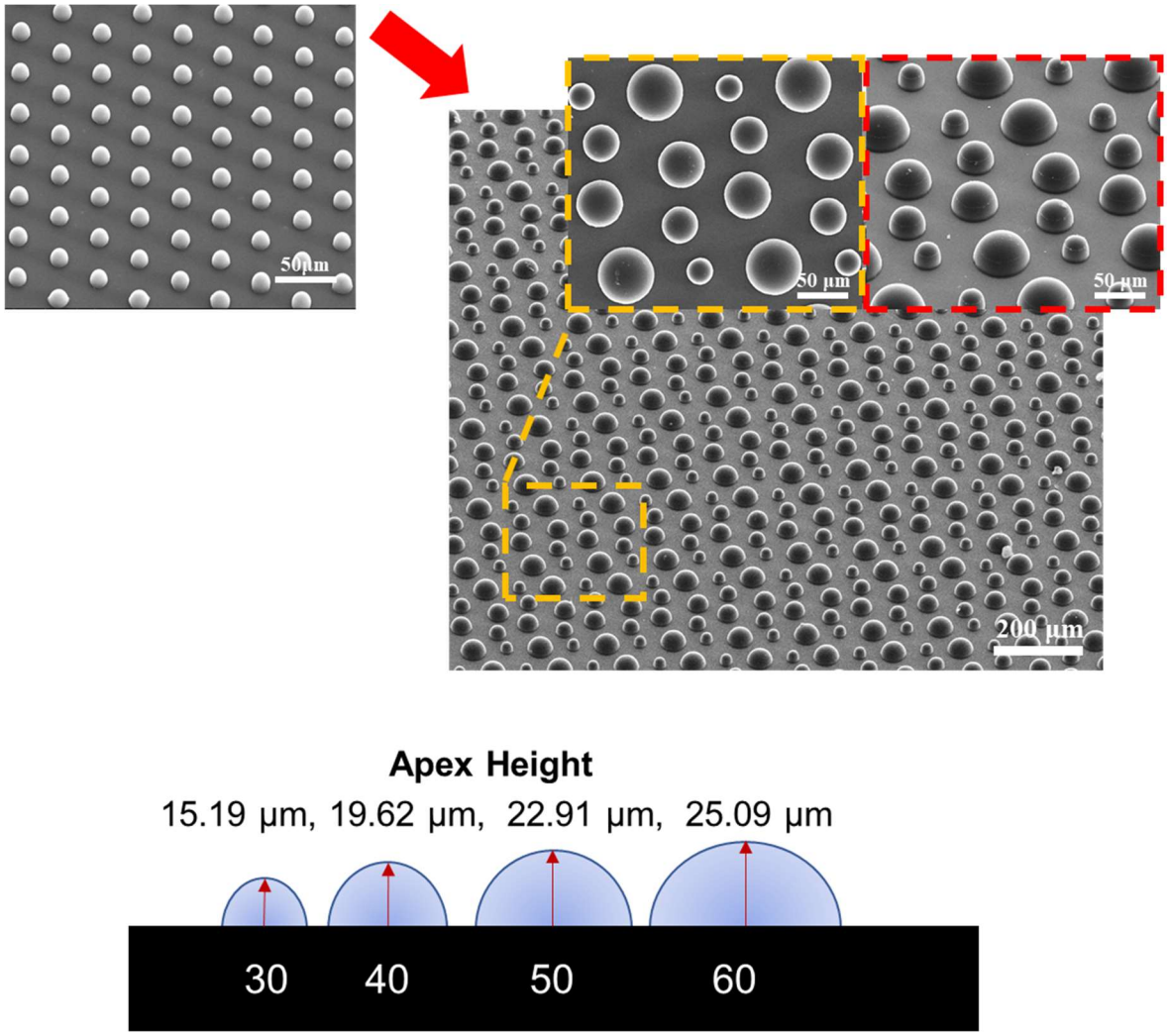

Figure 5.3. Fabricating an array of micro-domes with various sizes and heights with standard single layer photolithography

Replicas of the fabricated micro-dome structures were created in polydimethylsiloxane (PDMS, Sylgard 184, Dow Corning) via two-step casting[42]. In the first casting step, the PDMS pre-polymer and crosslinker were mixed in the ratio 5:1 and poured onto the wafer. After curing at 75 °C for 1.5 hours, this casting was oxygen plasma-treated (60 W, 200 mTorr, 2 min) and fluoro-silanized with 1H,1H,2H,2H-perfluorooctyltrichlorosilane (Sigma-Aldrich). This casting was used as the mold for the second casting step with a less rigid mixture of PDMS (pre-polymer:crosslinker :: 10:1)[62].

5.3 Maximizing polymer bi-layer buckling

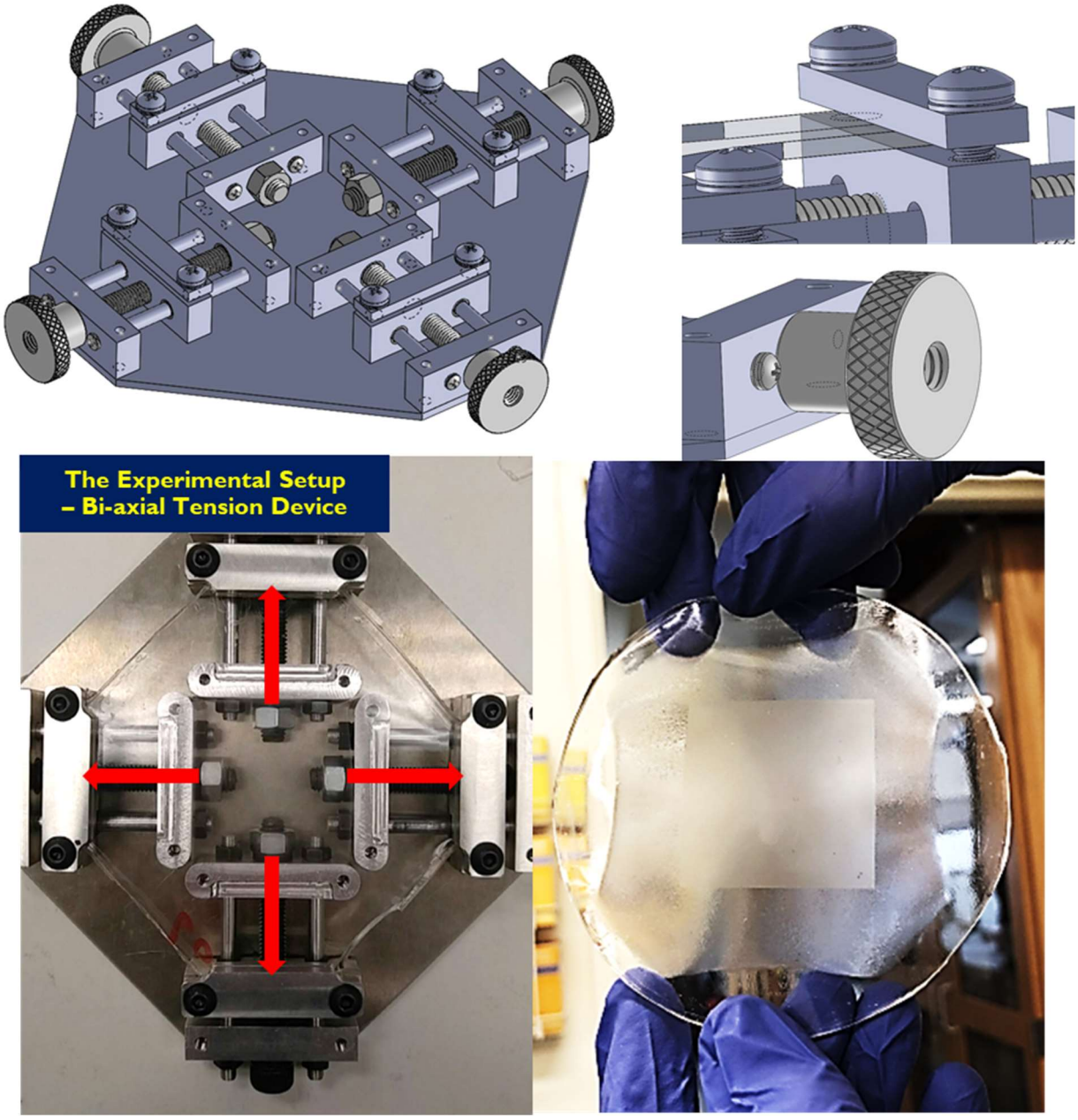

Figure 5.4. Schematic and photo of our custom built bi-axial tensile stress loader design, and photo of the sample with the surface micro-wrinkles induced.

In order to engineer periodic micro-undulations analogous to those formed by the boundaries between epidermal cells in *Nelumbo nucifera*, we carried out a mechanical stress-induced polymer bi-layer buckling process. According to previously reported studies[66,67], during the O_2 plasma or UV Ozone treatment, the top surface of the PDMS oxidizes and converts into a thin layer of glassy silicate. As a result, the PDMS sample turns into a bi-layered material with different Young's moduli. Biaxial tensile stress was applied prior to surface oxidation and released afterwards, and the bi-layered surface formed a wrinkled surface when it reached a stable state after unloading. According to the previously published results, zigzag-shaped herringbones were formed when the strains applied and relieved were sequential (releasing in X first and Y second accordingly). More randomly shaped two-dimensional wrinkles were formed when stretching and releasing simultaneously in both directions.

To apply tensile stress on our PDMS replica with the array of micro-domes by mechanical stretching, we prepared a custom-built bi-axial tensile stress loader (Figure 5.4). Our device is an aluminum-machined device with four lead-screw assemblies. All the parts are either off-the-shelf or machined from aluminum alloy stock. The four clamp assemblies can slide along linear rails, driven by M8 lead screws (four degrees of freedom, 65 mm of possible elongation space with a minimum sample diameter of 70 mm). For the operation, the PDMS sample was placed on our device, and slid into the clamp assemblies first. M5 screws are torqued to a level producing sufficient clamping force. After clamping all four ends of the sample, we manually turned the thumb nuts to drive tensile loading of samples to desired strain (e.g. if the target strain was 15 %, the center patterned region was stretched 40 → 46 mm) in both X and Y planar direction.

The stretched sample was then UVO treated (Model 42A, UVO-Cleaner, *Jelight*, Lamp power = 28,000 μW/cm^2) for the desired time, and the strain was released sequentially: X-direction first, then Y-direction[62,66]. The bottom right image in Figure 5.4 shows the result of this process.

To find the optimal size for the micro-wrinkles, we tested both oxygen plasma and UV ozone treatments and compared the results. Figure 5.5 shows scanning electron micrographs of oxygen plasma-induced wrinkles. Wrinkles with length-scales of approximately 100 nm were generated (Figure 5.5). These nano-wrinkles were induced not only on the 'ground' between microfeatures, but also across the surfaces of the dome structures. However, we found that the depths of these nano-wrinkles were too shallow to enhance superhydrophobic performance.

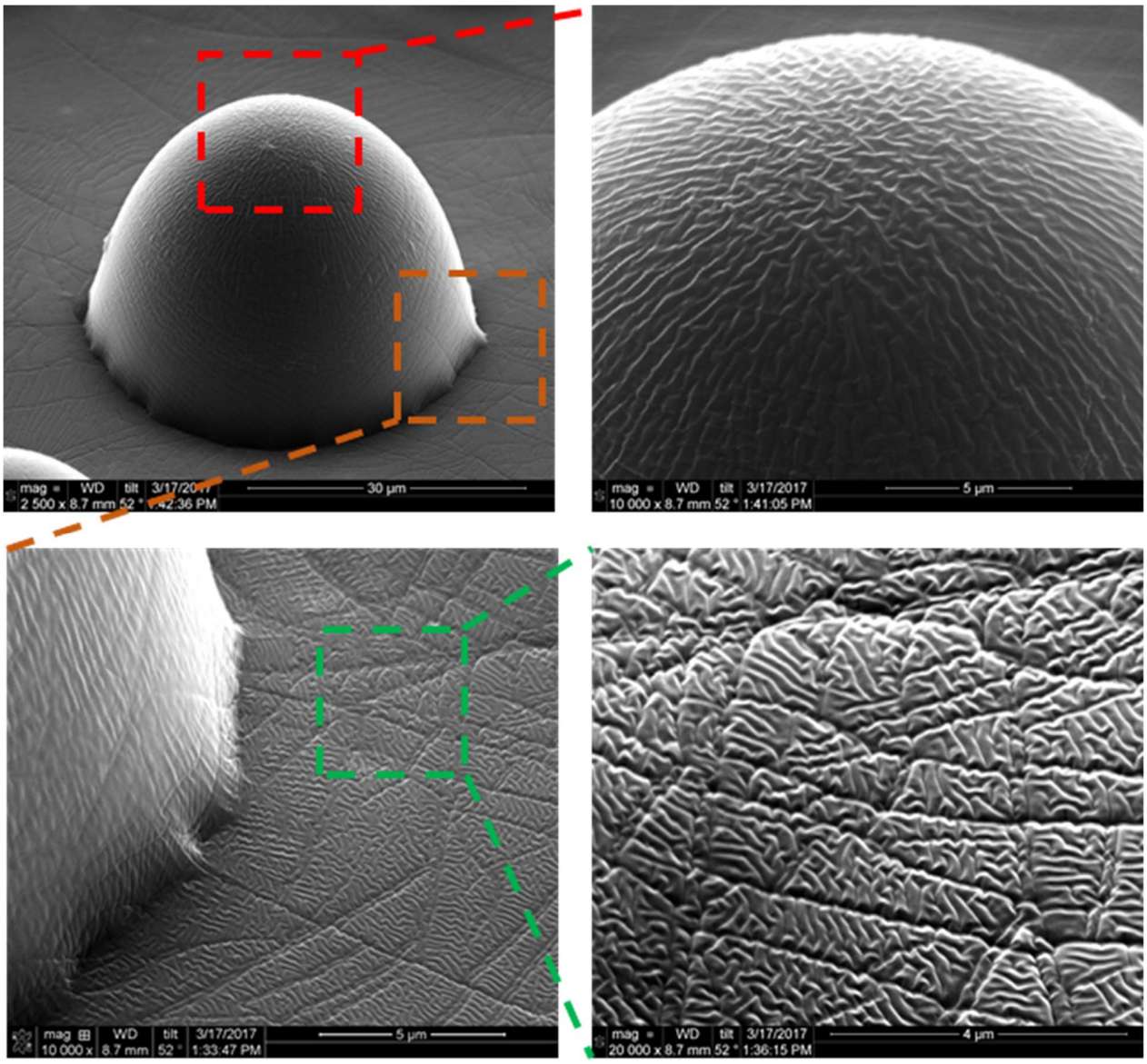

Figure 5.5. Plasma induced nano-wrinkle on PDMS surface with micro-domes. Plasma (~ 60 W, 1 min), Strain (15 %)

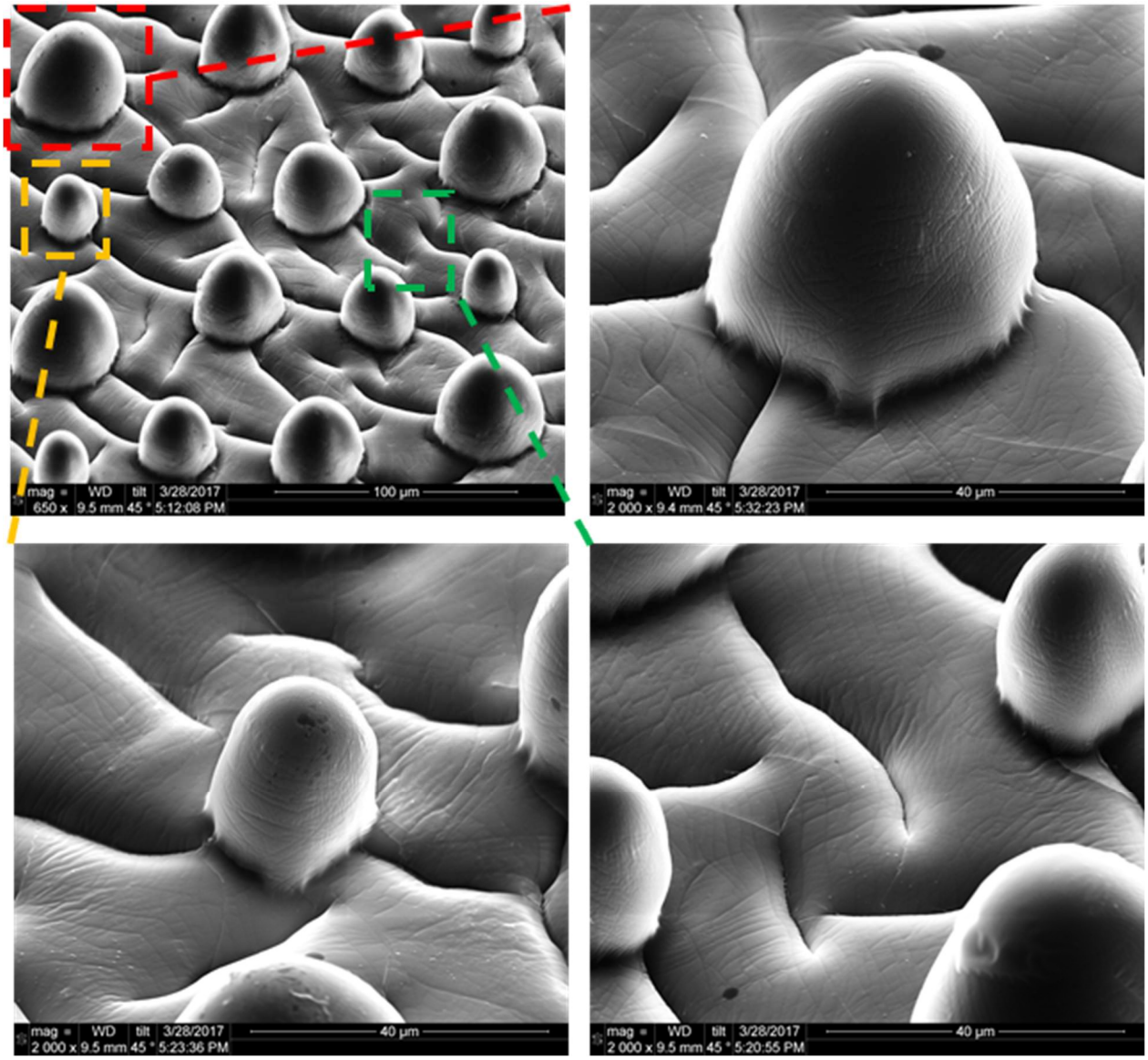

Figure 5.6. UV ozone induced micro-wrinkle on PDMS surface with micro-domes. UVO (40 min), Strain (15 %).

For comparison, we also investigated the UV ozone treatment (Figure 5.6). With this treatment, approximately 10-to-20-µm-sized micro-grooves were generated, this time only between the micro-domes and not on the domes themselves. The induced micro-grooves were about 100 times larger in size than the nanosized wrinkles from the plasma treatment.

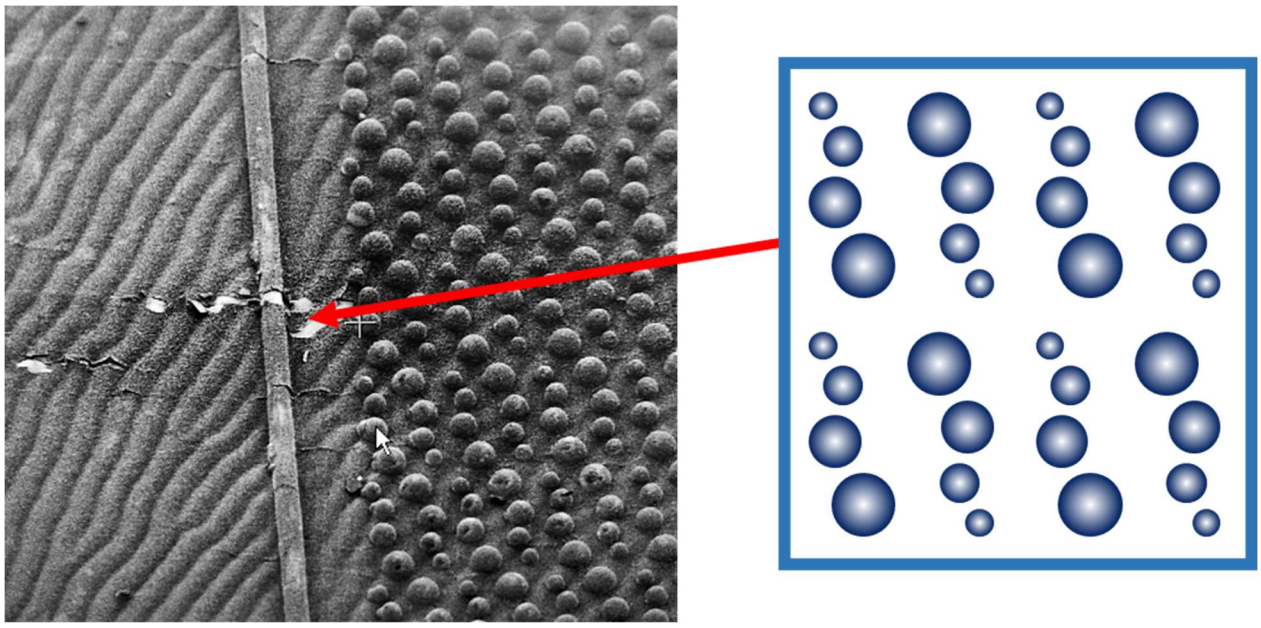

Figure 5.7. Result of polymer bi-layer buckling process on microstructures with the boundary lines

Thus, in this project[62], we chose to use UV-ozone treatment method[68], rather than the oxygen plasma treatment method described in other studies[66,67,69], in order to engineer the most suitable micro-wrinkles which not only can be located among our various-sized microdome array, but also can be big enough that was can conformally grow a zinc oxide nanoporous structure (approximately 3 μm in height) on the wrinkled surface. Also, we applied sequential release of the applied strain (first in the X direction, then in the Y direction) to provide a well-controlled energy release path for the formation of microwrinkles[70,71] in order to see the effect of presence of the microdome arrays more effectively.

Also, some of our failures showed interesting and meaningful result. The very first design of our photolithography mask had the border lines around the array of micro-domes. The purpose of having the border lines was to clearly detect the four ends of the patterned region to help measure the strain during the tension process. However, the border lines were found to act as robust energy barriers during the wrinkling process. As shown in Figure 5.7, the amplitudes of micro-wrinkles were notably reduced inside the border lines. We believe that our border lines were dissipating (or absorbing) the stress when the surface was released after the pre-strain. Therefore, we removed the border lines on our modified photomasks after these failure observations.

5.4 Conformal nanoporous structure synthesis

To obtain the smallest-scale nano-roughness in the TriSS structure, we conformally synthesized a zinc oxide nanoporous coating on top of our micro-dome array with periodic micro-undulations. This zinc oxide coating process had been previously developed in our lab[31], and its characteristic pore sizes match those of the nano-sized hairy structures observed in *Nelumbo nucifera*. The PDMS substrates with the micro-dome array and micro-wrinkles were sputtered with 20 nm chromium followed by 200 nm aluminum as the seed layer for the hydrothermal synthesis of nanoporous ZnO. The growth of ZnO followed our previously reported process, in which the aluminum-coated PDMS was immersed in a 25 mM equimolar aqueous solution of zinc nitrate ($Zn(NO_3)_2 \cdot 6\ H_2O$, Sigma-Aldrich) and hexamethylenetetramine (Sigma-Aldrich) at 70 °C for 90 minutes in an oven. After this bath synthesis, samples were rinsed in DI water, dried in a jet of N_2, and stored at room temperature[62]. The resulting ZnO nanoporous films coated the complex microstructured target surfaces remarkably conformally (Figure 5.8).

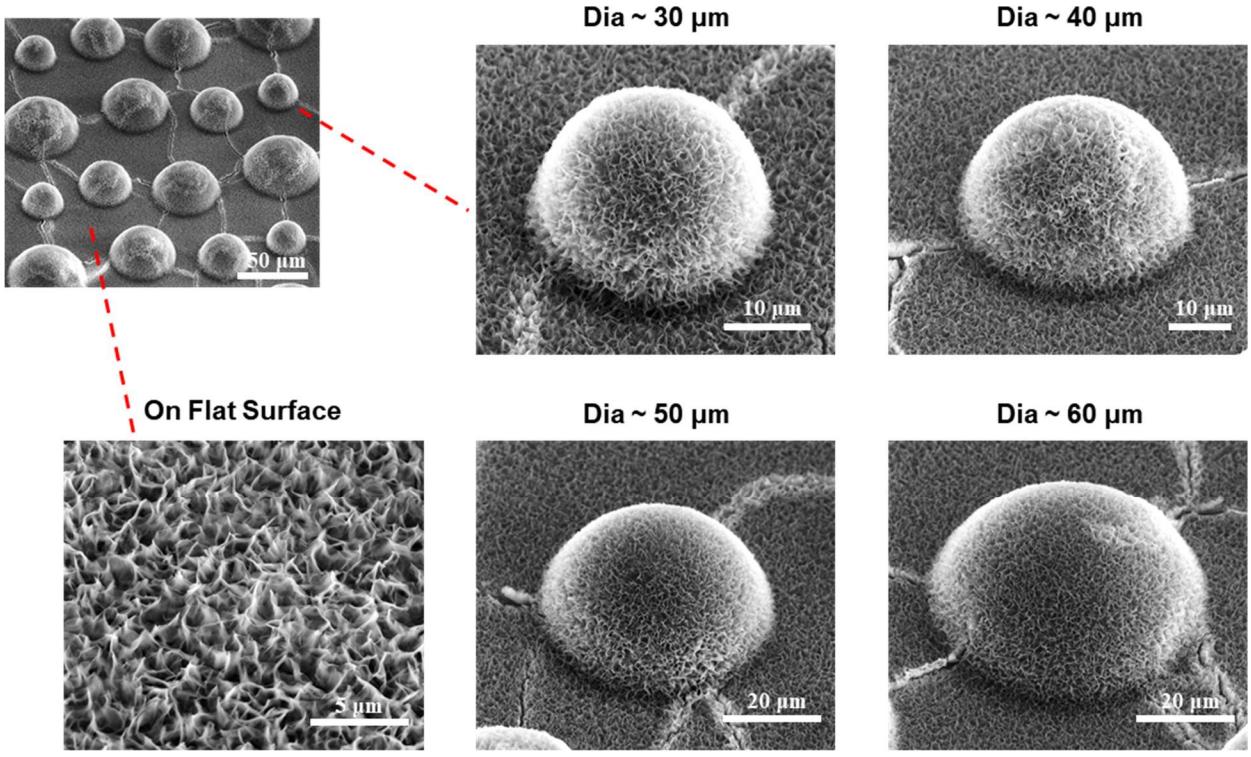

Figure 5.8. Zinc oxide nanoporous structure conformal synthesis on array of micro-domes

According to our observations, the growth height of the ZnO nanoporous structures was measured to be approximately 3.3 μm (Figure 5.9). Considering the conformal formation aspect of our ZnO nano-structure synthesis, we aimed for micro-wrinkles with a width greater than 10 μm in this project, because much smaller or narrower micro-grooves would have been totally covered and concealed by the ZnO nanoporous coating.

As the final step in achieving superhydrophobicity, a surface fluoro-silane termination process was done. 1 g of 1H,1H,2H,2H-perfluorooctyltriethoxysilane (POTS, Sigma-Aldrich) was mixed into 49 g of pure ethanol (200 proof, Decon Labs, Inc.) and the mixture was stirred thoroughly for 10 min. Sample surfaces were cleaned with isopropanol and deionized water and were treated with oxygen plasma (60 W, 200 mTorr, 2 min). The samples' surfaces were then immediately sprayed with the POTS solution mixture with a water sprayer (Ace Hardware) and were dried at room temperature for 30 min. This spraying and drying cycle was repeated four times to ensure that the surfaces were fully fluoro-silanized. Finally, the samples were rinsed with pure ethanol and allowed to cure at room temperature in a fumehood for 24 hours[62].

5.5 Overview of the triple hierarchical superhydrophobic surface (TriSS) and its fabrication process

Inspired by the actual hierarchical surface of nature (e.g. lotus and taro leaf) which consists an array of micro-scale protrusions with nano-scale hairy structures and grooves between the protrusions, we developed a novel triple hierarchical superhydrophobic surface (TriSS)[62], which has a distinctive artificial three-tier surface roughness (Figure 5.9a). Although controlled wrinkling on flat surfaces by mechanical stretching has been explored by others[66,67], we demonstrated in this work that the presence of the various sized micro-domes strongly affects the wrinkling and generates highly complex surface undulations that could not easily be formed by any type of conventional manufacturing technology. Then, aluminum is sputtered onto the surface and used as the seed layer for hydrothermal growth of zinc oxide nanoporous structure[31]. This process, coated with a hydrophobic surface termination such as fluorosilanization, creates a superhydrophobic triple-level complex surface (Figure 5.9b).

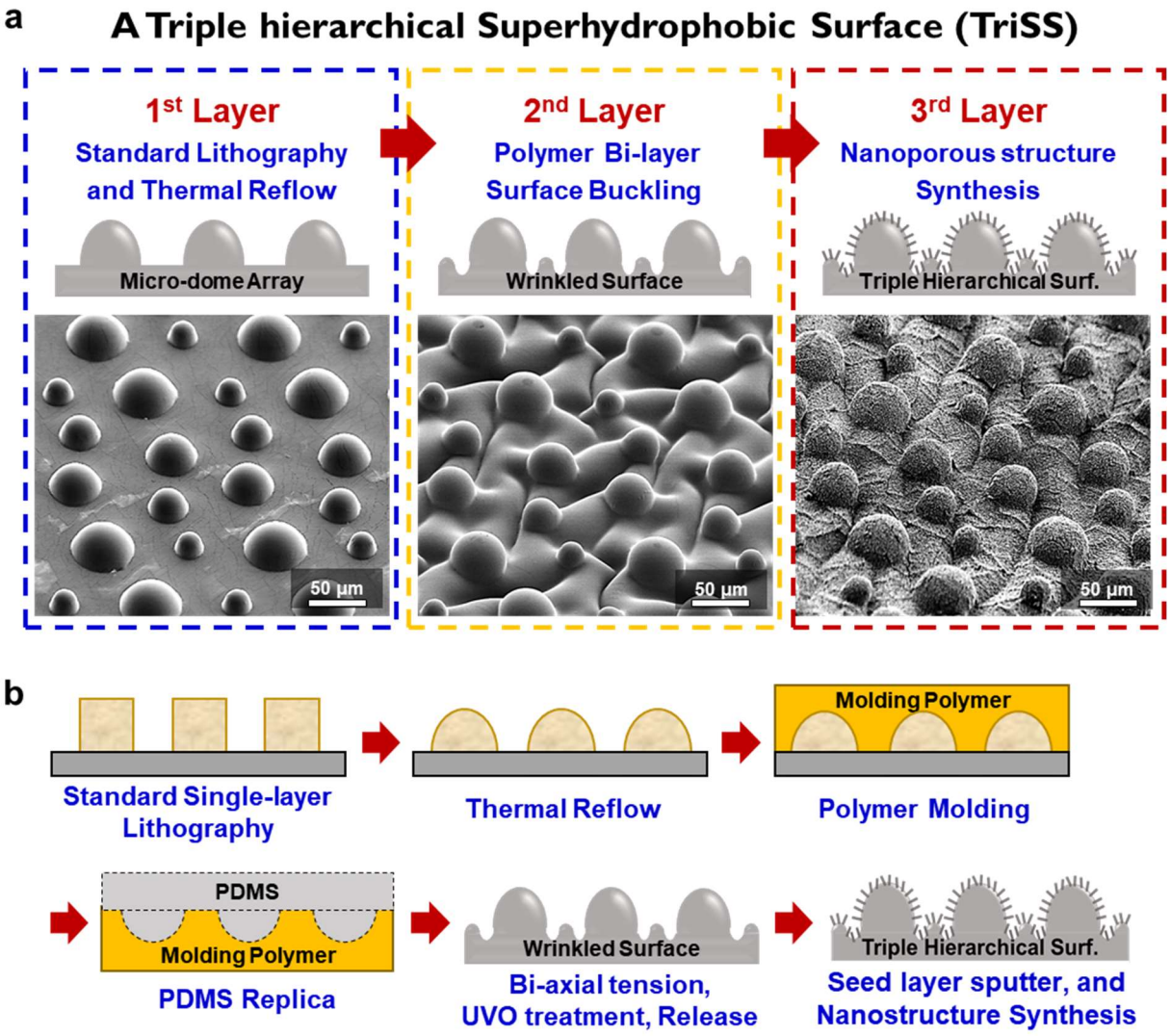

Figure 5.9. Overview of our Triple-hierarchical Superhydrophobic Surface. (a) Inspired by water-repellent examples from nature (e.g. lotus and taro leaf structure) which have an array of micro-sized domes with nano-sized hairy structures and periodic grooves in the middle of the domes, the novel triple hierarchical superhydrophobic surface with the microdome arrays (1st layer), the surface micro wrinkles (2nd layer), and the nano-porous structures (3rd layer) was precisely manufactured using a standard single-layer photolithography, polymer bi-layer deformation, and a simple hydrothermal bottom-up nanostructure synthesis. (b) Schematic of our process flow. (1) Single-layer photolithography; (2) followed by reflow; (3,4) transfer to PDMS by double-casting; (5) biaxial strain imposed, UVO exposure, and wrinkles induced by the sequential strain release (horizontal direction first, vertical direction next); (6) hydrothermal ZnO growth. The nominal diameters of the domes are {30, 40, 50, 60} μm with the center heights after re-flow were {15.19, 19.62, 22.91, 25.09} μm.

The fabrication process for our triple hierarchical superhydrophobic surface starts with standard single-layer photolithography (Figure 5.9b), followed by thermal reflow in which the surface tension of the heated photoresist creates features with a curved surface. The nominal diameters of the domes are {30, 40, 50, 60} μm with the center heights after the reflow were {15.19, 19.62, 22.91, 25.09} μm, so that various heights of the micro-bumps were simply achieved by the standard single-layer photolithography with reflow, which are then transferred to polydimethylsiloxane (PDMS) elastomer via a two-stage casting process. This replica is subjected to biaxial tensile strain, treated with UVO, and then sequentially released (horizontal direction first, then vertical direction) to its original state to induce a micro-groove pattern inside the array of the microdomes. Finally, the surface is sputtered with an aluminum seed layer and a ZnO nanoporous film is conformally coated through hydrothermal synthesis. This process flow allows a surface with distinctive artificial three-tier hierarchical structures to be manufactured rapidly[62].

5.6 Comparisons of wrinkle morphologies induced on surfaces with presence of microstructures

The morphologies of our induced microwrinkles were strongly affected by the geometry of the micro-domes, UVO exposure time, and the amount of pre-strain (Figure 5.10). Three different surfaces were investigated for comparison of wrinkle morphology; flat surfaces (no microstructures), surfaces covered with a regular hexagonal packed array of micro-domes (uniform diameter and spacing of 60 μm), and surfaces patterned with a micro-dome array containing mixed diameters {30, 40, 50, 60} μm.

Firstly, we found that at the fixed 15% biaxial pre-strain, increasing the UVO exposure duration made the wrinkles' widths larger and their lengths longer (Figure 5.10a–i). On the flat surfaces with no microstructure, the microwrinkles evolved into short checkerboard, long checkerboard, and herringbone shapes with the increased UVO exposure time (Figure 5.10a–c). These morphologies were similar to those described in previous work on the nonlinear analysis of wrinkle formation[70,71]. However, with the presence of the microdome array on the surface, the evolved microgrooves were highly distinctive. We believe that, when the pre-strain was released, the surface micropatterns acted as local nodes (or stress zero points) for the energy release and led to a preferential surface buckling direction, as explained in similar mechanisms of controlled wrinkle formation with thermal expansion and plasma oxidation[69].

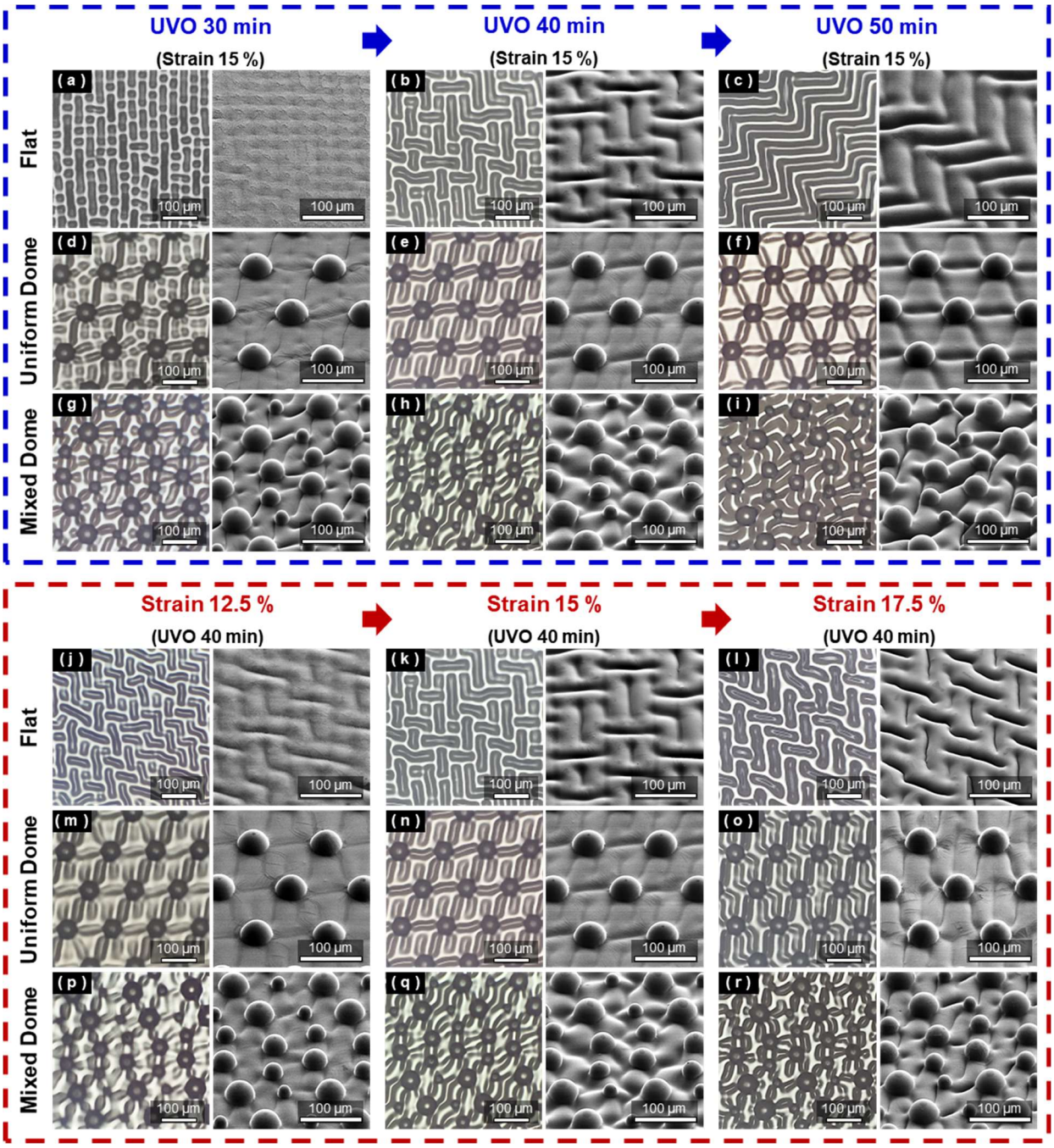

Figure 5.10. Comparisons of wrinkle morphologies induced on initially flat surfaces (no microstructures), surfaces covered with a regular hexagonal packed array of micro-domes (uniform diameter and gap of 60 μm), and surfaces patterned with a micro-dome array containing mixed diameters (30, 40, 50, 60 μm) after various UVO exposure times (30, 40, 50 min) with constant biaxial strain of 15% (a–i) and after various biaxial tensile strains (12.5, 15, 17.5%) with constant UVO exposure of 40 minutes (j–r), respectively. In our process, PDMS replica of 100 mm diameter had the center region (40 × 40 mm) which consist the micro-domes of interest. Then this replica was clamped and stretched to the target strain (if the target strain was 15 %, the center

region was stretched 40 → 46 mm) in both X and Y planar direction. The stretched sample was then UVO treated for certain time and the strain was released sequentially; X-direction first, then Y-direction. Each sub-figure has two images: an optical microscope image (left) and a scanning electron microscope (SEM) image with 45° tilted view (right). All the scale bars are 100 μm.

In the case of our uniform dome array, the short and the long checkerboard and the herringbone patterns, which were observed on the flat surface, evolved into similar patterns but confined to a lattice formed by the array of micro-domes (Figure 5.10d–f). As a result, the morphology of microgrooves induced with the 50-minute UVO exposure and 15% biaxial pre-strain (Figure 5.10f) were found to be completely regular in form when they were imposed onto a hexagonal array of domes with diameter and separation of 60 μm, resulted in a robustly periodic wrinkled surface with three-fold rotational symmetry that was templated strongly by the micro-domes. More interestingly, the mixed dome array, a micro-dome array consisting of multiple feature sizes, further modified the groove formation (Figure 5.10g–i).

We believe that the presence of various-sized domes acted as various-sized local nodes (or various-sized stress zero points) when the pre-strain was released, and finally led to the formation of highly complex surface buckling morphologies. In particular, the wrinkles induced with UVO exposure of 50 minutes and 15% biaxial pre-strain showed remarkable surface geometric complexity with maximized-height undulations that were templated strongly by the multiple-sized micro-domes. This effect resulted in surface distortions which even led to a change of the facing direction of the micro-dome's apex, away from a vertical angle (Figure 5.10i), giving the strongest resemblance to the actual surface of the lotus leaf.

Meanwhile, at constant UVO exposure of 40 minutes, varying the amount of pre-strain also resulted in a different evolution of wrinkle morphologies, but in all cases wrinkles were strongly templated by the existing micro-dome patterns (Figure 5.10j–r). While the lower pre-strain cases (12.5 and 15%, Figure 5.10j–k, 5.10m–n, 5.10p–q) induced a similar wrinkle morphology to the wrinkles induced with lower UVO exposure times (30 and 40 minutes, Figure 5.10a–b, 5.10d–e, 5.10g–h), the release of 17.5% of pre-strain formed vertically-dominant wrinkles (Figure 5.10l, 10o, 10r).

A possible physical explanation is that when the stress is released in the X-direction, an array of vertically oriented ripples is induced, and a deeper wrinkle amplitude is generated with the higher pre-strain, as suggested by recent theories[67,70]. However, when the pre-strain is released in the second Y-direction, the new array of horizontally

oriented ripple-shaped rows is infused into the pre-made vertical ripple column array. In this process, we believe that although the magnitudes of the first buckling force in the X-direction (due to the X release) and the second buckling force in the Y-direction (due to the Y release) are approximately equal, the wrinkles resulting from the second buckling event can be weaker since the sample surface after the first release is no longer a flat surface but an array of vertical ripples.

As a result of our comparisons of wrinkle morphologies induced on different surfaces, we chose the morphologies shown in Figure 5.10f and Figure 5.10i as representing the best process parameters for the uniform dome and the mixed dome cases, respectively, for further performance comparison[62].

5.7 Static and dynamic contact angle comparisons of surfaces with increasing surface complexities

For the static and dynamic contact angle measurements, we used a custom-built goniometer set-up. For static contact angle measurements, five water droplets (~7 μL) were deposited onto different locations of each sample and measured. Also, video of each droplet was recorded, viewed from the edge of the substrate using a camera (DCC1645C, Thorlabs). Images were analyzed in ImageJ[43]. Static contact angles were extracted using the Low-Bond Axisymmetric Drop Shape Analysis (LB-ADSA) ImageJ plug-in[44]. For dynamic contact angle measurements, the sample stage was then tilted until the droplet rolled off, and the Drop-Snake ImageJ plug-in[45] was used to extract advancing and receding contact angles from the video frame captured immediately prior to roll-off. Hysteresis is calculated as the difference between advancing and receding angles.

In Figure 5.11, the superhydrophobic performance characteristics of five different samples are presented in order of increasing surface complexity. Figure 5.11a shows the SEM images (upper row) and corresponding schematics (lower row) of our representative samples:

1. Zinc oxide (ZnO) nanoporous structure on flat surface without microstructures;
2. Double hierarchical surface - ZnO nanostructure synthesized on uniform dome (60 μm) array;
3. Double hierarchical surface - ZnO nanostructure synthesized on mixed dome (30, 40, 50, 60 μm) array;
4. Triple hierarchical surface - ZnO nanostructure synthesized on uniform dome array with micro-grooves (Figure 5.10f Case).

5. Triple hierarchical surface - ZnO nanostructure synthesized on mixed dome array with micro-grooves (Figure 5.10i Case).

All the samples are 1H,1H,2H,2H-Perfluorooctyltriethoxysilane (POTS) coated for hydrophobic surface termination[62].

Optical microscopy of water droplets placed on our surfaces showed that they remained suspended on top of the structures (Cassie–Baxter mode) and did not infiltrate into patterns (Wenzel mode)[3]. The plot of water sessile contact angle shows a clear increasing trend with increasing surface complexity (Figure 5.11b). The highest water sessile contact angle, 174.3±0.3° (mean ± standard error of the mean, N = 5), was achieved on our triple hierarchical surface with the mixed dome array (Sample 5). This result was more than 13° higher than obtained with the 'flat' ZnO (Sample 1). Interestingly, both in the double and triple hierarchical cases, average contact angle on the array of mixed dome was approximately 2.5 – 3.5° higher than the surfaces of uniform dome. Also, having additional surface roughness with the micro-wrinkles increased the average contact angle by 4 – 5° in both the uniform and mixed dome cases.

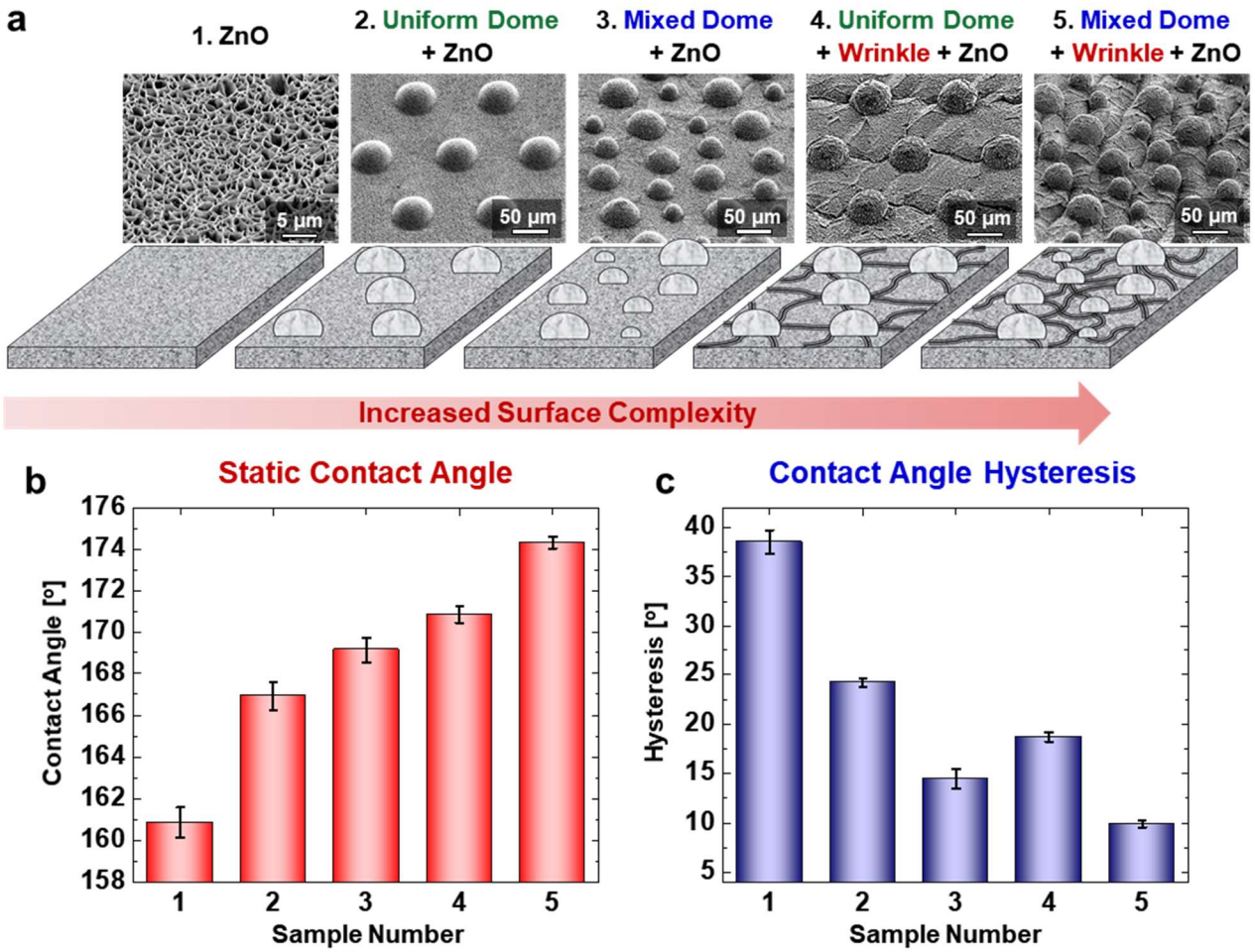

Figure 5.11. Static and dynamic contact angle comparisons of surfaces with increasing surface complexities. (a) SEM images and schematics of 5 different surfaces; Labeled as 1. Zinc oxide (ZnO) nanoporous structure on flat surface without microstructures, 2. Double hierarchical surface - ZnO nanostructure synthesized on uniform dome (60 µm) array, 3. Double hierarchical surface - ZnO nanostructure synthesized on mixed dome (30, 40, 50, 60 µm) array, 4. Triple hierarchical surface - ZnO nanostructure synthesized on uniform dome array with micro-grooves (Figure 5.10f case). 5. Triple hierarchical surface - ZnO nanostructure synthesized on mixed dome array with micro-grooves (Figure 5.10i Case). All the samples are POTS coated. (b) Comparison of water sessile contact angle on 5 surfaces. Error bars represent ±1 standard error of the mean; five droplets per specimen. (c) Contact angle hysteresis (dynamic contact angle) comparison. Error bars represent ±1 standard error of the mean; sample size is five separate droplet sheddings per specimen.

These enhancements are compatible with existing theories of the partial liquid–solid contact[3,27]. Adding an additional surface roughness (e.g. micro-grooves) reduces both the linear and areal liquid–solid contact fractions when suspended on the tips of the roughness.

Also, the curved tips of the micro-dome array allow the contact fraction to vary in order to minimize the total energy of the liquid droplet system, with contact only occurring at and near the apex of each dome[41]. Furthermore, having varying heights of the domes (our mixed-dome case) improves the surface to achieve outstanding water-repellent characteristics by further reducing the equilibrium liquid–solid contact fraction while being expected to maintain robustness against wetting when external energy inputs are introduced (e.g. by droplet impact).

Sample Number	1	2	3	4	5
Static Contact Angle	160.9 ± 0.7 °	166.9 ± 0.7 °	169.1 ± 0.4 °	170.9 ± 0.4 °	174.3 ± 0.3 °
Contact Angle Hysteresis	38.5 ± 1.2 °	24.2 ± 0.4 °	14.5 ± 1.0 °	18.7 ± 0.5 °	9.9 ± 0.3 °

Table 5.2. Static and dynamic contact angle comparisons of surfaces with increasing surface complexities

The plot of contact angle hysteresis also showed a clear but different trend (Figure 5.11c). Similar to the sessile contact angle results, samples with increased surface complexity achieved more desirable performance, in this case lower contact angle hysteresis: the lowest hysteresis observed was 9.9±0.3° for the triple hierarchical surface with the array of mixed micro-domes (Sample 5). When a surface has lower hysteresis, it can easily shed water droplets[27,48], suggesting that surfaces with multiple levels of hierarchical roughness can be attractive for greater ease of water removal.

However, an interesting observation was found in the comparison between uniform-size and mixed domes; the hysteresis observed on the double hierarchical surface with mixed domes (14.5±1.0°, Sample 3) had a slightly lower value than obtained with the triple hierarchical surface with uniform dome (18.7±0.5°, Sample 4). We believe that the varying height features in Sample 3 greatly minimized the liquid–solid contact fraction so that the hysteresis improvement by having multiple heights (about a 9.7° reduction from Sample 2 to Sample 3) was more effective than the improved hysteresis achieved by having micro-wrinkles between the domes (about 5.5° reduced from Sample 2 to Sample 4), and thus the lowest hysteresis was observed in Sample 5[62].

5.8 Water impingement resistance (underwater superhydrophobicity) performance comparisons of surfaces with increasing surface complexities

The last challenge for our five different superhydrophobic surfaces is the resistance to water impingement under high pressure circumstances (e.g. condensation accumulation, or underwater applications). Resistance to water impingement is highly desirable, since otherwise, a huge contact angle hysteresis increase can occur and cause droplets to stick after impact (reflecting a transition from the Cassie–Baxter to the Wenzel state), instead of shedding from the surface[72–77].

According to other literature, when air cavities (otherwise known as an air *plastron*) are captured inside the structural roughness of a superhydrophobic surface and immersed into water, their stability follows a similar principle as has been applied to sessile droplet cases, but with the droplet size being much larger than the surface structures[78]. As studied in Chapter 5.1, the wetting transition (during which water totally impregnates the structures) happens when the pressure from the liquid exceeds certain values[77,77,79].

Previous, related studies[55,80] have showed that the leaves of *Nelumbo nucifera* lost their superhydrophobicity after they were submerged in water for few minutes because the surface changed from the Cassie state to the Wenzel state. A transition from the Cassie state to the Wenzel state was also reported during evaporation of water droplets the superhydrophobic surfaces[81,82]. It was observed that the transition to the Wenzel state can happen when the liquid–air interface is subjected to a dynamic pressure that disturbs the static equilibrium. Similarly, other experiments have shown that the air plastron present on a submerged superhydrophobic surface decreased gradually with immersion time, and eventually the surface became totally wet[83]. Once the superhydrophobic surface reaches the Wenzel state, the surface no longer repels water and it acts as a hydrophilic surface until the surface is completely dried. Therefore, it is important for a robust water-repellent surface not only to trap air within the surface roughness but also to effectively resist water impingement and sustain the Cassie state for as long an immersion time as possible.

Schematic comparisons of expected scenarios are provided in Figure 5.12. In general (for a normal atmospheric environment), the wetting state is determined by the properties of the three-phase-contact line (TCL), van der Waals forces, and Laplace

pressure. Both the surfaces with double hierarchy and triple hierarchy were expected to resist water impalement effectively. However, it was found that water could penetrate the double-hierarchical structures after certain period of immersion, whereas our triple-hierarchical surface (TriSS) could maintain the air plastron for a much longer time.

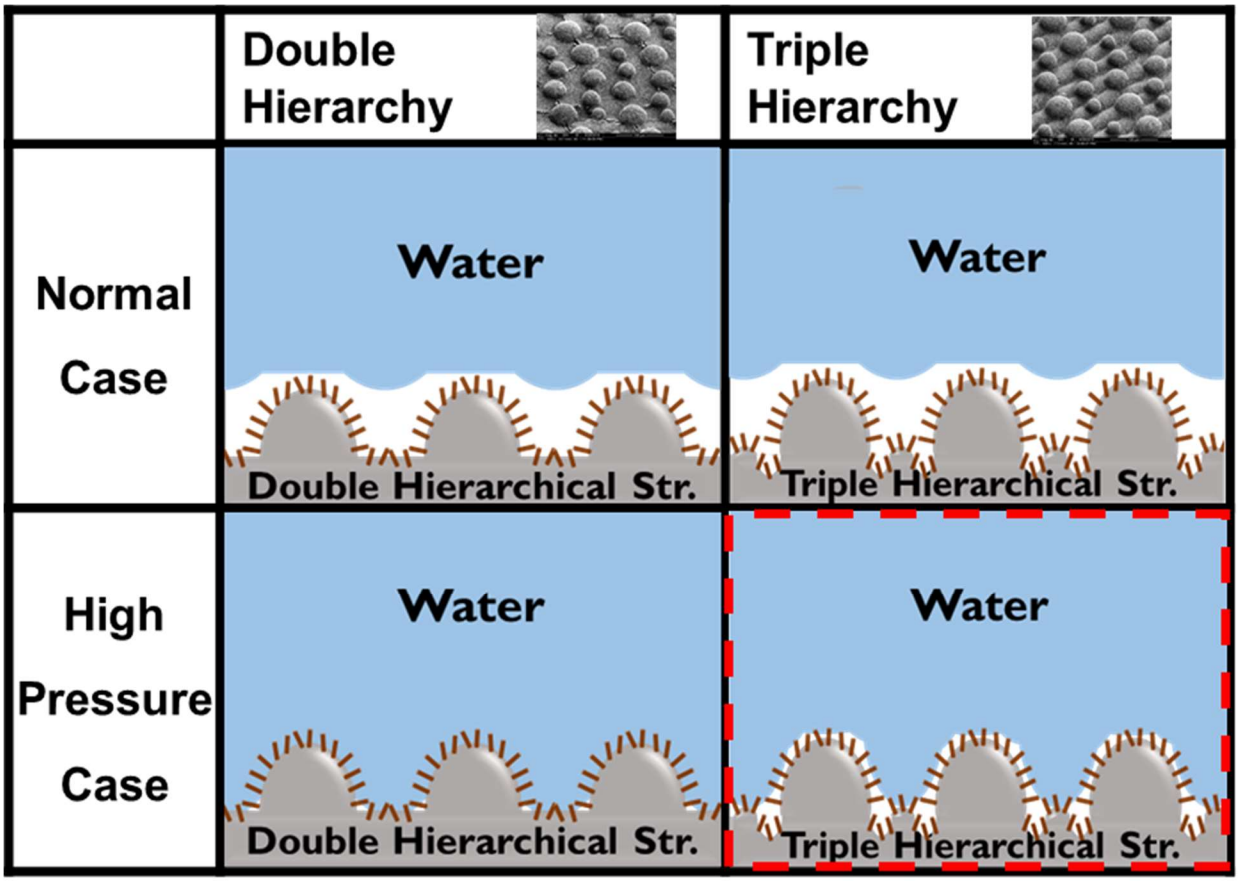

Figure 5.12. Schematic of our high-pressure underwater experiment (extreme case characterization). In general (normal atmospheric environment), the water-surface state is determined by the property of the three-phase-contact line (TCL), van der Waals forces, and Laplace pressure. However, when exposed to higher water pressure (emulating, e.g., raindrop impact or possibly condensate accumulation) water can penetrate (or impinge) between the structures.

In order to compare the water impalement resistance, we observed our surfaces in underwater environments. The immersion depth we chose was approximately 21 cm, which results in a hydrostatic pressure approximately four times larger than the weight of a droplet of 7 μL exerts on a superhydrophobic surface during a conventional water sessile contact

angle measurement. To select the immersion depth of 21 cm, we performed the calculations detailed below.

Assumptions: The volume of a droplet used in static contact angle measurements elsewhere in this dissertation is ~7 µL; the water sessile contact angle of a superhydrophobic surface is ~170 °; the shape of the droplet contact area is circular with a radius of 'c'; the direct action on the surface of the vertical component of the surface tension of water is negligible.

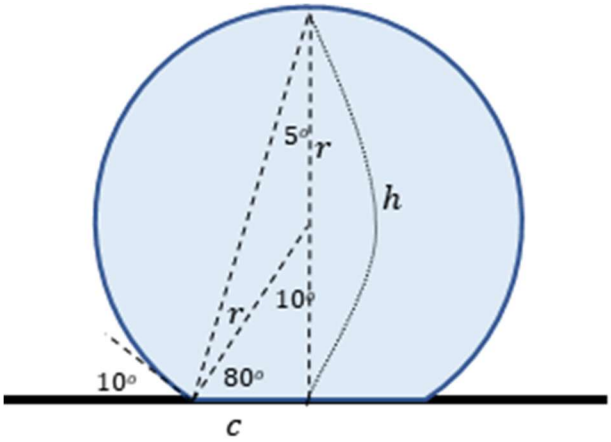

Figure 5.13. Droplet placed on superhydrophobic surface.

Calculation: We first calculate the pressure that the droplet exerts on the superhydrophobic surface. From the droplet geometry (Figure 5.13):

$$c = h\tan 5° \;\rightarrow h = \frac{c}{\tan 5°},$$

$$\mathrm{c} = r\,cos\,80° \;\rightarrow r = \frac{c}{\cos 80°}.$$

$$Water\ droplet\ volume(V) = (Sphere\ volume) - (Bottom\ cap\ volume)$$

$$= \frac{4}{3}\pi r^3 - \frac{1}{6}\pi(2r-h)[3c^2 + (2r-h)^2]$$

Plugging in h and r from the geometric relation above:

$$= \frac{4}{3}\pi\left(\frac{c^3}{cos^3 80°}\right) - \frac{1}{6}\pi\left(\frac{2c}{\cos 80°} - \frac{c}{\tan 5°}\right)\left[\frac{3c^2}{cos^2 80°} + \left(\frac{2c}{\cos 80°} - \frac{c}{\tan 5°}\right)^2\right]$$

$$= \frac{4}{3}\pi c^3\left(\frac{1}{cos^3 80°}\right) - \frac{1}{6}\pi c^3\left(\frac{2}{\cos 80°} - \frac{1}{\tan 5°}\right)\left[\frac{3}{cos^2 80°} + \left(\frac{2}{\cos 80°} - \frac{1}{\tan 5°}\right)^2\right]$$

$$= c^3\,(\,799.572 - 4.556\,) = 795.016 \times c^3 = 7\ \mu L\,,$$

$$\therefore c = 2.065 \times 10^{-4}\ [m]$$

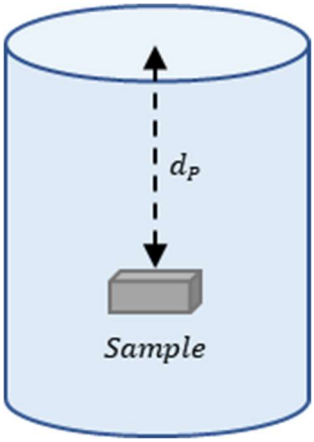

Figure 5.14. Sample immersed at the depth (d_P)

$$\therefore Pressure\ of\ sessile\ water\ droplet\ (P) = \frac{(Droplet\ weight)}{(Wet\ area)} = \frac{\rho V g}{\pi c^2}$$

$$= \frac{(997)(7 \times 10^{-9})(9.8)}{1.339 \times 10^{-7}} = 510.786\ [N/m^2]$$

We now compute the immersion depth d_p at which the hydrostatic pressure equals P (see Figure 5.14):

$$\rho g\, d_P = P = \frac{\rho V g}{\pi c^2}$$

$$\therefore d_P = \frac{V}{\pi c^2} = 0.0523\ [m] = 5.23\ [cm]$$

Therefore, similarly, the immersion depth for a pressure of '4 P' is:

$$d_{4P} = 4 \times d_P = 20.92\ [cm] \approx 21\ [cm]$$ [62].

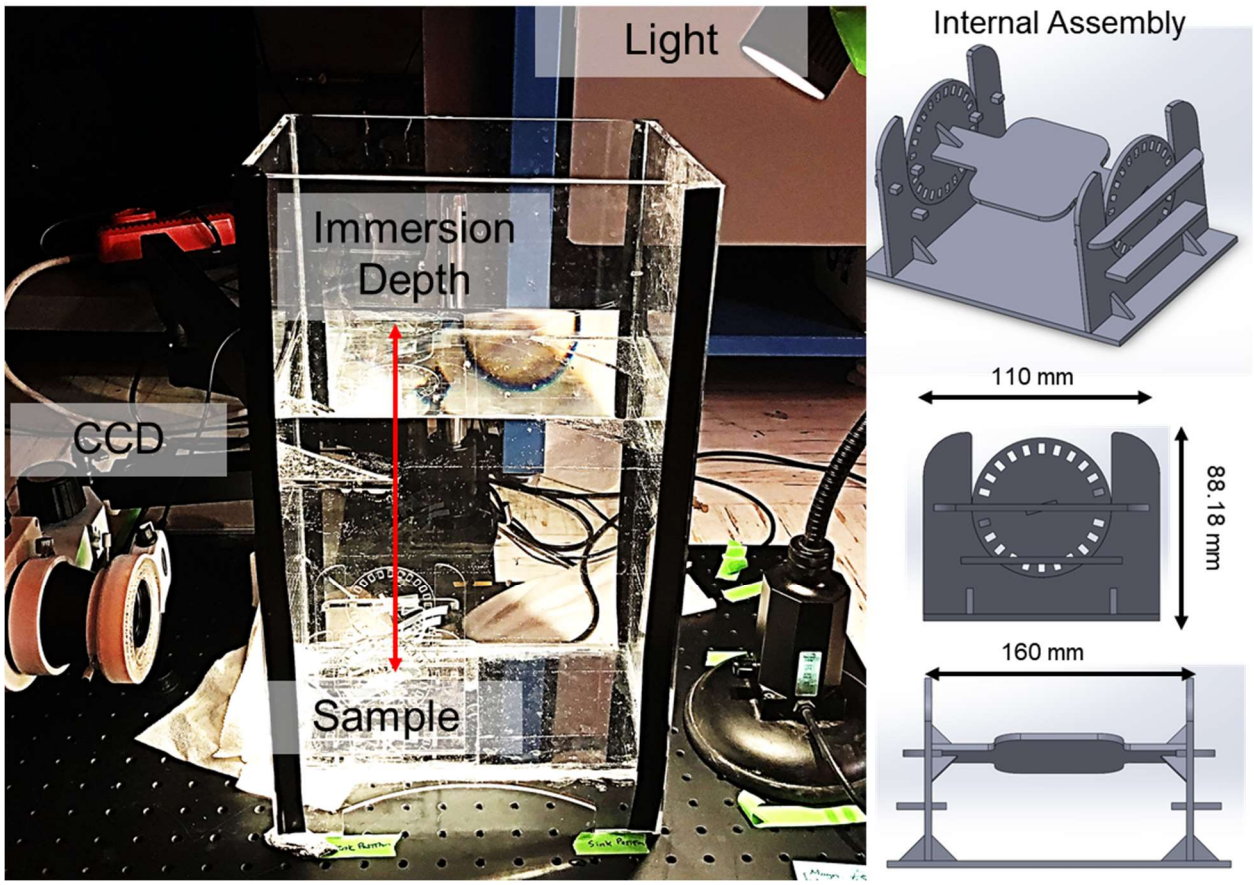

Figure 5.15. Custom-built experiment setup for underwater superhydrophobicity performance (or water impingement resistance)

Samples were analyzed in an underwater environment inside a transparent container using a camera (DCC1645C, Thorlabs), and a light source (20 W halogen lamp, LEVENGER) (Figure 5.15). By imaging the total internal reflection from any air–water boundary on the surface, the presence or absence of a plastron at any given time could be detected. The relative intensity of the reflected light was analyzed using ImageJ by converting the images to grayscale. Relative intensity was quantified by calculating the percentage of pixels in the imaged region that exhibited a relatively high reflected intensity and could therefore be assumed to be part of the plastron[5,9,84,85]. After the container was filled with water, the sample, attached to an acrylic plate, was immersed, face-down, into the water at a depth of approximately 21 cm. The relative intensity measured was plotted against the amount of time that the sample was immersed.

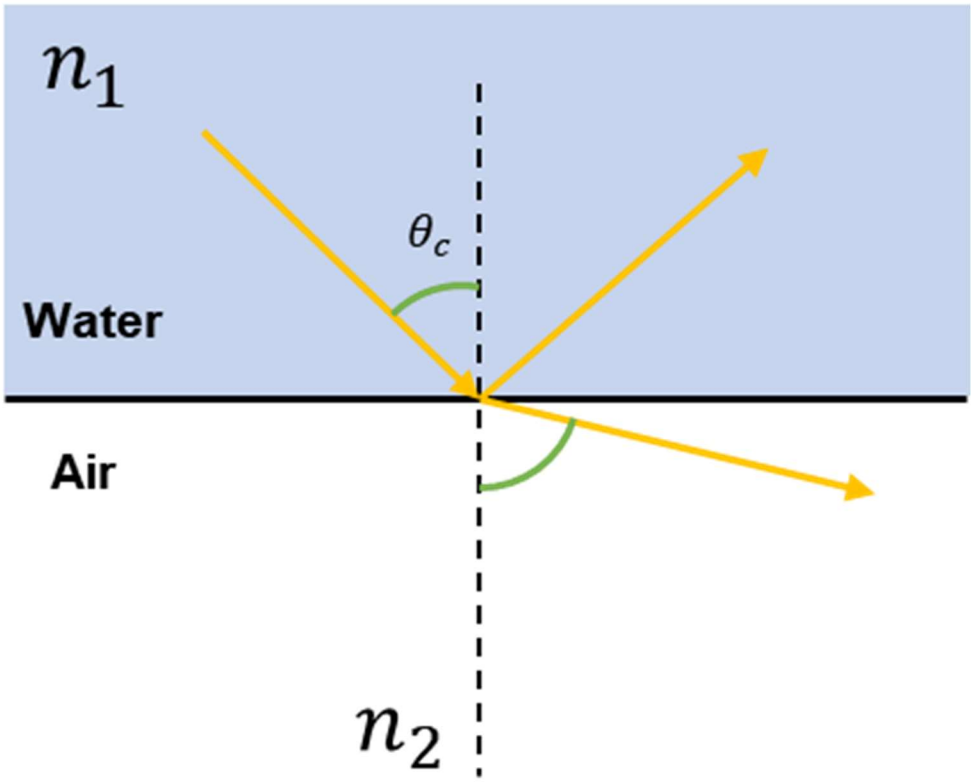

Figure 5.16. Total internal reflection can happen on the air plastron. With indices of refraction for water and air equal to 1.33 and 1, respectively, the critical angle for total internal reflection will be 48.75°.

All of our ZnO nanoporous structure-coated surfaces appeared as dark gray in the air. However, surfaces showed mirror-like silvery surfaces when just submerged into water due to the air voids (or air plastron) captured between surface asperities, whose air–water interfaces caused the total internal reflection of the light[5,9,84,85] (Figure 5.16).

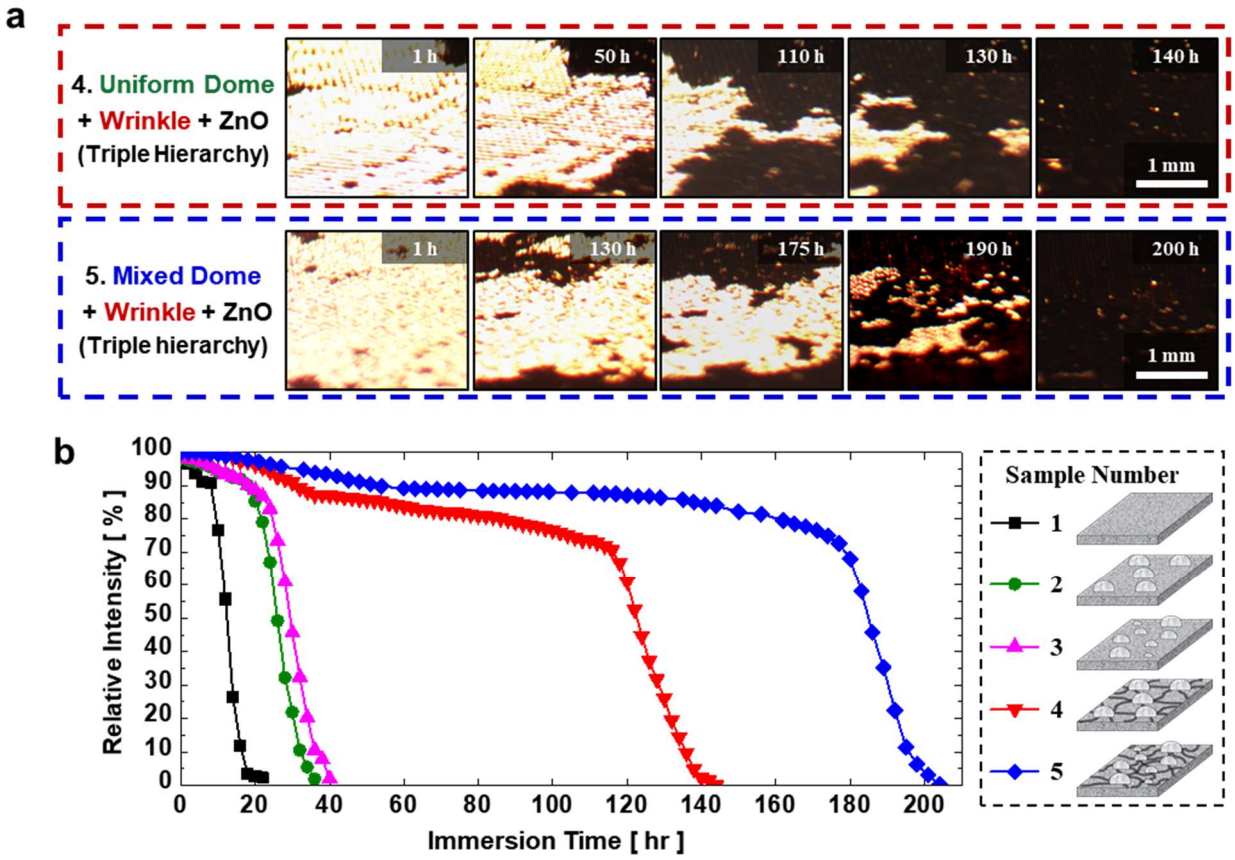

Figure 5.17. Resistance to water impingement (or underwater superhydrophobicity) of surfaces with increasing surface complexities. (a) Superhydrophobic performance under the extreme condition (or the resistance to water impingement). Images show air plastrons on Samples 4 and 5 at an immersion depth of approximately 21 cm for different immersion times. The air plastron appeared as bright regions due to total reflection at the interface between water and air pockets. These bright pixels decayed gradually as the water–air interface faded away or the air plastron diffused into the water. The scale bars in the last columns are applicable to all images. (b) Relative intensity plot of our five different surfaces with increasing surface complexity. At a water immersion depth of 21 cm, a hydrostatic pressure is exerted on the superhydrophobic surface that is approximately four times greater than the gravitational pressure exerted by a 7 μL droplet on the same surface during a conventional water sessile contact angle measurement.

As shown in Figure 5.17a, surfaces with the air plastron appeared as bright regions at the beginning of immersion, due to reflection at the interface between water and air pockets. Those bright regions decayed gradually into dark pixels as the water–air interface was destroyed by wetting.

In Figure 5.17b, the relative reflected intensity[5,9,84,85] was plotted against the immersion time for all of our surfaces with various degrees of surface complexity. Although all the samples started with the close to 100% relative intensities, each surface was observed to lose its water-repellent behavior at different rates.

Similar to the trend observed in static contact angle, the sample with the greatest surface complexity took the longest time until the underwater superhydrophobicity broke down. The triple-hierarchical surface with a mixed-size dome array (Sample 5) resulted in by far the longest time to loss of superhydrophobicity, which was approximately 204 hours, while the ZnO nanostructure on an otherwise flat surface (Sample 1) took only approximately 22 hours to wet completely. These clear results are consistent with, e.g., Xue's and Lee's previous studies[5,86], indicating that our triple hierarchical superhydrophobic surface (TriSS) with the array of mixed domes (Sample 5) is highly effective at resisting to water impingement even when fully immersed[62].

5.9 Conclusion

We have presented a novel, bio-inspired triple-hierarchical superhydrophobic surface (TriSS) that has unprecedented artificial multi-level surface complexity. Our facile manufacturing strategy provides a basis for controlling the formation of topographically-varied micro-grooves for extraordinary water-repellent characteristics. We believe that the TriSS technology will provide a promising strategy in many relevant industries. Multiphase heat transfer, although not yet explored in the context of TriSS, is one area where water shedding is of critical importance, and would be a fruitful area for further investigation. Successful fabrication of superhydrophobic surfaces for heat transfer applications is likely to require a bulk metallic surface for high thermal conductance, rather than an elastomeric one as used here. In manufacturing, we therefore may envision our microfabricated surface with an array of micro-domes and periodic microgrooves being used as the master mold for electroplating a hard metallic die that would then be stamped into, e.g., a bulk soft aluminum alloy fin stock[62].

Chapter 6. Summary and Future Work

6.1 Summary

In-depth investigations into novel micro- and nano-manufacturing processes for forming bio-inspired geometrically complex structures were studied in this research. By minimizing the water–surface contact fraction through a remarkable resemblance to *Nelumbo nucifera* (lotus leaf) structures, our surfaces achieved various interesting superior water-repellent performances, such as higher water sessile contact angle, lower water hysteresis, efficient dropwise condensation, and robust water impingement resistance in the adverse environments (e.g. immersed in water).

In Chapter 3, two different shapes of structure (micro-pillar and micro-dome) with various sizes and spacings were tested. This Chapter revealed that the array of micro-domes achieved higher static contact angle and lower contact angle hysteresis than both the micro-pillar array and the flat ZnO nanoporous surface with no microstructures. We also observed that both static contact angle and hysteresis are strongly dependent on the feature-sizes and spacings. Best performance was obtained with the smallest (20 μm) and most closely spaced (10 μm) domes tested, suggesting that it would be useful to investigate whether further reducing dome size or spacing could increase the performance even more.[41]

In Chapter 4, we provided an experimental framework for evaluating the dropwise condensation performance of hierarchically structured surfaces in an environment similar to the tropical regions (hot and humid air). Of the surfaces tested, we found the most favorable dropwise condensation performance occurred on an array of 30 μm-diameter domes separated by 30 μm, with the fluoro-silanized ZnO film applied conformally. Surfaces with square-tipped pillars of comparable size and spacing and the surface of only a fluorosilanized ZnO nanoporous coating exhibited much less favorable results, with surfaces flooding occurring. In addition, we compared the condensation performance of various ZnO growth conditions, established its possibility to be scalable, and devised and optimized a new spray-based fluoro-silanization method to reduce reagent consumption relative to immersion-coating when treating large heat exchanger surfaces.[57]

In Chapter 5, we introduced a novel micro- and nano-manufacturing process to mimic even more closely the complex geometries of the lotus leaf epidermis. Our triple-hierarchical superhydrophobic surface (TriSS) has three distinctive levels of structure and its precisely tuned surface morphology bears the highest resemblance to the actual lotus leaf. The surface is composed of an array of micro-domes of various sizes and heights, produced via a standard single-layer photolithography step followed by thermal reflow. Wrinkles are then induced by surface oxidation of the cast elastomeric material, followed by sequential release of biaxial stress. Finally, conformal growth of a zinc oxide nanoporous coating takes place. The TriSS surface achieved outstanding water repellency and hysteresis due to minimized liquid–solid contact fractions at the curved tips of the micro-dome array, which were topographically distorted by micro-grooves. Furthermore, our triple-hierarchical surface was highly effective in resisting water impingement by capturing and retaining a stable air layer even when fully immersed.[62]

6.2 Future work

Possible future research could usefully address the fact that the conventional Cassie–Baxter model was not found to be able to describe quantitatively the water sessile contact angle trends for various feature spacings, nor the trends for the curved features (micro-domes) that were observed in our project. We believe that this discrepancy may be explained by the fact that the liquid–air interfaces located between the solid–liquid contact regions of a composite interface are assumed to be perfectly straight in the Cassie model, while the local contact angle at the contact region remains the same (approximately 157° in our case). In reality, it is possible that the patterns with the larger inter-feature spacings permitted more meniscus curvature under the action of gravity on the droplet, which may have increased the solid–liquid contact fraction and thereby reduced the contact angle compared to the Cassie prediction. A more sophisticated model incorporating gravity-related terms and contact angle hysteresis may be needed to describe accurately the overall performance of the surfaces demonstrated in this dissertation.

In addition, it would be interesting to design further experiments to better quantify the condensation heat transfer coefficients of our various surface designs. The method we developed to determine condensation performance was based on extraction of the condensate area fraction using customized droplet image boundary analysis routines. However, these results may not be fully representative since the surfaces tested were predominantly elastomeric, with a thin aluminum and ZnO coating, and will have therefore had higher thermal resistances than would be expected from, e.g., a fully metallic heat-exchanger fin. The *rate* of condensation is expected to play an important role in

determining the degree to which dropwise condensation can be sustained. Further investigation of the relation between condensation heat transfer coefficients and droplet growth and coalescence dynamics would be an important next step.

Additionally, we found that stable and unprecedented water-repellency could be obtained from our three-tier hierarchical surface (TriSS). The micro-groove generation process, based on the release of biaxial stress from an oxidized sample surface, was found to be strongly templated by the presence of micro-patterns on the target surface. Employing micro-domes with a range of sizes increased even more the prominence of the induced micro-wrinkles, and as a result, the underlying microstructured features were seen to become somewhat distorted, generating the most complex artificial triple hierarchical surface. It would be interesting to investigate more deeply the relationship between the wrinkle induction effect and the various sizes and shapes of the micro-patterns that can be used to direct wrinkling. Moreover, since the TriSS surface showed a remarkable ability to maintain the air plastron over an extended time period, potenital performance improvements in the underwater drag reduction could also be usefully explored.

Lastly, superhydrophobic surfaces for condensation heat-transfer applications generally require a metallic material rather than an elastomeric one to enable low thermal resistance to be achieved. For practical manufacturing, we therefore may envision our surface with array of micro-domes with periodic microgrooves being used as the master mold for electroplating a hard metallic die that would then be stamped into bulk soft aluminum alloy fin stock.

Chapter 7. Bibliography

[1] Wang, S., Liu, K., Yao, X. & Jiang, L. Bioinspired Surfaces with Superwettability: New Insight on Theory, Design, and Applications. *Chem. Rev.* **115**, 8230–8293 (2015).

[2] Ensikat, H. J., Ditsche-Kuru, P., Neinhuis, C. & Barthlott, W. Superhydrophobicity in perfection: the outstanding properties of the lotus leaf. *Beilstein J. Nanotechnol.* **2**, 152–161 (2011).

[3] Cassie, A. B. D. & Baxter, S. Wettability of porous surfaces. *Trans. Faraday Soc.* **40**, 546–551 (1944).

[4] Bhushan, B., Koch, K. & Jung, Y. C. Biomimetic hierarchical structure for self-cleaning. *Appl. Phys. Lett.* **93**, 093101 (2008).

[5] Lee, J. & Yong, K. Combining the lotus leaf effect with artificial photosynthesis: regeneration of underwater superhydrophobicity of hierarchical ZnO/Si surfaces by solar water splitting. *NPG Asia Mater.* **7**, e201–e201 (2015).

[6] Kwon, Y., Patankar, N., Choi, J. & Lee, J. Design of Surface Hierarchy for Extreme Hydrophobicity. *Langmuir* **25**, 6129–6136 (2009).

[7] Koch, K., Bhushan, B., Chae Jung, Y. & Barthlott, W. Fabrication of artificial Lotus leaves and significance of hierarchical structure for superhydrophobicity and low adhesion. *Soft Matter* **5**, 1386–1393 (2009).

[8] Bhushan, B., Jung, Y. C., Niemietz, A. & Koch, K. Lotus-Like Biomimetic Hierarchical Structures Developed by the Self-Assembly of Tubular Plant Waxes. *Langmuir* **25**, 1659–1666 (2009).

[9] Poetes, R., Holtzmann, K., Franze, K. & Steiner, U. Metastable Underwater Superhydrophobicity. *Phys. Rev. Lett.* **105**, 166104 (2010).

[10] Jung, Y. C. & Bhushan, B. Wetting behaviour during evaporation and condensation of water microdroplets on superhydrophobic patterned surfaces. *J. Microsc.* **229**, 127–140 (2008).

[11] Adamsom, A. & Gast, A. *Physical Chemistry of surfaces*. (Wiley, New York, 1997).

[12] Young, T. III. An essay on the cohesion of fluids. *Philos. Trans. R. Soc. Lond.* **95**, 65–87 (1805).

[13] Wenzel, R. N. Surface Roughness and Contact Angle. *J. Phys. Colloid Chem.* **53**, 1466–1467 (1949).

[14] Good, R. J. Contact angle, wetting, and adhesion: a critical review. *J. Adhes. Sci. Technol.* **6**, 1269–1302 (1992).

[15] Feng, L. *et al.* Super-Hydrophobic Surfaces: From Natural to Artificial. *Adv. Mater.* **14**, 1857–1860 (2002).

[16] Davis, L. W. & Gertler, P. J. Contribution of air conditioning adoption to future energy use under global warming. *Proc. Natl. Acad. Sci. U. S. A.* **112**, 5962–5967 (2015).

[17] Liu, L. & Jacobi, A. M. The effects of hydrophilicity on water drainage and condensate retention on air-conditioning evaporators. in *International Refrigeration and Air Conditioning Conference* (2006).
[18] Paxson, A. T. Advanced materials for enhanced condensation heat transfer. (Massachusetts Institute of Technology, 2014).
[19] Yin, L., Zhu, L., Wang, Q., Ding, J. & Chen, Q. Superhydrophobicity of Natural and Artificial Surfaces under Controlled Condensation Conditions. *ACS Appl. Mater. Interfaces* **3**, 1254–1260 (2011).
[20] Enright, R., Miljkovic, N., Al-Obeidi, A., Thompson, C. V. & Wang, E. N. Condensation on Superhydrophobic Surfaces: The Role of Local Energy Barriers and Structure Length Scale. *Langmuir* **28**, 14424–14432 (2012).
[21] Ma, F. M. *et al.* Geometrical effect, optimal design and controlled fabrication of bio-inspired micro/nanotextures for superhydrophobic surfaces. *Mater. Res. Express* **4**, 092001 (2017).
[22] Koch, K., Bhushan, B. & Barthlott, W. Diversity of structure, morphology and wetting of plant surfaces. *Soft Matter* **4**, 1943–1963 (2008).
[23] Nosonovsky, M. Multiscale Roughness and Stability of Superhydrophobic Biomimetic Interfaces. *Langmuir* **23**, 3157–3161 (2007).
[24] Feng, L. *et al.* Creation of a Superhydrophobic Surface from an Amphiphilic Polymer. *Angew. Chem. Int. Ed.* **42**, 800–802 (2003).
[25] Bhushan, B. Biomimetics: lessons from nature–an overview. *Philos. Trans. R. Soc. Math. Phys. Eng. Sci.* **367**, 1445–1486 (2009).
[26] Bhushan, B. & Jung, Y. C. Natural and biomimetic artificial surfaces for superhydrophobicity, self-cleaning, low adhesion, and drag reduction. *Prog. Mater. Sci.* **56**, 1–108 (2011).
[27] Extrand, C. W. Designing for Optimum Liquid Repellency. *Langmuir* **22**, 1711–1714 (2006).
[28] Latthe, S. S., Terashima, C., Nakata, K. & Fujishima, A. Superhydrophobic Surfaces Developed by Mimicking Hierarchical Surface Morphology of Lotus Leaf. *Molecules* **19**, 4256–4283 (2014).
[29] Park, K.-C. *et al.* Condensation on slippery asymmetric bumps. *Nature* **531**, 78–82 (2016).
[30] Lee, W.-K., Jung, W.-B., Nagel, S. R. & Odom, T. W. Stretchable Superhydrophobicity from Monolithic, Three-Dimensional Hierarchical Wrinkles. *Nano Lett.* **16**, 3774–3779 (2016).
[31] Brockway, L. & Taylor, H. A nanoporous, ultrahydrophobic aluminum-coating process with exceptional dropwise condensation and shedding properties. *Mater. Res. Express* **4**, 045003 (2017).
[32] Extrand, C. W. Contact Angles and Hysteresis on Surfaces with Chemically Heterogeneous Islands. *Langmuir* **19**, 3793–3796 (2003).

[33] Erbil, H. Y. & Cansoy, C. E. Range of Applicability of the Wenzel and Cassie−Baxter Equations for Superhydrophobic Surfaces. *Langmuir* **25**, 14135–14145 (2009).
[34] Zhang, X. *et al.* Effect of pattern topology on the self-cleaning properties of textured surfaces. *J. Chem. Phys.* **127**, 014703 (2007).
[35] Teisala, H. *et al.* Nanostructures Increase Water Droplet Adhesion on Hierarchically Rough Superhydrophobic Surfaces. *Langmuir* **28**, 3138–3145 (2012).
[36] Varanasi, K. K., Deng, T., Hsu, M. & Bhate, N. Hierarchical Superhydrophobic Surfaces Resist Water Droplet Impact. in *Technical Proceedings of the 2009 NSTI Nanotechnology Conference and Expo* (2009).
[37] Zhao, H., Park, K.-C. & Law, K.-Y. Effect of Surface Texturing on Superoleophobicity, Contact Angle Hysteresis, and "Robustness". *Langmuir* **28**, 14925–14934 (2012).
[38] Wier, K. A. & McCarthy, T. J. Condensation on Ultrahydrophobic Surfaces and Its Effect on Droplet Mobility: Ultrahydrophobic Surfaces Are Not Always Water Repellant. *Langmuir* **22**, 2433–2436 (2006).
[39] Edalatpour, M., Liu, L., Jacobi, A. M., Eid, K. F. & Sommers, A. D. Managing water on heat transfer surfaces: A critical review of techniques to modify surface wettability for applications with condensation or evaporation. *Appl. Energy* **222**, 967–992 (2018).
[40] Hisler, V. *et al.* Model Experimental Study of Scale Invariant Wetting Behaviors in Cassie–Baxter and Wenzel Regimes. *Langmuir* **30**, 9378–9383 (2014).
[41] S. Chung, K. Kadala, and H. Taylor. Enhancement of Water Repellence by Hierarchical Surface Structures Integrating Micro-dome and Micro-pillar Arrays with Nanoporous Coatings. *SUBMITTED* (2019).
[42] Shao, G., Wu, J., Cai, Z. & Wang, W. Fabrication of elastomeric high-aspect-ratio microstructures using polydimethylsiloxane (PDMS) double casting technique. *Sens. Actuators Phys.* **178**, 230–236 (2012).
[43] ImageJ. https://imagej.nih.gov/ij/.
[44] Stalder, A. F. *et al.* Low-bond axisymmetric drop shape analysis for surface tension and contact angle measurements of sessile drops. *Colloids Surf. Physicochem. Eng. Asp.* **364**, 72–81 (2010).
[45] Stalder, A. F., Kulik, G., Sage, D., Barbieri, L. & Hoffmann, P. A snake-based approach to accurate determination of both contact points and contact angles. *Colloids Surf. Physicochem. Eng. Asp.* **286**, 92–103 (2006).
[46] Zhu, L., Feng, Y., Ye, X. & Zhou, Z. Tuning wettability and getting superhydrophobic surface by controlling surface roughness with well-designed microstructures. *Sens. Actuators Phys.* **130–131**, 595–600 (2006).
[47] Brockway, L. & Taylor, H. A statistical model for the wettability of surfaces with heterogeneous pore geometries. *Mater. Res. Express* **3**, 105039 (2016).
[48] Yeh, K.-Y., Chen, L.-J. & Chang, J.-Y. Contact Angle Hysteresis on Regular Pillar-like Hydrophobic Surfaces. *Langmuir* **24**, 245–251 (2008).

[49] Lv, C., Yang, C., Hao, P., He, F. & Zheng, Q. Sliding of Water Droplets on Microstructured Hydrophobic Surfaces. *Langmuir* **26**, 8704–8708 (2010).
[50] Air conditioning use emerges as one of the key drivers of global electricity-dema. https://www.iea.org/newsroom/news/2018/may/air-conditioning-use-emerges-as-one-of-the-key-drivers-of-global-electricity-dema.html.
[51] Wilke, K. L., Preston, D. J., Lu, Z. & Wang, E. N. Toward Condensation-Resistant Omniphobic Surfaces. *ACS Nano* **12**, 11013–11021 (2018).
[52] Miljkovic, N. & Wang, E. N. Condensation heat transfer on superhydrophobic surfaces. *Nenad Miljkovic* (2013).
[53] Miljkovic, N. *et al.* Jumping-Droplet-Enhanced Condensation on Scalable Superhydrophobic Nanostructured Surfaces. *Nano Lett.* **13**, 179–187 (2013).
[54] Bhushan, B. & Chae, Y. J. Wetting study of patterned surfaces for superhydrophobicity. *Ultramicroscopy* **107**, 1033–1041 (2007).
[55] Zhang, J., Sheng, X. & Jiang, L. The Dewetting Properties of Lotus Leaves. *Langmuir* **25**, 1371–1376 (2009).
[56] Lv, C. *et al.* Condensation and jumping relay of droplets on lotus leaf. *Appl. Phys. Lett.* **103**, 021601 (2013).
[57] S. Chung, K. Kadala, and H. Taylor. Stable dropwise condensation observed on a hierarchically structured superhydrophobic surface integrating micro-domes. *SUBMITTED* (2019).
[58] ImageJ User Guide - IJ 1.46r. https://imagej.nih.gov/ij/docs/guide/index.html.
[59] Mohammad Karim, A. & Kavehpour, H. P. Dynamics of spreading on ultra-hydrophobic surfaces. *J. Coat. Technol. Res.* **12**, 959–964 (2015).
[60] Global image threshold using Otsu's method - MATLAB graythresh. https://www.mathworks.com/help/images/ref/graythresh.html.
[61] The Watershed Transform: Strategies for Image Segmentation. https://www.mathworks.com/company/newsletters/articles/the-watershed-transform-strategies-for-image-segmentation.html.
[62] S. Chung, C. Riley, and H. Taylor. A Novel Bio-inspired Triple-hierarchical Superhydrophobic Surface (TriSS). *SUBMITTED* (2019).
[63] Kreder, M. J., Alvarenga, J., Kim, P. & Aizenberg, J. Design of anti-icing surfaces: smooth, textured or slippery? *Nat. Rev. Mater.* **1**, 1–15 (2016).
[64] Bhushan, B. Biomimetics: lessons from nature–an overview. *Philos. Trans. R. Soc. Lond. Math. Phys. Eng. Sci.* **367**, 1445–1486 (2009).
[65] Laplace pressure. *Wikipedia* https://en.wikipedia.org/w/index.php?title=Laplace_pressure&oldid=915733997 (2019).
[66] Lin, P.-C. & Yang, S. Spontaneous formation of one-dimensional ripples in transit to highly ordered two-dimensional herringbone structures through sequential and unequal biaxial mechanical stretching. *Appl. Phys. Lett.* **90**, 241903 (2007).
[67] Yang, S., Khare, K. & Lin, P.-C. Harnessing Surface Wrinkle Patterns in Soft Matter. *Adv. Funct. Mater.* **20**, 2550–2564 (2010).

[68] Khare, K., Zhou, J. & Yang, S. Tunable Open-Channel Microfluidics on Soft Poly(dimethylsiloxane) (PDMS) Substrates with Sinusoidal Grooves. *Langmuir* **25**, 12794–12799 (2009).
[69] Bowden, N., Huck, W. T. S., Paul, K. E. & Whitesides, G. M. The controlled formation of ordered, sinusoidal structures by plasma oxidation of an elastomeric polymer. *Appl. Phys. Lett.* **75**, 2557–2559 (1999).
[70] Huang, Z. Y., Hong, W. & Suo, Z. Nonlinear analyses of wrinkles in a film bonded to a compliant substrate. *J. Mech. Phys. Solids* **53**, 2101–2118 (2005).
[71] Chen, X. & Hutchinson, J. W. A family of herringbone patterns in thin films. *Scr. Mater.* **50**, 797–801 (2004).
[72] Maitra, T. *et al.* Hierarchically nanotextured surfaces maintaining superhydrophobicity under severely adverse conditions. *Nanoscale* **6**, 8710–8719 (2014).
[73] Antonini, C., Carmona, F. J., Pierce, E., Marengo, M. & Amirfazli, A. General Methodology for Evaluating the Adhesion Force of Drops and Bubbles on Solid Surfaces. *Langmuir* **25**, 6143–6154 (2009).
[74] Quéré, D. Non-sticking drops. *Rep. Prog. Phys.* **68**, 2495–2532 (2005).
[75] Antonini, C., Villa, F., Bernagozzi, I., Amirfazli, A. & Marengo, M. Drop Rebound after Impact: The Role of the Receding Contact Angle. *Langmuir* **29**, 16045–16050 (2013).
[76] Reyssat, M., Pépin, A., Marty, F., Chen, Y. & Quéré, D. Bouncing transitions on microtextured materials. *EPL Europhys. Lett.* **74**, 306 (2006).
[77] Bartolo, D. *et al.* Bouncing or sticky droplets: Impalement transitions on superhydrophobic micropatterned surfaces. *EPL Europhys. Lett.* **74**, 299 (2006).
[78] Yahui Xue, Pengyu Lv, Hao Lin, Huiling Duan. Underwater Superhydrophobicity: Stability, Design and Regulation, and Applications | Applied Mechanics Reviews | ASME Digital Collection. *Appl. Mech. Rev.* **68**, (2016).
[79] Jung, Y. C. & Bhushan, B. Dynamic Effects Induced Transition of Droplets on Biomimetic Superhydrophobic Surfaces. *Langmuir* **25**, 9208–9218 (2009).
[80] Cheng, Y.-T. & Rodak, D. E. Is the lotus leaf superhydrophobic? *Appl. Phys. Lett.* **86**, 144101 (2005).
[81] Rathgen, H., Sugiyama, K., Ohl, C.-D., Lohse, D. & Mugele, F. Nanometer-Resolved Collective Micromeniscus Oscillations through Optical Diffraction. *Phys. Rev. Lett.* **99**, 214501 (2007).
[82] Reyssat, M., Yeomans, J. M. & Quéré, D. Impalement of fakir drops. *EPL Europhys. Lett.* **81**, 26006 (2007).
[83] Govardhan, R. N., Srinivas, G. S., Asthana, A. & Bobji, M. S. Time dependence of effective slip on textured hydrophobic surfaces. *Phys. Fluids* **21**, 052001 (2009).
[84] Lee, J. & Yong, K. Surface chemistry controlled superhydrophobic stability of W 18 O 49 nanowire arrays submerged underwater. *J. Mater. Chem.* **22**, 20250–20256 (2012).

[85] Bobji, M. S., Kumar, S. V., Asthana, A. & Govardhan, R. N. Underwater Sustainability of the “Cassie” State of Wetting. *Langmuir* **25**, 12120–12126 (2009).
[86] Xue, Y., Chu, S., Lv, P. & Duan, H. Importance of Hierarchical Structures in Wetting Stability on Submersed Superhydrophobic Surfaces. *Langmuir* **28**, 9440–9450 (2012).